UNIVERSIDAD NACIONAL AUTÓNOMA DE MÉXICO
POSGRADO EN CIENCIA FÍSICAS
INSTITUTO DE CIENCIAS FÍSICAS

EFFECT OF NONCENTROSYMMETRIC GEOMETRY ON SECOND ORDER OPTICAL PROPERTIES OF NANOSTRUCTURES

TESIS QUE PARA OPTAR POR EL GRADO DE:
DOCTOR EN CIENCIAS (FÍSICA)

PRESENTA:

RAKSHA SINGLA

TUTOR PRINCIPAL:

DR. WOLF LUIS MOCHÁN BACKAL
INSTITUTO DE CIENCIAS FÍSICAS, UNAM

MIEMBROS DEL COMITÉ TUTORIAL:

DR. JORGE ALEJANDRO REYES ESQUEDA
INSTITUTO DE FÍSICA, UNAM

DRA. VIVECHANA AGARWAL
CENTRO DE INVESTIGACIÓN EN INGENIERÍAS
Y CIENCIAS APLICADAS, UAEM

CUERNVACA, MORELOS, AGOSTO DE 2020

Dedicated to my father
Mr. Pradip Kr. Ruia

Abstract

We explore three-wave mixing phenomena such as the second harmonic (SHG), sum frequency (SFG), and difference frequency (DFG) generation from nanostructures and nanowires with non-centrosymmetric geometry made up of a centrosymmetric material. We perform both a numerical analysis and an approximate analytical calculation of the response tensors. First, we obtain and evaluate approximate analytical formulas for the SH, DF and SF hyperpolarizability tensors of an isolated infinite cylinder with a cross section that is slightly deformed away from a circle with three protuberances separated by an angle of 120° in the plane and with its nominal radius much smaller than the wavelength of light. We perform calculations in $2D$ owing to the translational symmetry along the axis of the cylinder. We utilize a perturbative method, with the deformation as the perturbation parameter, to find approximate expressions for the self-consistent linear and nonlinear fields. We evaluate the nonlinear dipolar and quadrupolar SH, DF, and SF hyperpolarizability, and analyze their spectra for metallic and dielectric cylinders. We discuss the nature of the SH fields radiated at various input frequencies; we find that dominant contribution may arise from either the dipolar or the quadrupolar nonlinear response and they may also compete with each other to produce non-symmetric radiation patterns. In addition to SH radiated fields, we compute the fields radiated at the DF and SF frequencies and determine the efficiency of the DFG/SFG from the nanowire.

Next, we consider a nanostructure formed of an array of the non-centrosymmetric cylinders and explore its SH response. To this end, we apply an efficient homogenization scheme to obtain the macroscopic quadratic SH response. This scheme was developed by our group, implemented in a programming package called *Photonic*, to calculate the macroscopic linear and nonlinear response of metamaterials. The program is based on an implementation of the *dipolium* model to calculate the second order polarization and susceptibility. In this work, an exhaustive testing of the previously developed modules for the computation of the nonlinear response is performed and its limitations identified. The problems discovered are corrected and validated against the analytical results. We make the area of each unit cell relatively large, in order to separate each element of the array, so that the interaction between them is negligible. This permits us to calibrate and assess the results of our numerical analysis by comparing it to the analytical expressions. We obtain good agreement between both the results for small deformations; thus verifying the results of our numerical approach. Furthermore, we perform computations for larger deformations, a regime where the perturbative analytical formulas fail, to investigate the evolution of the response as the deformation is increased. This yields the limit up to which our analytical expressions are valid.

Resumen

En esta tesis, investigamos fenómenos que involucran el mezclado de tres ondas como generación de segundo armónico (GSA), de suma de frecuencias (GSF) y de diferencia de frecuencias (GDF) por nanoestructuras y metamateriales con geometría no centrosimétricas formadas por materiales centrosimétricos, realizando nuestros estudios numéricamente y analíticamente. En la primera parte del trabajo calculamos analíticamente la respuesta no lineal, tanto de GSA como de GDF y GSF, de una partícula bidimensional y aislada en forma de un cilindro infinito con una sección transversal ligeramente deformada con respeto a un círculo. Obtuvimos expresiones analíticas para las hiperpolarizabilidades del cilindro no centrosimétrico en términos de respuestas lineales del sistema y algunos parámetros que caracterizan las distintas contribuciones del sistema a la polarización no lineal. Suponiendo que el sistema tiene simetría translacional a lo largo del eje del cilindro, hicimos nuestros cálculos en $2D$. Además, escogimos al radio del círculo mucho mas pequeño que la longitud de onda para hacer nuestros cálculos dentro del régimen donde la aproximación de longitud de onda larga es válida. Utilizamos un método perturbativo eligiendo la deformación como un parámetro perturbativo y obtuvimos expresiones aproximadas hasta el orden lineal en la deformación para los campos lineales y no lineales inducidos en el sistema. Usando los campos inducidos y los resultados del modelo de *dipolium*, evaluamos las contribuciones del bulto y superficie a la polarización no lineal inducida en el cilindro. Obtuvimos expresiones para las hiperpolarizabilidades de tipo SA, SF y DF incluyendo las contribuciones dipolar y cuadrupolar, y analizamos sus características espectrales para cilindros metálicos y dieléctricos. También calculamos los campos SA en la zona de radiación y discutimos las características de los patrones de radiación para SA con distintas frecuencias para la luz incidente. Encontramos que dependiendo de la frecuencia de la luz, las contribuciones dipolar o cuadrupolar compiten entre sí y en algunos casos domina una sobre la otra. El patrón de radiación muestra formas no simétricas para los casos donde ambas contribuciones son comparables. Además, evaluamos los campos DF y SF radiados para investigar la eficiencia del proceso del GDF y GSF.

La segunda parte del trabajo involucra el estudio numérico de la GSA desde un metamaterial binario formado por una red de inclusiones, cada una de las cuales tiene la misma geometría que la de nuestra partícula aislada. El código que empleamos es parte del paquete *Photonic* desarrollado por nuestro grupo, el cual nos permite calcular eficientemente campos locales de metamateriales binarios. El paquete tiene incorporado el modelo de *dipolium*, lo cual nos permite calcular la polarización y la susceptibilidad no lineal a partir de los campos microscópicos locales. En este trabajo, realizamos pruebas exhaustivas de los módulos que calculan la respuesta no lineal e identificamos imprecisiones, las cuales fueron corregidas y verificadas contrastándo los resultados numéricos con los resultados analíticos. Elegimos las celdas unitarias con tamaños relativamente grandes, lo cual permite despreciar las interacciones entre las pequeñas inclusiones. Eso nos permite comparar los resultados numéricos con los analíticos y validar nuestros códigos. Encontramos un buen acuerdo entre los resultados de ambos cálculos para deformaciones pequeñas. Después de validar los resultados de los códigos, realizamos cálculos para deformaciones grandes, en un régimen en el cual las expresiones analíticas no son válidas, para estudiar el efecto de la deformación y la evolución de la respuesta conforme la deformación crece. Encontramos así los limites de validez de nuestra teoría perturbativa y analítica.

Acknowledgements

I have finally come to the end of the enriching experience of pursuing a doctorate. Never had I imagined, I would be writing my thesis amid a crisis as big as a pandemic. Words are certainly not enough to express my gratitude to everyone who were part of this wonderful journey without whom I would not have been able to see its end.

I begin by whole-heartedly thanking my husband, Tanu, for standing beside me through thick and thin and always believing in me. Without his constant motivation, I would have not been able to make it through. I thank my entire family in India for sending me their best wishes throughout my doctorate. I cannot thank my parents enough for always motivating me to pursue my dreams of a career in science; which sadly is still not common in my region. Without their inspiration and love, I would not be the person I am today. Special thanks to my sister, Pooja, for always being there. I immensely appreciate my parents-in-law for their support during my doctoral research.

I would like to express my deepest gratitude to my tutor and a very good friend Dr. Luis Mochán whose insight and knowledge into the subject and many related and unrelated fields made my doctorate an inspirational journey. His enthusiasm and encouragement steered me through the research presented in this thesis. The ways of his life showed me how to not only be a brilliant scientist but a better person.

I appreciate the valuable suggestions from the members of my tutorial committee, Dr. Vivechana Agarwal and Dr. Jorge Alejandro Reyes Esqueda, during the semesterly examinations which helped in enhancing the contents of this research. I acknowledge the insightful discussions on the research work for my doctoral thesis with our collaborators, Dr. Bernardo Mendoza, Dr. Guillermo P. Ortiz and Dr. Lucila Juárez. I also had the pleasure of working with them on other related projects. I especially thank Lucila for becoming one of my closest friends and always being there for me.

I would also like to acknowledge the institution *Consejo Nacional de Ciencia y Tecnología* (CONACYT) for their financial support through the national scholarship programme; scholarship number 600337. I also acknowledge the economic support from DGAPA-UNAM PAPIIT projects Nos. IN113016 and IN111119 and the university grant PAEP for supporting my participation in different national and international conferences; and the economic support from DGAPA-UNAM PAPIIT to finish my studies after the end of my scholarship. I express my sincere gratitude to all the people of the university, Universidad Nacional Autónoma de México with whom I have interacted in the course of my studies. Special regards to the entire community of my institute, Instituto de Ciencias Físicas, where I had the opportunity to interact and come to know wonderful researchers. I thank all the researchers with whom I took classes to prepare for admission exams to the program: Dr. José Récamier, Dr. Max Aldana, Dr. Frédéric Masset, and Dr. Hernán Larralde.

From the bottom of my heart I would like to say a big thanks to all of my friends here in Mexico who made me a part of their life in this foreign country and making being so far from home simpler. I grew as a person learning about new cultures and a new language from them. I specially thank Lucila, Karla, Adriana, David and Sebastien. I hope I am not forgetting anyone; thanks to Arturo, Tammy, Bertha, Diego, Carlos, Manan, Harinder, Luisana, Eric, Martín, Cristina, Mota, Mayra, Rocío, Merlyn.

Last but not the least, I acknowledge the jury members who evaluated this work, for their invaluable suggestions and corrections to the thesis.

Contents

Introduction

Nonlinear nanophotonics, a sub branch of nanoscience, is an emerging field of research offering multifaceted opportunities for the manipulation and control of light at the nanometer scale. It primarily focuses on the sub-wavelength behavior of light and its interaction with nanostructured materials in order to engineer highly efficient and ultrafast novel nanophotonic devices. Rapid advances in this discipline is the result of a multitude of applications it promises in the fields of science, engineering, and medicine; nonlinear nanoantennas, nanophotonic circuits for nanoscale electronics, light sources, biosensing, targeted drug delivery systems, medical implants, to name a few. For application purposes, most of the important nonlinear optical effects take place at the second or third order; namely three- and four-wave mixing effects (TWM and FWM) such as second- and third-harmonic generation (SHG and THG), optical Kerr effect, self-phase modulation (SPM), and stimulated Raman scattering (SRS). Nanophotonic devices fabricated from metallic, metal-dielectric, and all dielectric materials have been reported in the form of diverse types of structures such as metamaterials, metasurfaces, nanoparticles and their arrays [1–7]. This work is dedicated to the investigation of second order nonlinear optical response, such as second harmonic generation (SHG), and sum and difference frequency generation (SFG/DFG) from an isolated nanowire and also SHG from a nanostructure formed by a periodic array of such nanowires.

Long before we started to develop artificial photonic nanostructures, nature had perfected this art as many organisms have been found to possess and exploit nanophotonic structures to exhibit extraordinary optical effects [8]. For example, the impressive blue colored iridescent pattern of the *Morpho* butterflies is the result of interference effects within the photonic microstructures formed by its multiple layers of cuticle and air [Fig. 1]. The evolution of these colored patterns has been thought to be driven by diverse reasons such as mate attraction, camouflage, mimicry, etc. Another example is the structure of the arm ossicles from light-sensitive species of the brittle-star, *Ophiocoma wendtii* [8]. They possess arrays of inorganic microstructures composed of anisotropic calcite microlenses with a design to detect incoming light from a particular direction [Fig. 2]. This sensitivity to light

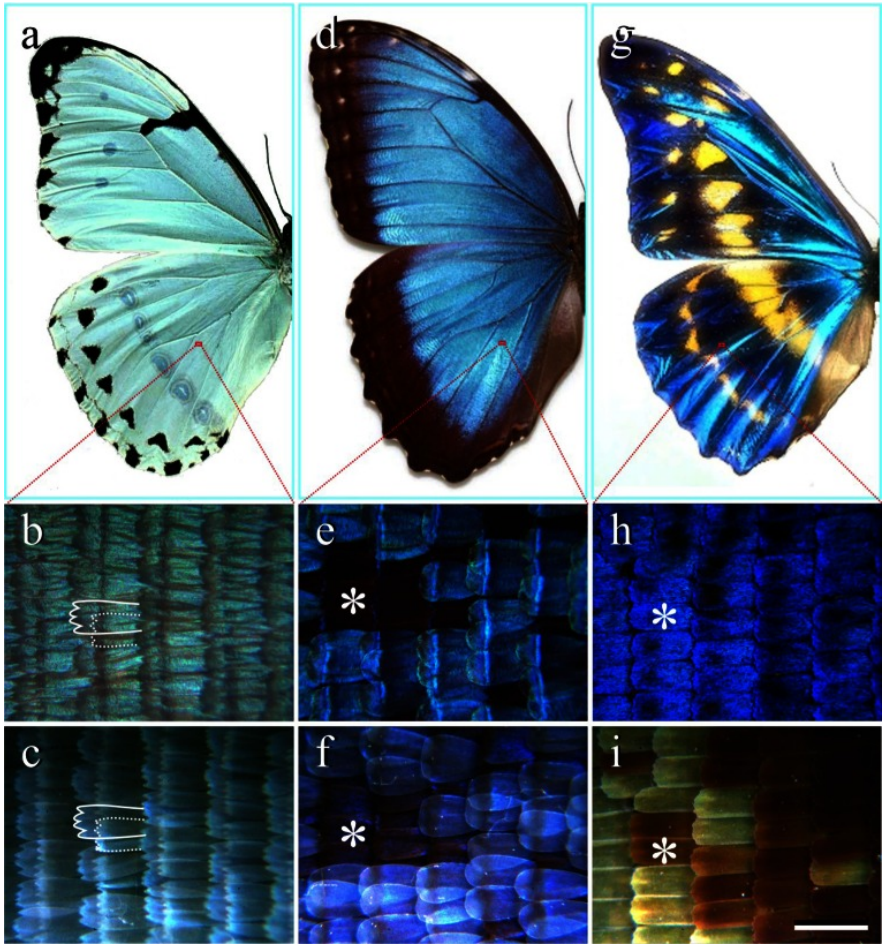

Figure 1: Photographs of the left wings of three species of *Morpho* Butterflies (a, d, g) along with the bright-field (b, e, h) and dark-field (c, f, i) micrographs of a small area of the wings [9].

warns them of the presence of any predators. The history behind the development of man-made nanophotonic structures is a long one with various origins. Investigations into historical artworks have revealed that the artisans, unknowingly, practised a primitive form of nanotechnology by incorporating metallic nanoparticles as colorants. The Roman Lycurgus cup [Fig. 3] with its unusual display of optical effects is one of the exceptional achievements of the ancient glass industry [11]. Other notable examples include stained glass windows [12,13], medieval pottery and ceramics [14,15], etc.

Present day nanophotonics is the result of decades long research and investigation into various sub-fields of science and engineering integrated together leading to interdisciplinary fields such as photonics, nonlinear optics, laser science, nanofabrication techniques, plasmonics, etc. The efficiency of nanophotonic devices rely on strong light matter interaction and large effective nonlinearities of the nanostructure which is achieved by the confinement of light in sub-wavelength regimes. Engineering of artificial materials began with structures of micrometer-scale dimensions, however, gradual improvement in the novel nanofabrication techniques over the past few decades have per-

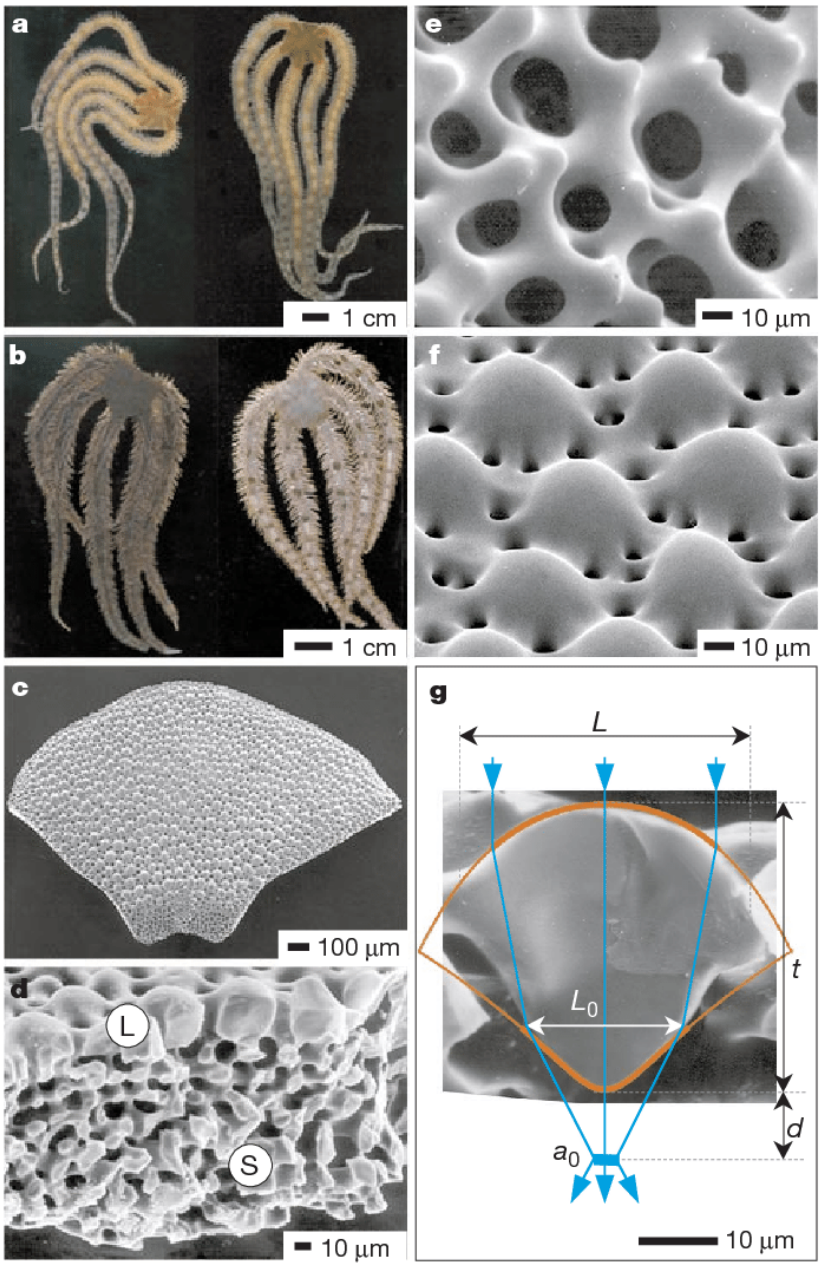

Figure 2: (a) Light-indifferent species Ophiocoma pumila. (b) Light-sensitive species O. wendtii. (c) Scanning electron micrograph (SEM) of a dorsal arm plate (DAP) of O. wendtii. (d) SEM of the cross-section of a fractured DAP from O. wendtii. (e) SEM of the peripheral layer of a DAP of O. pumila. (f) SEM of the peripheral layer of a DAP from O. wendtii with lens structures. (g) Highly magnified SEM of the cross-section of an individual lens in O. wendtii [10].

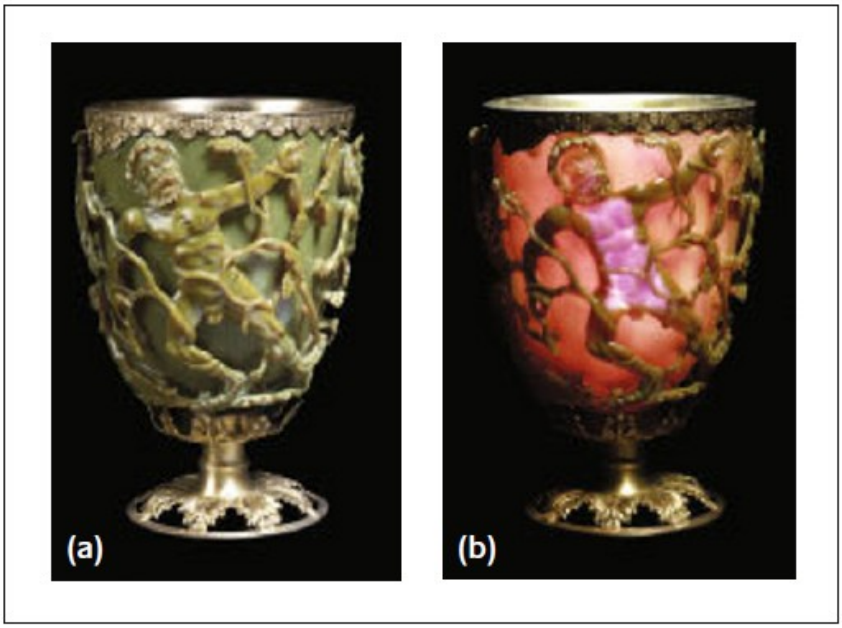

Figure 3: The Lycurgus Cup. It appears opaque with a greenish-yellow color tone in reflected light (a), and turns to a translucent ruby color in transmitted light (b) [11].

mitted the fabrication of nanoscale structures with exceptional control over confinement of light at the nanoscale dimensions. Developments of techniques such as electron or focused ion beam lithography, electrically induced nanopatterning, etc., made such small structures possible that can be precisely engineered to exhibit unique nonlinear optical properties with unprecedented control over its response.

The extraordinary performance of metallic or metal-dielectric nanostructures are due to the enhancement of local fields achieved through plasmonic effects or the resonant excitation of surface plasmon polaritons (SPPs) [2, 16, 17]. The effective nonlinear response of such structures gain a significant boost because of the presence of strong local fields at the SPP resonances; in contrast to the macroscopic bulk media where the efficiency depends on their intrinsic nonlinear susceptibility and phase matching conditions. Years of investigations have revealed that the properties of light can be easily modified and controlled at wavelength or sub-wavelength scales by controlling the physical or structural nature of these nanostructures. Nanostructures such as nanoparticles and nanoclusters or arrays of such nanoparticles forming metasurfaces or metamaterials made up of noble metals or metal-dielectric combined materials have been fabricated and studied for diverse applications [16, 18, 19]. In addition to the enhancement of the near field due to plasmonic effects, geometrical resonances can also be controlled by the design of the nanostructures [20–22]. Experimental investigations into efficient nonlinear response from nanostructures backed by numerical computations have been widely reported [16, 23]. In particular, SHG from metasurfaces [24], nanoparticles [20, 21, 25], nanostructures [26] have been extensively studied experimentally [16, 20, 25, 27, 28] and by diverse numerical

methods such as the finite difference in the time domain method (FDTD) [29, 30], the surface integral equation (SIE) method [31–33], the finite element (FEM) [21] technique, the discrete dipole approximation (DDA) [34], etc.

Although plasmonic structures possess large optical nonlinearities and have exhibited tremendous potential in various applications, they suffer from large ohmic losses and are not always compatible for integration with complementary metal-oxide-semiconductor (CMOS) circuits. Hence, the need for low-loss plasmonic materials arises which remains a growing area of interest. Investigating nonlinear properties of structures made of heavily doped semiconductors and loss-less dielectric materials have become a promising sub-field of nonlinear nanophotonics. Recently, nanostructures fabricated from *all-dielectric* materials have been reported to exhibit extraordinary efficiencies [35–37]. Low absorption in a large domain of the electromagnetic spectrum coupled to Mie type localized resonances, ability to support both electric and magnetic resonances, and low ohmic losses make these high-refractive index dielectric nanostructures highly suitable for nonlinear nanophotonic applications. Various groups investigated enhanced SHG from gallium arsenide (GaAs) nanoresonator arrays [38] and indium gallium nitride/gallium nitride (InGaN/GaN) multiple quantum well [39] metasurfaces, aluminium gallium arsenide (AlGaAs) nanoantennas [40, 41], barium titanate ($BaTiO_3$) nanoparticles [42], etc. An experimental investigation with supporting numerical computations for sub-wavelength AlGaAs particles excited by doughnut shaped cylindrical vector beams was reported recently [43]. A theoretical investigation employing multipolar analysis for exploring SHG from $2D$ dielectric particles was also reported [44]. These III-V semiconductors with efficient second order nonlinearities have noncentrosymmetric crystal structure, and possess non-zero intrinsic second order susceptibilities. SHG induced by the presence of extremely high electric field of a terahertz (THz) pulse from centrosymmetric silicon was reported [45]. Strain induced breaking of the centrosymmetry in silicon waveguides leading to SHG was investigated in detail by Castellan et. al [46]. Most recently, efficient SHG from a silicon based microresonator by uniting photo-induced second-order nonlinearity with resonant enhancement [47]. Besides silicon, graphene has also emerged as a promising candidate for SHG [26, 48].

SHG is one of the most common nonlinear optical phenomena investigated due to the wide range of applications it offers. Over the years, many theoretical models and calculations have been reported to explore SH radiation (scattered and reflected, coherent and incoherent) and the efficiency of the conversion process. Here, we will briefly review some of them which will help the readers appreciate the present work. Nonlinear Rayleigh type scattering from small nanospheres perturbed by plane electromagnetic waves was investigated by Dadap et al. [49]. They provided explicit expressions for the scattered second harmonic (SH) light in the small particle limit. An approach to explore the nonlinear Mie scattering from spheres of arbitrary sizes was presented by Beer et al. [50]; they used their model to calculate the SHG and sum frequency generation (SFG) patterns from water droplets in air. Both of these works demonstrated calculations and results for scattered incoherent light. Coherent SHG from an isolated spherical particle illuminated by an inhomogeneous external

field with explicit expressions of its SH response was reported by Brudny et al. [51]. In their work, they calculated contributions from dipolar and quadrupolar moments induced in the spherical particle due to gradients in the external field and presented the spectral response of the SH response tensor, in contrast to the work by Dadap [49] where they used arbitrary values for the second order response and discussed how they could be obtained from experimental measurements. Few years later, Mochán et al. [52] presented their calculation of the SH response for a single nanosphere and a composite constructed from an array of nanospheres perturbed by an inhomogeneous transverse and/or longitudinal fields. A theoretical calculation of the total and angular resolved SH power radiated from an infinitely long cylinder was presented by Valencia et al. [53] and from a finite cylinder by Dadap [54]. It must be pointed out that all of these theoretical models are for symmetrically shaped particles. Second order response, particularly SHG, from metamaterials or nanoparticles with noncentrosymmetric geometry has gained attention over the last decade and has been studied extensively by employing various numerical techniques and in experiments. A comprehensive theoretical study of SHG in metamaterials made up of a distribution of centrosymmetric nanowires was proposed by Biris and Panoiu [55]. Bachelier et al. [21] explored multipolar SHG from noble metal particles. They investigated the effects of the noncentrosymmetric shape and interference between different multipolar contributions using FEM. In another study, a numerical approach using FDTD to study SHG from noncentrosymmetric nanoholes in metal was published by Zhou et al [30].

Although SHG has been more commonly studied, many research groups have reported SFG or DFG from nanostructures. An experimental work to study the vibrational resonance of thiophenol molecule adsorbed on gold nanoparticles using SFG and DFG was published by Pluchery et al. [56]. Mid-infrared generation from DFG in self-assembled gallium arsenide/aluminium arsenide (GaAs/AlAs) near Au nanoparticles was explored numerically by Yan et al. [57]. They discussed effects of the interparticle distance on the efficiency of the nonlinear process and found an optimal distance for enhanced signal generation. A design of an optical frequency mixer using plasmonic nanoantennas resonant at the difference frequency (DF) in the optical or tera-hertz (THz) regime was investigated through full wave numerical simulations employing the FEM method by Chettiar et al. [58]. Enhancement of the nonlinear optical response of plasmonic nanoparticle arrays due to surface lattice resonances was investigated by Huttunen et al. [59]. They used the DDA to explore different nonlinear properties of nanoparticle arrays with emphasis on SFG, DFG and THG. Luca et al. [60] presented a parameter-free hydrodynamic approach to theoretically investigate DFG from plasmonic nanostructures. They used the results of their numerical model to predict the DFG efficiency of doubly resonant gold nanoantennas. Most recently, a theoretical investigation to explore optical rectification from an asymmetric GaAs/AlAs quantum dot coupled to a Au nanosphere illuminated by a strong electromagnetic field was reported [61]. The author discusses how decreasing the distance between the nanosphere and the quantum dot leads to an enhancement of nonlinear optical rectification from the quantum dot when the incident field is polarized along the interparticle separation and observed the opposite effect for light polarized in the perpendicular direction.

It must, however, be remarked that most of the calculations for the different models to study the nonlinear response of nanostructures with noncentrosymmetric geometries are performed numerically. Investigation into analytical theories have not received similar attention and are still few in number, with many being for symmetrical geometries where an exact solution of the problem is possible [49, 51, 53]. Some of the works published on analytical theories of SHG from arbitrary nanoparticles or nanostructures are rough and approximate, calculating the scattering coefficients but taking the nonlinear response as a given input [62]. Last year, selection rules for SHG from nanoparticles made up of noncentrosymmetric crystal structure but with arbitrary shapes was reported by Frizyuk [63]. To the best of our knowledge, analytical calculations of the second order response of a non-symmetrical nanostructure made up of a centrosymmetric material has not been reported. The importance of having analytical calculations resides in the fact that they can be used as standards to test and calibrate numerical methods in simple systems, so they can later be employed confidently to model any complex system. This would greatly simplify and aid the design process of nanostructures with novel geometrical forms. Also, once verified and calibrated, the numerical methods become more trustworthy for other kinds of systems for which no analytic solutions are possible. Numerical results from these verified theories would be valuable before any experimental fabrication of a nanostructure is attempted, thus reducing the cost and time for the development of newer structures. The purpose of the presented work is related to this idea. We begin with a simple nanowire with nonsymmetrical geometry and develop a theoretical method to analytically obtain its SH, DF, and SF response. Later, we design a metamaterial formed of a periodic array of these nanowires and calculate its SH response numerically employing a computational package called *Photonic* [64], written in the programming language *Perl* and its extension *Perl Data Language*, to compare with the analytical results. The program is a free software available on the Comprehensive Perl Archive Network (CPAN). This package was developed by our group to investigate the linear properties of metamaterials and photonic structures by employing an efficient homogenization scheme [65–67] and has been used to study various metamaterial systems [68–70]. The package also includes some modules that implement the calculation of the SH response of binary metamaterials; these modules were applied recently to study the SH response of a nanostructured metamaterial [71]. This work is devoted to the testing and calibration of these modules by comparison with analytical results. During the process of comparison between the numerical and analytical results, we discovered the different shortcomings within the modules which sometimes lead to errors for the SH response. Rectifying and updating the corresponding parts of the modules producing the errors was a part of my doctoral research investigation. The updated package will soon be available on the public platform.

Thesis outline

Chapter 1 introduces the field of nonlinear optics, discusses different second order nonlinear process, and reviews their applications. Chapter 2 presents the theory of the dipolium model which we have employed in our calculations; both analytical and numerical. It also introduces the jellium model with comments on the comparison between the two models and their applicability. Chapter 3 demonstrates our analytical theory to obtain the SH response from an isolated nanowire respectively, providing a detailed description of our calculations, discussion of results, and conclusions from each work. In Chapter 4, we generalize our theory to describe any three wave-mixing process with an emphasis on DFG from the nanowire. The numerical method of homogenization to obtain effective medium response of the metamaterial is introduced and explained in Chapter 5, with a detailed account of the method to calculate the SH response of the metamaterial. We also provide a discussion of the numerical results and their comparison with those of the analytical case. After a detailed discussion of the origin of some discrepancies, we describe some strategies for improving the numerical calculations and report on the advances of their implementation. Finally, we present our conclusions in Chapter 6.

1 Nonlinear optics

Nonlinear optics is a branch of science that deals with phenomena emerging from the interaction between a strong beam of light and a material medium [72]. The effects of this interaction include both modifications in the optical properties of the nonlinear medium and in the behavior of the light beam within the medium. At low illumination power, the properties of the medium remain independent of the magnitude of the electromagnetic fields. In this regime, the superposition principle holds true allowing light beams of different frequencies to pass through or get reflected from the medium without interacting with each other. However, the superposition principle is no longer valid for highly potent beams which can modify the optical properties of the medium. In such a situation, multiple beams traversing the medium interact with each other by exchanging energy and momentum through the medium, thus generating waves with new frequencies. For such processes to be efficient, beams with sufficiently high intensity are required, like those provided by laser light sources only. That is why these effects were unobserved until the development of the laser [73] allowed the first measurement of second harmonic generation [74]. From then on there has been continuing interest in the field with extensive research leading to significant developments. This opened the door to investigations in diverse sub-fields such as parametric amplification [75–79], phase modulation [80–84], harmonic generation [71,79,85,86], four wave mixing [87–90], pulse compression [91–93] and generation of super continuum [94–96]. Aside from the fundamental research on these light-matter interaction processes, nonlinear optics also paved the way for novel photonic devices [1,97] with applications in various fields of science and engineering [98,99].

Optical processes are usually described in terms of the response of a medium to an external electromagnetic field, the polarization $\boldsymbol{P}$ induced in the system due to electronic motion. To include the nonlinear effects produced by an intense perturbing field, the induced polarization in the media is expressed as a power series in the external electric field $\boldsymbol{E}$,

$$\boldsymbol{P} = \chi^{(1)}\boldsymbol{E} + \boldsymbol{\chi^{(2)}EE} + \boldsymbol{\chi^{(3)}EEE} + \ldots, \tag{1.1}$$

where $\boldsymbol{\chi}^{(n)}$ is the nth order susceptibility tensor. We must point out that the above expression is valid only within the electric dipole approximation, i.e. when the polarization is described by dipole driven transitions only. However, the contributions of higher order multipolar transitions, such as the quadrupolar transitions, may not be negligible and add correction terms to the net polarization induced in the medium, i.e., to Eq. (1.1). A component of the second order polarization induced due to an electric quadrupolar transition leading to a nonlinear dipole moment would have the form $\chi^{(2)}_{ijkl} E_j \partial_k E_l$. The presence of spatial derivatives indicate that the response of the medium at a point in the medium not only depends on the external field at that point but also on the variations in the field around it. This response of the medium is termed *non-local*, in contrast to the *local* response which is dependent only on the value of the field at the same point.

The first term in Eq. (1.1) describes the linear response of the material, which has found applications in conventional optical devices such as lenses, mirrors, diffraction gratings, etc. As the intensity of the incident electromagnetic (EM) field increases, for example, when a strongly focused laser beam is incident on the media, the linear term alone is not sufficient to explain the observed optical properties. The higher order terms must be taken into consideration to understand the origin of the nonlinear effects. We must point out that in certain circumstances a nonlinear effect may appear with low intensity of illumination due to a cumulative effect of many individual processes, for example in photochromic glasses or phase conjugated mirrors. The quantities $\boldsymbol{\chi}^{(2)}$ and $\boldsymbol{\chi}^{(3)}$ in Eq. (1.1) are the second- and the third- order nonlinear susceptibility tensors respectively. Both of these nonlinear terms are explored more often than others, being important for most applications. A simple order of magnitude analysis of the size of the nonlinear quantities can be done in the following manner. The lowest order correction $\boldsymbol{P}^{(2)}$ would be comparable to the linear polarization $\boldsymbol{P}^{(1)}$ when the external perturbing field E_{ex} is of the order of the internal atomic field E_{at}. With $\chi^{(1)}$ being of the order of unity, it is appropriate to expect that the quadratic susceptibility $\chi^{(2)}$ will be of the order of $\chi^{(1)}/E_{\text{at}} \sim 1/E_{\text{at}}$. Similarly $\chi^{(3)}$ will be of the order of $\chi^{(2)}/E_{\text{at}} \sim \chi^{(1)}/E^2_{\text{at}}$. Thus, each term in Eq. (1.1) is of the order of $(E_{\text{ex}}/E_{\text{at}})^{n-1}$ which is typically much smaller than unity for any $n > 1$. This allows one to terminate the series after the lowest order relevant nonzero nonlinear correction in order to explore and analyze a given nonlinear optical process. The internal atomic fields are of the order of $E_{\text{at}} = e/a_b^2$ where a_b is the Bohr radius. This makes the second order susceptibility of the order of

$$\chi^{(2)} \sim a_b^2/e \sim 1/nea_b \tag{1.2}$$

where we have used $n = 1/a_b^3$ as an estimate for the number density.

The type of nonlinear response exhibited by a material is strongly determined by the presence of different symmetry properties. Materials can be broadly classified into two groups; those that possess a center of inversion, called centrosymmetric materials, and those that do not called non-centrosymmetric materials. Fig. 1.1 illustrates these two crystal structures. For a centrosymmetric crystal [Fig. 1.1 (b)], all even order terms in the expansion [Eq. (1.1)], related to the even order

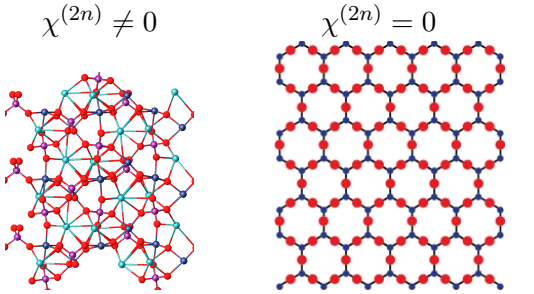

Figure 1.1: Crystal structure of (a) KTP (noncentrosymmetric), (b) $\alpha-$quartz (Centrosymmetric)

nonlinear effects vanish. This is because applying an inversion operator would leave both the even order products of the electric field and the nonlinear susceptibility invariant, but change the sign of the induced electric dipole moment per unit volume, i.e. the polarization. This is illustrated by the following simple relation,

$$-\boldsymbol{P}^{(2n)} = \boldsymbol{\chi}_I^{(2n)}(-\boldsymbol{E})^{2n} = \boldsymbol{\chi}_I^{(2n)}\boldsymbol{E}^{2n} = \boldsymbol{\chi}^{(2n)}\boldsymbol{E}^{2n} \implies \boldsymbol{\chi}^{(2n)} = 0 \qquad \forall\, n. \tag{1.3}$$

where the subscript I is used to denote the inversion operation and the relation $\boldsymbol{\chi}_I^{(2n)} = \boldsymbol{\chi}^{(2n)}$ holds true due to centrosymmetry in the material. We remark that Eq. (1.3) also holds true only under the *dipolar approximation*. A dipolar SH signal may still be obtained from the surface of such systems where the inversion symmetry is locally lost. Hence, these processes serve as important probes for surface imaging and spectroscopy [100–102]. Note that the bulk signal vanishes only in the dipolar approximation; there may be a second order response from the centrosymmetric bulk due to the excitation of electric quadrupolar or magnetic dipolar moments. Artificial materials, such as nanoparticles, constructed from centrosymmetric materials may exhibit second order response controlled by their geometry. Hence, exploring the possibility of efficient second order conversion processes producing an SH, SF, or DF signal simply by arranging their geometry would be interesting and useful. On the other hand, materials with a non centrosymmetric crystal structure [Fig. 1.1 (a)] do not possess such symmetry properties and thus, within them, the even order nonlinear processes are allowed. For example, Lithium Niobate ($LiBNO_3$) has a non-zero $\chi^{(2)}$ and is most commonly used by the laser industry to produce green (0.53μ) laser by doubling the output frequency of a Nd:YAG laser [103]. In this work, we restrict ourselves to the discussion of only the second order nonlinear properties of nanostructures made up of centrosymmetric materials. Our interest in exploring the second order properties of centrosymmetric materials stems from the fact that metals and many dielectric materials, such as Silicon which forms an integral part of countless nonlinear photonic devices possesses a centrosymmetric crystal structure. They have received increasing attention over the years due to their extraordinary performance and potential for different application purposes.

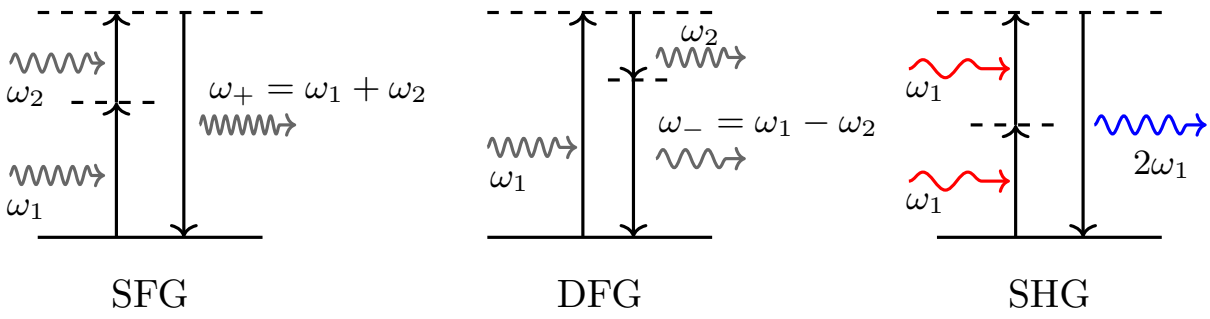

Figure 1.2: Energy level diagrams to illustrate different second order nonlinear processes. Horizontal solid lines indicate the real ground states of the system while the dashed represents the excited states to which virtual transitions occur, indicated by vertical arrows.

1.1 Second order nonlinear processes

We begin by considering two monochromatic laser beams with frequencies ω_1 and ω_2 incident on a nonlinear material with nonzero second order susceptibility $\boldsymbol{\chi}^{(2)}$. The total external electric field can be represented as

$$\boldsymbol{E}(t) = \boldsymbol{E_1} e^{-i\omega_1 t} + \boldsymbol{E_2} e^{-i\omega_2 t} + c.c. \tag{1.4}$$

where *c.c.* stands for complex conjugate. We substitute Eq. (1.4) into Eq. (1.1) and write down the second order term corresponding to the quadratic polarization $\boldsymbol{P}^{(2)}$. We obtain,

$$\begin{aligned}\boldsymbol{P}^{(2)}(t) = \boldsymbol{\chi}^{(2)}[&\boldsymbol{E}_1\boldsymbol{E}_1 e^{-i2\omega_1 t} + \boldsymbol{E}_2\boldsymbol{E}_2 e^{-i2\omega_2 t} + 2\boldsymbol{E}_1\boldsymbol{E}_2 e^{-i(\omega_1+\omega_2)t} + 2\boldsymbol{E}_1\boldsymbol{E}_2^* e^{-i(\omega_1-\omega_2)t} + c.c. \\ &+ 2\{\boldsymbol{E}_1\boldsymbol{E}_1^* + \boldsymbol{E}_2\boldsymbol{E}_2^*\}].\end{aligned} \tag{1.5}$$

Each term in the expansion [Eq. (1.5)] describes a different second order process and the resulting nonlinear polarization generates an outgoing radiative field with distinct frequency components. The second order nonlinear processes take into account those photon-photon interactions within materials that lead to various wave-mixing effects such as the generation of the sum (SFG) ($\omega_+ = \omega_1 + \omega_2$) or the difference (DFG) ($\omega_- = \omega_1 - \omega_2$) of the two incident frequencies ω_1 and ω_2, or the conversion of each of these input signals into their second harmonics (SH) $2\omega_1$ or $2\omega_2$ and their complex conjugate terms. Fig. 1.2 illustrates the energy level diagram for these processes. The last two terms correspond to a quadratic process where no electromagnetic radiation field is generated but only a quasi-static nonlinear polarization. This process is known as optical rectification (OR). It must be pointed out that for simplicity we have written the $\boldsymbol{\chi}$ tensor independent of frequencies, however, it does depend on the process and the frequencies of the electromagnetic waves involved in it.

Sum/Difference Frequency Generation

In SFG process, two incoming photons are destroyed to create a new photon with a frequency equal to the sum of the incoming photons, satisfying the energy conservation principle. Fig. 1.2 (left panel) illustrates the energy level diagram for the process. When a material is illuminated by an electromagnetic source, photons are absorbed to create electron-hole pairs within the medium which then recombine to emit photons with the same energy. However, in certain situations, the excited electron may interact with another photon and get excited to a higher energy level before recombination occurs. In such cases, the new photon generated will have energy different from the two initial photons. Note that such processes take place in general as a result of nonresonant virtual transitions, as the incident photon energy is not sufficient for an absorption process to occur. Hence, a nonlinear virtual transition, disobeying the law of energy conservation occurs, until a new photon is emitted with a frequency equal to the sum of the incident frequencies. This violation of the conservation of energy is allowed by the Heisenberg uncertainty principle, but only for a short time interval. Hence, these virtual transitions are very short-lived, making the nonlinear transitions essentially instantaneous and the process coherent. It must be pointed out that in the overall process of the annihilation of the incoming photons and the generation of the new photon, the total energy is conserved; the energy conservation is violated only in the transient intermediate transitions.

Difference frequency generation (DFG) is the second order process where the output photon has a frequency equal to the difference of two interacting photons (center panel of Fig. 1.2). Although, DFG seems similar to SFG, both processes are quite different. Note that in order to create a photon of the difference frequency (DF), $\omega_- = \omega_1 - \omega_2$, a photon of higher frequency ω_1 must be destroyed and that of ω_2 generated. Hence, the lower frequency source gets amplified in the process of difference frequency generation. In this process, a photon with frequency ω_1 is absorbed populating an excited state of the system through virtual transitions, which then decays generating two photons with frequency ω_2 and ω_- in the presence of an incoming wave of frequency ω_2.

Typical applications of both of these processes include generation of intense light sources by mixing of frequencies from existing lasers, spectroscopy and imaging [100, 104]. Sum frequency generation is commonly used in the generation of UV-Vis light sources [105–107]. Difference frequency generation (DFG) finds applications in the generation of mid-infrared sources which are essential for spectroscopic studies of gases [108–110] and to generate terahertz radiation [111, 112]. In addition to the generation of different light sources at varied frequency regimes, both of these processes serve as excellent probes for studying surfaces and interfaces [113–117]. Being second order processes, they are prohibited in the bulk of centrosymmetric media with only a response sensitive to surface from such materials. We reemphasize that this is valid only within the electric dipole approximation and that bulk contributions from higher multipoles may be present. Conversion of optical oscillations to radio frequencies have been done for quite some time and by employing the technique of femtosecond laser frequency combs an optical clock based on DFG in a Ti:sapphire ring laser has been

demonstrated by Ref. [118].

Second Harmonic Generation and Optical Rectification

Second harmonic generation is a process akin to SFG except for the fact that both the incoming photons have the same frequency. Thus, two photons of equal frequency get annihilated to create a new photon with double the frequency in a single coherent chain of quantum processes. A schematic energy level diagram to illustrate the transition is shown in the right panel of Fig. 1.2. As in SFG, two incoming photons interact with the electrons of the system to populate higher energy states through an extremely fast virtual transition followed by a similar recombination process to generate a photon with double the incident frequency. SHG in turn has similar applications as SFG in the generation of new frequencies, spectroscopy of surfaces and interfaces, and imaging [101, 106, 116, 117, 119].

Optical rectification (OR) is a process in which a steady nonlinear polarization is induced, which can be imagined as a special case of DFG where the difference frequency of some light wave interacting with itself is generated. This zero frequency component causes a non-zero time averaged value resulting in a static nonlinear polarization and fields or a DC current. Like DFG, optical rectification is also employed in the generation of terahertz radiation [120, 121]. To this end, when a laser with femtosecond pulse width is made incident on a nonlinear system, the different frequency components of the same pulse interact with each other to produce a beating polarization. This leads to emission of electromagnetic fields in the terahertz (THz) regime [121, 122]. Another way to understand this is that an optical rectification of the central frequency of the pulse occurs during the short duration of the pulse, and then nothing, i.e., a time dependent optical rectification takes place which oscillates in the THz frequency.

2

Theoretical models

Second harmonic generation (SHG) from calcite, a centrosymmetric crystal, was first observed by Terhune et al. [123]; one year after the experimental discovery of SHG in 1961 by Franken et al. [74]. Ever since, investigation of second order nonlinearities of centrosymmetric media have drawn much attention. The interest in the field has increased rapidly in the last few decades due to the commercialization of numerous applications. The earliest theoretical models to explore SHG and other second order effects from centrosymmetric media were developed concurrently with the first reports of the experimental studies. Most of the initial studies were oriented towards qualitative estimates of the contribution of various mechanisms to the second order response of centrosymmetric media. Decades of rigorous research by various groups has led to systematic and sophisticated computations and development of theoretical models allowing us to investigate the second order response of not only simple systems but also complex nanostructures. Section 2.1 of this chapter reviews various theoretical models that have been reported over the years to calculate the second order response of the bulk and planar interfaces of centrosymmetric media.

The analytical and numerical calculations in this work employs the *dipolium* model which was developed by Mendoza and Mochán [124]. In ref. [124], they calculate the components of the surface and the bulk second harmonic (SH) susceptibility tensor of semi-infinite homogeneous centrosymmetric systems. The theory was developed initially for dielectric materials. This was followed by a work by Maytorena et al. [125] where the theory was extended to include the sum frequency (SF) response. Section 2.2 provides an elaborated discussion about the *dipolium* model explicitly calculating the difference frequency (DF) response. Section 2.3 briefly describes how the sum frequency (SF) and the SH response can be identified from the DF response. In ref. [125], it was shown that the results of the model are applicable to metallic systems through a comparison with a calculation done with a hydrodynamic model. We will not indulge into a detailed discussion about it here, but for the sake of completeness of this work, a brief description of the said hydrodynamic model and a discussion on the comparison between both models is given in Sec. 2.4.

2.1 Theoretical models for second order response from planar surface

The pioneering work of Pershan [126] in 1963 paved the way for the development of different theories and models to study SHG from centrosymmetric media. He derived the linear and nonlinear macroscopic electromagnetic equations for non-dissipative media using a time averaged energy function. From them, he predicted the order of magnitude of several nonlinear effects. A few years later, Bloembergen et al. [127] gave a theoretical calculation of SHG from media with inversion symmetry considering only a quadrupolar contribution. They also performed experiments on semiconductors and noble metals. Rudnick and Stern [128] presented a work in 1971 which had a paramount effect on research in SHG from the surface. They stressed the significance of a systematic and careful analysis of various contributions of nonlinear currents induced in the system. They presented a calculation of the nonlinear susceptibility and the radiated fields at the SH from a metal surface describing in detail the origins and effects of different bulk and surface currents. They further parameterized the nonlinear susceptibility components using frequency dependent dimensionless parameters. These parameters were later verified using different techniques and a confirmation of the estimate of these parameters was published by Sipe et al [129]. They formulated a hydrodynamic theory to calculate SHG from a metal surface by dividing the metal in to *bulk* and *selvedge* (signifying a very thin region at the surface) regions. Generalizing their basic equations, Corvi and Schaich [130] evaluated and presented in detail a numerical solution for the SHG efficiency. A phenomenological method for treating the surface SHG was presented by Mizrahi and Sipe [131]. To calculate SHG they considered a dipole sheet as a model to describe the surface. They considered different experimental geometries and presented expressions for the SH radiation power with their dependence on polarization and angle of incidence. They also included contributions from the bulk to the SH radiation. However, most of these calculations were not sufficient to explain all the different components correctly. These results could be applied easily to metals and extended in some cases to semiconductors.

A microscopic theory for SHG from crystals was given by Schaich and Mendoza [132] in which the material is assumed to be an array of point dipolar polarizable entities called *dipolium*. Their work proved an essential step towards a different approach from the existing models and was applied to semiconductors and noble metals. However, their results were only qualitative and needed further development to apply to a realistic material. Another model based on the similar dipolium was developed by Mendoza and Mochán [124]. The model calculates the second order response and nonlinear reflectance of a semi-infinite, isotropic, and centrosymmetric system in terms of its linear response. This simple model yields analytical expressions for the second order nonlinear susceptibility and efficiency of SHG from the system by assuming a harmonic-oscillator-like response of each polarizable entity to an inhomogeneous local field. These results were written in terms of the linear response of the system, and thus, they might be used for obtaining the spectra of the second order

response of arbitrary centrosymmetric systems whose linear response is known from experiments or from linear response theories. Since the effects of crystal structure have not been considered in the calculation of the response, the results would lack any related features. This is in contrast to some of the earliest measurements of SHG which were performed with a fixed frequency laser and for which the effects of polarization and orientation on SHG were studied [127]; in them, the crystal symmetries were emphasized but the spectral dependence was disregarded. We will use the results of the dipolium model for our calculations, the details of which will be described in the following section.

Although, SHG have been studied more extensively, theoretical investigation into SFG and DFG from centrosymmetric semi-infinite isotropic media have not been neglected. Sum frequency generation spectroscopy was first observed and reported by Shen et al. [133]. A theoretical investigation of SFG and DFG from isotropic surfaces with a discussion on the properties of the surface nonlinear susceptibility was reported [134]. Petukhov proposed a systematic theoretical investigation of SFG in reflection geometry from a centrosymmetric material surface [135]. He presented a phenomenological theory of SFG and provided the expressions for the radiated SFG field in terms of the surface and bulk responses for isotropic metallic surfaces within the jellium model. Later, Petukhov and Rasing [136] published their work on the calculation of quadrupolar contribution to the infrared-visible SFG from noble metals taking the effects of crystallinity into consideration. The energy exchange between the three waves using Manley Rowe relations within a centrosymmetric medium was also reported [137]. A simple model for SFG from isotropic centrosymmetric surfaces considering the *jellium* and the *dipolium* model was reported by Maytorena et al. [125]. They contrasted the results of both the models and found an agreement between them. They also compared their results to the work of Petukhov [135] and discussed the differences in the bulk contributions. They, later, extended this work to include the effects of non-locality by choosing a nonlocal *jellium* system [138]. The basic theory for SFG, both reflected and transmitted, from an interface between two semi-infinite centrosymmetric system was also reported [139]. Wang et al. [140] reported a theoretical investigation of SFG from a thin metal-film in the Kretschmann configuration.

2.2 Dipolium model : DF response

In this section we describe a simple model which permits the calculation of the components of the surface and the bulk quadratic susceptibility tensors of a centro-symmetric, semi-infinite system. Within the model, the system is represented by a semi-infinite *dipolium* [124], a homogeneous array of polarizable entities which respond harmonically to an external perturbing field [Fig. 2.1]. The model was originally developed to obtain analytical expressions for the surface and bulk SH response and the efficiency of SHG [124]. The frequency dependent SH response tensors of the system were obtained in terms of its linear response functions. Ref. [124] was among the first few spectral calculations; it was only later that other theories were put forward. A few years later, the

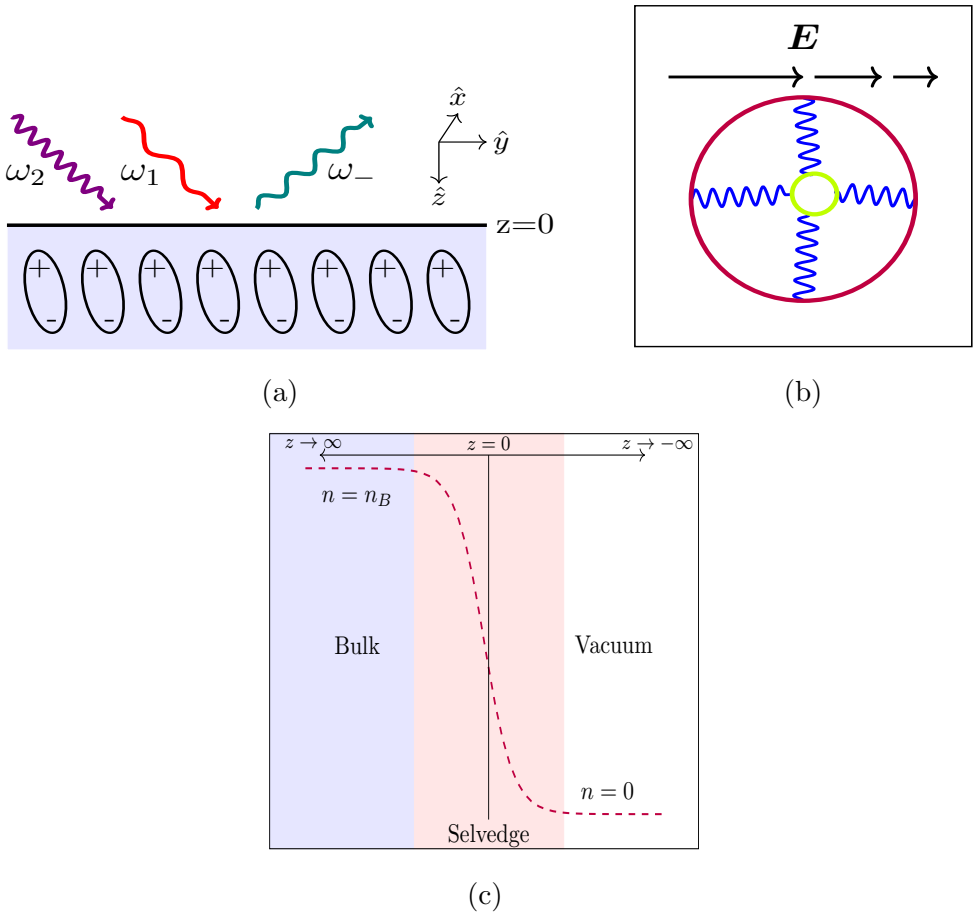

Figure 2.1: A schematic illustration of the Dipolium model. (a) Homogeneous semi-infinite system, (b) model harmonic entity which is polarized by a non homogeneous field, (c) number density profile for the polarizable entities.

theory presented in ref. [124] was extended to include the non-degenerate case of SFG [125]. The theoretical approach to calculate the components of the response tensors for both of these second order processes is essentially the same except for some additional terms that do not contribute in the degenerate, SH case. The DF response can be obtained from the SF response by making appropriate changes to the nonlinear equations and choosing the corresponding conjugated linear response. Since the analytical expressions of the components of the DF susceptibility tensor have not been published explicitly, we will illustrate the methodology of the *dipolium* model through their calculation. We will begin with a description of the model and its basic assumptions before going into a detailed discussion of the procedure to obtain the analytical expressions for the quadratic response. As mentioned in the previous paragraph, the model represents the medium as a semi-infinite array of harmonic polarizable entities. The dipole number density n of this distribution is assumed to have a constant value n_B in the bulk and zero in the vacuum, and to vary rapidly between these two in a thin selvedge region across the surface [Fig. 2.1]. We would like to remark

that we choose this transition in the density across the surface to interpolate continuously between its two asymptotic values to avoid an inherent ambiguity present in models with abrupt interfaces, namely, some field components are discontinuous and their gradients are singular precisely at the discontinuity, so the nonlinear response at the surface would not be well defined. Nevertheless, by obtaining the response corresponding to a continuous one we can unambiguously take afterwards the limit of an abrupt interface. We also assume that the response of all the particles to the polarizing field are identical. Although harmonic systems are considered to respond linearly to a driving field, they do respond non-linearly to spatially inhomogeneous fields. The field inhomogeneity yields a small contribution of order a_d/λ in the bulk of the media, where a_d is the size of the dipole and λ is the wavelength of the incident light. The normal component of the linear electric field exhibits a rapid variation across the surface reminiscent of the discontinuity it suffers at an abrupt surface. The corresponding large gradient in the perturbing field results in a large surface contribution to the nonlinear response of the system. We will calculate the quadratic electric dipole, quadrupole moment, and magnetic dipole moment induced in the bulk and the surface of the system to get a generalized polarization. From it we will obtain a bulk nonlinear susceptibility and, integrating across the selvedge, we will identify the surface nonlinear polarization. From them we will obtain the susceptibility corresponding to the DFG process.

Each polarizable entity is represented by an electron of charge $-e$ and mass m at a distance $\boldsymbol{x}$ from its equilibrium position $\boldsymbol{r}_0$ to which it is bound by a harmonic force with resonant frequency ω_0. The equation of motion of each of these electrons under the influence of a spatially varying external electromagnetic field is given by,

$$m\ddot{\boldsymbol{x}} = -m\omega_0^2\boldsymbol{x} - \frac{m}{\tau}\dot{\boldsymbol{x}} - e\boldsymbol{E}(\boldsymbol{r},t) - \frac{e}{c}\dot{\boldsymbol{x}}\times\boldsymbol{B}(\boldsymbol{r},t), \tag{2.1}$$

where we have included a dissipative term with τ as the corresponding lifetime parameter. It is to be noted that the actual position of the electron is $\boldsymbol{r} = \boldsymbol{r}_0 + \boldsymbol{x}$ and the field must be evaluated at this position and not at the equilibrium position $\boldsymbol{r}_0$. Assuming the displacement $\boldsymbol{x}$ of the electrons to be smaller than the scale of variation in the perturbing field, we can expand the polarizing field as a Taylor series,

$$\boldsymbol{E}(\boldsymbol{r}_0+\boldsymbol{x},t) \approx \boldsymbol{E}(\boldsymbol{r}_0,t) + \boldsymbol{x}\cdot\nabla\boldsymbol{E}(\boldsymbol{r}_0,t) + \cdots . \tag{2.2}$$

Substituting Eq. (2.2) in the equation of motion [Eq. (2.1)], we get

$$m\ddot{\boldsymbol{x}} = -m\omega_0^2\boldsymbol{x} - \frac{m}{\tau}\dot{\boldsymbol{x}} - e\boldsymbol{E}(\boldsymbol{r}_0,t) - e\,\boldsymbol{x}\cdot\nabla\boldsymbol{E}(\boldsymbol{r}_0,t) + e\,\dot{\boldsymbol{x}}\times\int^t dt'\,\nabla\times\boldsymbol{E}(\boldsymbol{r_0},t') + \cdots , \tag{2.3}$$

where we have used the relation $\boldsymbol{B}(\boldsymbol{r},t) = -c\int^t dt'\nabla\times\boldsymbol{E}(\boldsymbol{r},t')$ for the magnetic field. This equation resembles that of a forced damped parametric harmonic oscillator with ω_0 equal to its natural resonant frequency. Notice that the second term is related to the damping in the system and the last three terms correspond to the driving forces. It must be pointed out that the coefficients of $\boldsymbol{x}$ and $\dot{\boldsymbol{x}}$ in the last two terms are not constant but dependent on the field gradients. The presence of

these terms modulate the restoring force, the *stiffness* of the oscillator varies in time, thus making Eq. (2.3) analogous to that of a parametric oscillator. Hence, even though the harmonic oscillator is a linear system, the spatial variations of the perturbing fields, in this case, have led to a nonlinear system.

We now choose two different sources of electromagnetic waves oscillating at frequencies ω_1 and ω_2 to drive the system. The total external field is given by

$$\boldsymbol{E}(\boldsymbol{r},t) = \boldsymbol{E}_1(\boldsymbol{r})e^{-i\omega_1 t} + \boldsymbol{E}_2(\boldsymbol{r})e^{-i\omega_2 t} + c.c., \tag{2.4}$$

where $\boldsymbol{E}_1(\boldsymbol{r})$ and $\boldsymbol{E}_2(\boldsymbol{r})$ are the complex amplitudes of the field components and *c.c.* stands for the complex conjugate terms. Since the incident optical fields are usually much smaller than the microscopic atomic fields, we employ a perturbative approach to solve Eq. (2.3) by expanding the solution in powers of $\boldsymbol{E}$,

$$\boldsymbol{x}(t) = \boldsymbol{x}^{(1)}(t) + \boldsymbol{x}^{(2)}(t) + \cdots . \tag{2.5}$$

The linear solution $\boldsymbol{x}^{(1)}(t) = \sum_g \boldsymbol{x}_g^{(1)} e^{-i\omega_g t} + c.c.$, like the perturbing electric field, is a superposition of two oscillations with amplitudes $\boldsymbol{x}_1^{(1)}$ and $\boldsymbol{x}_2^{(1)}$ corresponding to the incident frequencies ω_1 and ω_2 respectively, both obeying the equation of a forced linear harmonic oscillator given by

$$-m\omega_g^2 \boldsymbol{x}_g^{(1)} = -m\omega_0^2 \boldsymbol{x}_g^{(1)} + im\frac{\omega_g}{\tau}\boldsymbol{x}_g^{(1)} - e\boldsymbol{E}_g(\boldsymbol{r}_0,t), \tag{2.6}$$

with $g = 1, 2$. We can utilize this linear solution to calculate the induced linear dipole moment, defined as $\boldsymbol{p}_g^{(1)} = -e\boldsymbol{x}_g^{(1)}$. After substituting the linear solution $\boldsymbol{x}_g^{(1)}$ of Eq. (2.6), we obtain $\boldsymbol{p}_g^{(1)} = \alpha_g \boldsymbol{E}_g$ where α_g is the linear polarizability at frequency ω_g,

$$\alpha_g = \frac{e^2/m}{\mathscr{D}_g}, \tag{2.7}$$

with the denominator being

$$\mathscr{D}_g = \omega_0^2 - \omega_g^2 - i\omega_g/\tau, \tag{2.8}$$

for $g = 1, 2$.

We now proceed to find the solution of Eq. (2.3) at the second order, the equation for which is

$$\begin{aligned} m\ddot{\boldsymbol{x}}^{(2)}(t) = &- m\omega_0^2 \boldsymbol{x}^{(2)}(t) - \frac{m}{\tau}\dot{\boldsymbol{x}}^{(2)}(t) - e\boldsymbol{x}^{(1)}(t)\cdot\nabla\boldsymbol{E}(\boldsymbol{r}_0,t) \\ &+ e\dot{\boldsymbol{x}}^{(1)}(t) \times \int^t dt' \nabla \times \boldsymbol{E}(\boldsymbol{r_0},t'). \end{aligned} \tag{2.9}$$

Notice that once the solution for $\boldsymbol{x}^{(1)}$ obtained from Eq. (2.6) is substituted, the driving terms in this equation will become quadratic in $\boldsymbol{E}$ with the following frequency components: DC, second harmonics of both incident frequencies ($2\omega_1$ and $2\omega_2$), the sum frequency ($\omega_+ \equiv \omega_1 + \omega_2$), and

the difference frequency ($\omega_- \equiv \omega_1 - \omega_2$). Our interest is to find the solution to the above equation corresponding to the difference frequency (DF) component, with amplitude $\boldsymbol{x}_-^{(2)}$, where $\omega_- = \omega_1 - \omega_2$, and which obeys

$$\begin{aligned}\omega_-^2\, \boldsymbol{x}_-^{(2)} =& \omega_0^2 \boldsymbol{x}_-^{(2)} - i\frac{\omega_-}{\tau}\boldsymbol{x}_-^{(2)} + \frac{e}{m}\left(\boldsymbol{x}_1^{(1)} \cdot \nabla \boldsymbol{E}_2^* + \boldsymbol{x}_2^{(1)*} \cdot \nabla \boldsymbol{E}_1\right) \\ &+ \frac{e}{m}\left[\left(\frac{\omega_1}{\omega_2}\right)\boldsymbol{x}_1^{(1)} \times \nabla \times \boldsymbol{E}_2^* + \left(\frac{\omega_2}{\omega_1}\right)\boldsymbol{x}_2^{(1)*} \times \nabla \times \boldsymbol{E}_1\right], \end{aligned} \tag{2.10}$$

where the superscript $(*)$ on any quantity signifies its complex conjugate. Notice that in writing the previous equation, the explicit time dependence has been left out and only complex amplitude is written. Henceforth, we will use this notation for all equations and drop the explicit time dependence. Using the solution of Eq. (2.10), the quadratic DF dipole moment induced within the bulk of the media $\boldsymbol{p}_-^{(2)} = -e\boldsymbol{x}_-^{(2)}$ can be written as,

$$\begin{aligned}\boldsymbol{p}_-^{(2)} = -\frac{1}{e}\alpha_- \Bigg[&\alpha_1\left(\boldsymbol{E}_1 \cdot \nabla \boldsymbol{E}_2^* + \frac{\omega_1}{\omega_2}\boldsymbol{E}_1 \times (\nabla \times \boldsymbol{E}_2^*)\right) \\ &+ \alpha_2^*\left(\boldsymbol{E}_2^* \cdot \nabla \boldsymbol{E}_1 + \frac{\omega_2}{\omega_1}\boldsymbol{E}_2^* \times (\nabla \times \boldsymbol{E}_1)\right)\Bigg]. \end{aligned} \tag{2.11}$$

It has been shown [125] that apart from the nonlinear electric dipole moment, there are two other moments of the second order induced in the system which can significantly contribute to the macroscopic nonlinear polarization: the electric quadrupole moment and the magnetic dipole moment. The quadratic electric quadrupole moment is given by $\boldsymbol{Q}_-^{(2)} = -\mathrm{e}\boldsymbol{x}_1^{(1)}\boldsymbol{x}_2^{(1)*} - \mathrm{e}\boldsymbol{x}_2^{(1)*}\boldsymbol{x}_1^{(1)}$. Notice that for convenience our definition differs from the usual one, which is made *traceless* by subtracting the trace of the tensor and includes a numerical prefactor of 3. Substituting the linear solution, we obtain

$$\boldsymbol{Q}_-^{(2)} = -\frac{1}{e}\alpha_1\alpha_2^*(\boldsymbol{E}_1\boldsymbol{E}_2^* + \boldsymbol{E}_2^*\boldsymbol{E}_1). \tag{2.12}$$

The quadratic magnetic dipole is given by

$$\boldsymbol{\mu}_-^{(2)} = (-e/2mc)\{\boldsymbol{x}_1^{(1)} \times m\dot{\boldsymbol{x}}_2^{(1)*} + \boldsymbol{x}_2^{(1)*} \times m\dot{\boldsymbol{x}}_1^{(1)}\}, \tag{2.13}$$

which becomes

$$\boldsymbol{\mu}_-^{(2)} = -\frac{i}{2ce}\alpha_1\alpha_2^*\,(\omega_1 + \omega_2)\,(\boldsymbol{E}_1 \times \boldsymbol{E}_2^*), \tag{2.14}$$

after the substitution of the linear solution. Taking into consideration the contribution of these three second order moments, the position dependent macroscopic nonlinear polarization induced in the system can be defined in the following way,

$$\boldsymbol{P}_-(z) = n(z)\boldsymbol{p}_-^{(2)} - \frac{1}{2}\nabla \cdot n(z)\boldsymbol{Q}_-^{(2)} + \frac{ic}{\omega_-}\nabla \times n(z)\boldsymbol{\mu}_-^{(2)}, \tag{2.15}$$

Note that the above expression has an additional term related to the quadratic magnetic moment.

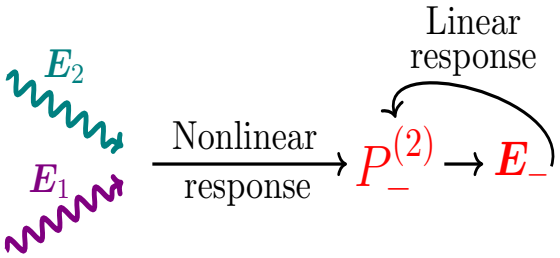

Figure 2.2: A schematic diagram to illustrate the two incident fields oscillating at frequency ω_1 and ω_2, the DF polarization (ω_-) induced by the nonlinear response, the resulting DF field oscillating at ω_- and its linear response to the DF field.

This relation would yield the same induced current and is more convenient than keeping only the first two terms in Eq. (2.15) but adding a nonlinear magnetization in the system. In Eq. (2.15), $n(z)$ is the number density of the polarizable entities which make up the semi-infinite system, with its value changing rapidly albeit continuously across the surface (located at $z = 0$), from its bulk asymptotic value $n(z \to \infty) = n_B$ to the value $n(z \to -\infty) = 0$ in the vacuum [Fig. 2.1 (c)]. As we have assumed all entities to be identical to each other, effects such as those arising from the surface electronic structure or any other microscopic crystalline effects do not contribute to the nonlinear response of the system within our model. We must remark that in a real system these additional effects may not be negligible. However, we will only focus on the effect of the spatial variation of the field on the second order response. The nonlinear polarization induced in the system results in nonlinear sources oscillating at the difference frequency generating an oscillating DF field. The linear response of the system to this DF field must be taken into consideration to obtain appropriately screened self-consistent nonlinear polarization and fields. This response is illustrated schematically in Fig. 2.2. Taking it into consideration and substituting Eqs. (2.11), (2.12) and (2.14) into Eq. (2.15), we get

$$\begin{aligned}\boldsymbol{P}_-(z) =& n(z)\alpha_-\boldsymbol{E}_- - \frac{n(z)}{e}\alpha_-\Bigg[\alpha_1\left(\boldsymbol{E}_1\cdot\nabla\boldsymbol{E}_2^* + \frac{\omega_1}{\omega_2}\boldsymbol{E}_1\times(\nabla\times\boldsymbol{E}_2^*)\right)\\ &+\alpha_2^*\left(\boldsymbol{E}_2^*\cdot\nabla\boldsymbol{E}_1 + \frac{\omega_2}{\omega_1}\boldsymbol{E}_2^*\times(\nabla\times\boldsymbol{E}_1)\right)\Bigg]\\ &+\frac{1}{2e}\alpha_1\alpha_2^*\nabla\cdot n(z)(\boldsymbol{E}_1\boldsymbol{E}_2^* + \boldsymbol{E}_2^*\boldsymbol{E}_1)\\ &+\frac{1}{2e}\alpha_1\alpha_2^*\left(\frac{\omega_1+\omega_2}{\omega_-}\right)\nabla\times n(z)(\boldsymbol{E}_1\times\boldsymbol{E}_2^*).\end{aligned} \tag{2.16}$$

In order to find the surface response of the medium, we will only be interested in the thin *selvedge* region whose thickness is much smaller than the wavelength and thus the effects of retardation can be safely ignored. To this end, we drop the $\nabla\times\boldsymbol{E}$ terms and ignore the slow spatial variations of

the field along the surface. Although the $\nabla \times \boldsymbol{E}$ terms are negligible, the *curl* of the cross products may not be insignificant and hence have not been left out.

As the $\hat{\boldsymbol{z}}$ axis is normal to the surface [see Fig. 2.1(a)], the normal component of the macroscopic polarization is

$$\begin{aligned} P_{-,z}(z) =& n(z)\alpha_- E_{-,z} - \frac{n(z)}{e}\alpha_- \left(\alpha_1 E_{1z}\frac{\partial}{\partial z}E^*_{2z} + \alpha_2^* E^*_{2z}\frac{\partial}{\partial z}E_{1z}\right) \\ &+ \frac{1}{2e}\alpha_1\alpha_2^*\frac{\partial}{\partial z}n(z)(E_{1z}E^*_{2z} + E^*_{2z}E_{1z}). \end{aligned} \tag{2.17}$$

Since we concentrate our attention in the long-wavelength regime, the fields at the selvedge are essentially longitudinal. In the medium, we have $\nabla \cdot \boldsymbol{E} = 4\pi\rho^{\text{tot}} = -4\pi\nabla \cdot \boldsymbol{P}$. At the surface, both $\boldsymbol{E}$ and $\boldsymbol{P}$ have rapid variations in the z direction. Thus $\nabla \cdot \boldsymbol{E} = \partial E_z/\partial z$ and $\nabla \cdot \boldsymbol{P} = \partial P_z/\partial z$ which after integration yields $E_z = -4\pi P_z$. There is a small correction term present which integrates to zero across the selvedge in the limit of zero width. Substituting this for the electric field at ω_- in the previous equation and combining the term with L.H.S., we get,

$$\begin{aligned} P_{-,z}(z)\{1 + 4\pi n(z)\alpha_-\} =& -\frac{n(z)}{e}\alpha_- \left(\alpha_1 E_{1z}\frac{\partial}{\partial z}E^*_{2z} + \alpha_2^* E^*_{2z}\frac{\partial}{\partial z}E_{1z}\right) \\ &+ \frac{1}{2e}\alpha_1\alpha_2^*\frac{\partial}{\partial z}n(z)(E_{1z}E^*_{2z} + E^*_{2z}E_{1z}). \end{aligned} \tag{2.18}$$

Using the relation $E_{jz} = D_{jz}/\epsilon_g(z)$ for the linear fields with

$$\epsilon_g(z) = 1 + 4\pi n(z)\alpha_g, \tag{2.19}$$

for $g = 1, 2$, ω_- or ω_+ as the case may be in Eq. (2.18), we write the normal component of the DF polarization as,

$$\begin{aligned} P_{-,z}(z) =& \frac{1}{e\epsilon_-(z)}\Bigg[- n(z)\alpha_- \left(\alpha_1 \frac{1}{\epsilon_1(z)}\frac{\partial}{\partial z}\frac{1}{\epsilon_2^*(z)} + \alpha_2^* \frac{1}{\epsilon_2^*(z)}\frac{\partial}{\partial z}\frac{1}{\epsilon_1(z)}\right) \\ &+ \alpha_1\alpha_2^*\frac{\partial}{\partial z}n(z)\frac{1}{\epsilon_1(z)}\frac{1}{\epsilon_2^*(z)}\Bigg] D_{1z}D^*_{2z} + 1 \leftrightarrow 2. \end{aligned} \tag{2.20}$$

Note that in Eq. (2.20), we have used the long wavelength approximation (LWA) to assume that the linear displacement fields D_{gz} for $(g = 1, 2)$ are constant across the selvedge. Here, we have also ignored the effects of spatial dispersion and surface induced corrections to the local field. Thus, the resulting normal component of the DF polarization will depend on z through the density profile $n(z)$ and its spatial derivatives.

The DF polarization calculated above [Eq. (2.20)] thus exists only in the thin selvedge region at the surface where the linear response has a large gradient and vanishes in the bulk and in vacuum.

Hence, we can define the surface polarization as,

$$\boldsymbol{P}_{-}^{s} = \int_{-\infty}^{\infty} dz\, \boldsymbol{P}_{-}(z). \tag{2.21}$$

The components of DF quadratic surface susceptibility tensor may be defined as,

$$P_{-,i}^{s} = \sum_{jk} \left[\chi_{ijk}^{s}(\omega_1, \overline{\omega}_2) + \chi_{ikj}^{s}(\overline{\omega}_2, \omega_1)\right] F_{1j} F_{2k}^{*}, \tag{2.22}$$

where the indices i, j, and k represent the different Cartesian directions and the symbol $\overline{\omega}_2$ is used to denote the negative frequency $-\omega_2$. $\boldsymbol{F}$ in Eq. (2.22) is a field whose components are the components of $\boldsymbol{D}$ or $\boldsymbol{E}$ that are continuous across the surface, to avoid the ambiguity about the position in the selvedge where the fields are to be calculated. Note that j and k are dummy indices and thus can be interchanged. Also, the nonlinear susceptibility possesses an intrinsic permutation symmetry which makes, $\chi_{ijk}^{s}(\omega_1, \overline{\omega}_2) = \chi_{ikj}^{s}(\overline{\omega}_2, \omega_1)$. We must point out that the product of fields in Eq. (2.22) is symmetric and the summation implies a full contraction with the $\boldsymbol{\chi}$ tensor which in turn requires the susceptibility tensor to be symmetric under permutation of indices j, k when the frequencies are interchanged simultaneously.

We now integrate Eq. (2.20) by substituting it in Eq. (2.21). The integral to be evaluated is of the form $\int dz f(n(z)) dg(n(z))/dz$, where f and g are rational functions of $n(z)$. The integration can be divided into different intervals where n varies monotonically, which allows us to change integration variable $z \to n$. As the integrands are rational functions of n, they may be integrated analytically for any density profile $n(z)$ to obtain the normal component of the nonlinear surface polarization $P_{-,z}^{s}$,

$$P_{-,z}^{s} = \chi_{zzz}^{s}(\omega_1, \overline{\omega}_2) D_{1z} D_{2z}^{*} + 1 \leftrightarrow 2, \tag{2.23}$$

where the χ_{zzz}^{s} component of the nonlinear susceptibility is given by

$$\chi_{-,zzz}^{s} = -\frac{a(\omega_1, \overline{\omega}_2)}{64\pi^2 n_B e} \left(\frac{\epsilon_1 - 1}{\epsilon_1}\right) \left(\frac{\epsilon_2^{*} - 1}{\epsilon_2^{*}}\right), \tag{2.24}$$

where $a(\omega_1, \overline{\omega}_2)$ is a dimensionless function to parameterize the normal component of the nonlinear surface polarization [128], given in this case by

$$a(\omega_1, \overline{\omega}_2) = -2\left[1 + \frac{\left(1 - \epsilon_{-}\right) \epsilon_1 \epsilon_2^{*} \left(\epsilon_2^{*} \log(\epsilon_{-}/\epsilon_1) + \text{c.p.}\right)}{\left(\epsilon_1 - \epsilon_2^{*}\right) \left(\epsilon_2^{*} - \epsilon_{-}\right) \left(\epsilon_{-} - \epsilon_1\right)}\right], \tag{2.25}$$

where c.p. denotes cyclic permutation of the indices $1, 2$, and $-$.

In Fig. 2.3 we illustrate the behavior of the real and imaginary parts of $a(\omega_1, \overline{\omega_2})$. To that end, we consider a dispersive harmonic solid whose dielectric function has a single Lorentzian resonance

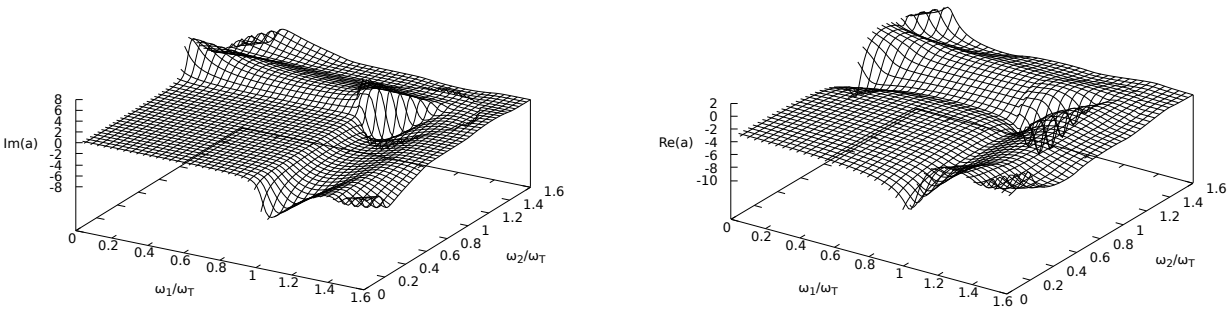

Figure 2.3: Imaginary (left panel) and real (right panel) part of the function $a(\omega_1, \overline{\omega}_2)$ for a harmonic solid as function of ω_g/ω_T for $g = 1, 2$. The relation between the longitudinal and transverse optical mode frequencies is $\omega_{\rm L} = \sqrt{2}\,\omega_{\rm T}$. The lifetime parameter $\tau = 20/\omega_{\rm T}$.

given by [141]

$$\epsilon_{\rm d}(\omega) = \frac{\omega_{\rm L}^2 - \omega^2 - i\omega/\tau}{\omega_{\rm T}^2 - \omega^2 - i\omega/\tau} \tag{2.26}$$

where $\omega_{\rm L}$ and $\omega_{\rm T}$ are the frequencies of the longitudinal and transverse optical modes respectively and we included a small dissipation characterized by τ. We choose $\omega_{\rm L} = \sqrt{2}\omega_{\rm T}$ and $\tau = 20/\omega_{\rm T}$. The dielectric function has a pole at $\omega_{\rm T}$ and crosses zero at $\omega_{\rm L}$. Between these two values, it is negative and the logarithm in Eq. (2.25) becomes large. Hence, we expect the real and imaginary part of a to exhibit some spectral feature in this region. Fig. 2.3 demonstrates peaks and valleys, for both the real and imaginary part of a, whenever either of the input frequency falls in this region. A broad valley along the diagonal is observed in the region where both the input frequencies lie between $\omega_{\rm T}$ and $\omega_{\rm L}$ with the difference frequency close to zero. The parameter a reaches its asymptotic value equal to -2 in the low frequency limit, illustrated by the real part of a in the right panel of the figure.

We follow a similar procedure to that shown above for the parallel component of the nonlinear polarization. Using Eq. (2.16), we find an expression analogous to Eq. (2.20) for the parallel component,

$$\begin{aligned}\boldsymbol{P}_{-,\parallel}(z) = \frac{1}{2e}\alpha_1\alpha_2^*\Bigg[&\boldsymbol{E}_{1\parallel}\frac{\partial}{\partial z}\frac{n(z)}{\epsilon_2^*(z)}D_{2z}^* + \boldsymbol{E}_{2\parallel}^*\frac{\partial}{\partial z}\frac{n(z)}{\epsilon_1(z)}D_{1z} \\ &+ \left(\frac{\omega_1+\omega_2}{\omega_-}\right)\left(\frac{\partial}{\partial z}\frac{n(z)}{\epsilon_2^*(z)}D_{2z}^*\boldsymbol{E}_{1\parallel} - \frac{\partial}{\partial z}\frac{n(z)}{\epsilon_1(z)}D_{1z}\boldsymbol{E}_{2\parallel}^*\right)\Bigg].\end{aligned} \tag{2.27}$$

The above equation can be simply integrated across the selvedge, yielding the nonlinear tangential

surface polarization

$$\begin{aligned}\boldsymbol{P}^s_{-,\parallel} &= \int_{-\infty}^{\infty} dz \boldsymbol{P}_{-,\parallel}(z) \\ &= \frac{1}{2e}\alpha_1\alpha_2^*\left[\frac{n_B}{\epsilon_2^*}\left(1+\frac{\omega_1+\omega_2}{\omega_-}\right)\boldsymbol{E}_{1\parallel}D^*_{2z} + \frac{n_B}{\epsilon_1}\left(1-\frac{\omega_1+\omega_2}{\omega_-}\right)D_{1z}\boldsymbol{E}^*_{2\parallel}\right] \\ &= \chi^s_{-,\parallel\parallel z}(\omega_1,\overline{\omega}_2)\boldsymbol{E}_{1\parallel}D^*_{2z} + \chi^s_{-,\parallel z\parallel}(\omega_1,\overline{\omega}_2)D_{1z}\boldsymbol{E}^*_{2\parallel} + 1 \leftrightarrow 2, \end{aligned} \tag{2.28}$$

where the surface susceptibility is parameterized as

$$\chi^s_{-,\parallel\parallel z}(\omega_1,\overline{\omega}_2) = \chi^s_{-,\parallel z\parallel}(\overline{\omega}_2,\omega_1) = -\frac{1}{32\pi^2 n_B e}\frac{(\epsilon_1-1)(\epsilon_2^*-1)}{\epsilon_2^*}\frac{\omega_1}{\omega_-}b(\omega_1,\overline{\omega}_2), \tag{2.29}$$

$$\chi^s_{-,\parallel\parallel z}(\overline{\omega}_2,\omega_1) = \chi^s_{-,\parallel z\parallel}(\omega_1,\overline{\omega}_2) = \frac{1}{32\pi^2 n_B e}\frac{(\epsilon_1-1)(\epsilon_2^*-1)}{\epsilon_1}\frac{\omega_2}{\omega_-}b(\overline{\omega}_2,\omega_1), \tag{2.30}$$

with

$$b(\omega_1,\overline{\omega}_2) = b(\overline{\omega}_2,\omega_1) = -1. \tag{2.31}$$

There is another component of the surface susceptibility tensor, $\chi^s_{z\parallel\parallel}$ allowed by the in-plane isotropy at the surface, but it is null within this model. By definition, our results are primarily applicable to dielectric materials, however it has been shown that the results are equivalent to those of the local jellium model [125] for metals.

We now focus on the bulk nonlinear response of the system. The quadratic polarization induced within the bulk is evaluated by substituting Eqs. (2.11), (2.12) and (2.14) in Eq. (2.15) and assuming that the fundamental fields propagate as plane waves $\boldsymbol{E}_g(\boldsymbol{r}) = \boldsymbol{E}_g e^{i\boldsymbol{q}_g\cdot\boldsymbol{r}}$ with the bulk wave vectors given by $\boldsymbol{q}_g = \{\boldsymbol{q}_{j\parallel}, q_{jz}\}$ for $(g = 1, 2)$. We get

$$\boldsymbol{P}^B_-(\boldsymbol{r}) = ie^{i(\boldsymbol{q}_1+\boldsymbol{q}_2)\cdot\boldsymbol{r}}[D_1\boldsymbol{q_1}(\boldsymbol{E}_1\cdot\boldsymbol{E}_2^*) + \overline{D}_1(\boldsymbol{q}_1\cdot\boldsymbol{E}_2^*)\boldsymbol{E}_1 + D_2^*\,\boldsymbol{q}_2^*(\boldsymbol{E}_2^*\cdot\boldsymbol{E}_2) + \overline{D}_2^*(\boldsymbol{q}_2^*\cdot\boldsymbol{E}_1)\boldsymbol{E}_2^*], \tag{2.32}$$

where the number density of the polarizable entities is equal to the constant value n_B in the bulk. The wave vectors projection onto the surface $\boldsymbol{q}_{j\parallel}$ are determined by Snell's law, $q_{j\parallel} = (\omega_g/c)\sin\theta_g$, where θ_g is the angle of incidence of the beam, and q_{iz} is obtained from the bulk dispersion relation, $q_{iz}^2 = (\omega_g/c)^2\epsilon_g - q_{j\parallel}^2$ for both incident beams, i.e., $g = 1, 2$. The bulk nonlinear polarization in Eq. (2.32) is characterized by the parameters D_g and $\overline{D}_g$ given by

$$D_g = \frac{1}{16\pi^2 n_B e}(\epsilon_2^*-1)(\epsilon_1-1)\delta_g d_g, \tag{2.33}$$

$$\overline{D}_g = \frac{1}{16\pi^2 n_B e}(\epsilon_2^*-1)(\epsilon_1-1)\overline{\delta}_g \overline{d}_g, \tag{2.34}$$

for $g = 1, 2$ and with the bulk parameter, δ as

$$\delta_1 = -\left(\frac{\epsilon_- - 1}{\epsilon_1 - 1}\right)\frac{\omega_2}{\omega_1}, \tag{2.35}$$

$$\overline{\delta}_1 = \frac{\omega_1}{\omega_-} - \left(\frac{\epsilon_- - 1}{\epsilon_1 - 1}\right)\frac{\omega_-}{\omega_1}, \tag{2.36}$$

$$\delta_2 = -\left(\frac{\epsilon_- - 1}{\epsilon_2^* - 1}\right)\frac{\omega_1}{\omega_2}, \tag{2.37}$$

$$\overline{\delta}_2 = -\frac{\omega_2}{\omega_-} + \left(\frac{\epsilon_- - 1}{\epsilon_2^* - 1}\right)\frac{\omega_-}{\omega_2}, \tag{2.38}$$

and $d_1 = d_2 = \overline{d}_1 = \overline{d}_2 = 1$. Note that P_-^B plays the role of an external source for the DF field in the bulk. The total bulk polarization contains also an additional polarization linearly induced in response to the self-consistent DF field, as shown in Eq. (2.16). To obtain the self-consistent DF field Maxwell's equations with sources should be solved with appropriate boundary conditions.

2.3 Dipolium model : SF and SH response

The sum frequency (SF) response for the semi-infinite homogeneous system described by the *dipolium* model (introduced in Sec. 2.2) has been reported in [125] by Maytorena et al. The SF response can be easily obtained by changing the sign of ω_2 in the expressions for the DF response evaluated in the previous section and using the relation $\epsilon(-\omega_2) = \epsilon^*(\omega_2)$. In the next sub-section, explicit expressions for SF macroscopic polarization, the different components of the surface polarization and susceptibility tensors are provided. They are identical to the results of ref. [125]. Afterwards, we will consider the degenerate second harmonic (SH) response by choosing the same frequency for both input fields, $\omega_1 = \omega_2$ and write down the explicit analytical formulas for the nonlinear response functions. The results for SH are important for this work, as they are employed to calculate the response of the bidimensional system in Chapter 3.

Dipolium model : SF response

The quadratic SF moments, macroscopic SF polarization and susceptibility induced in the system can be obtained from the expressions of the DF case by changing the sign of the frequency $\omega_2 \to -\omega_2$ and using $\epsilon(-\omega_2) = \epsilon(\omega_2)^*$. We also use the SF, $\omega_+ = \omega_1 + \omega_2$, in the expressions instead of the DF, $\omega_- = \omega_1 - \omega_2$.

The quadratic SF dipole moment induced within the bulk of the media, can be written directly

from Eq. (2.11) by making the change of frequency. We get,

$$\boldsymbol{p}_{+}^{(2)} = -\frac{1}{e}\alpha_{+}\Bigg[\alpha_1\left(\boldsymbol{E}_1\cdot\nabla\boldsymbol{E}_2 - \frac{\omega_1}{\omega_2}\boldsymbol{E}_1\times(\nabla\times\boldsymbol{E}_2)\right) + \alpha_2\left(\boldsymbol{E}_2\cdot\nabla\boldsymbol{E}_1 - \frac{\omega_2}{\omega_1}\boldsymbol{E}_2\times(\nabla\times\boldsymbol{E}_1)\right)\Bigg]. \tag{2.39}$$

The quadratic DF electric quadrupole moment given by Eq. (2.12), for the SF case becomes,

$$\boldsymbol{Q}_{+}^{(2)} = -\frac{1}{e}\alpha_1\alpha_2(\boldsymbol{E}_1\boldsymbol{E}_2 + \boldsymbol{E}_2\boldsymbol{E}_1), \tag{2.40}$$

and the quadratic magnetic dipole, of Eq. (2.14),

$$\boldsymbol{\mu}_{+}^{(2)} = -\frac{i}{2ce}\alpha_1\alpha_2\left(\omega_1-\omega_2\right)(\boldsymbol{E}_1\times\boldsymbol{E}_2). \tag{2.41}$$

The macroscopic SF polarization can be obtained by substituting these second order moments into Eq. (2.15) and using the same arguments as those to obtain the DF macroscopic polarization given by Eq. (2.16). We get,

$$\begin{aligned}\boldsymbol{P}_{+}(z) =& n(z)\alpha_{+}\boldsymbol{E}_{+} - \frac{n(z)}{e}\alpha_{+}\Bigg[\alpha_1\left(\boldsymbol{E}_1\cdot\nabla\boldsymbol{E}_2 - \frac{\omega_1}{\omega_2}\boldsymbol{E}_1\times(\nabla\times\boldsymbol{E}_2)\right)\\ &+\alpha_2\left(\boldsymbol{E}_2\cdot\nabla\boldsymbol{E}_1 - \frac{\omega_2}{\omega_1}\boldsymbol{E}_2\times(\nabla\times\boldsymbol{E}_1)\right)\Bigg]\\ &+\frac{1}{2e}\alpha_1\alpha_2\nabla\cdot n(z)(\boldsymbol{E}_1\boldsymbol{E}_2+\boldsymbol{E}_2\boldsymbol{E}_1)\\ &+\frac{1}{2e}\alpha_1\alpha_2\left(\frac{\omega_1-\omega_2}{\omega_{+}}\right)\nabla\times n(z)(\boldsymbol{E}_1\times\boldsymbol{E}_2).\end{aligned} \tag{2.42}$$

Following the same procedure as illustrated by Eqs. (2.17) to (2.21), an equation analogous to Eq. (2.23) for the normal component of the SF surface polarization can be evaluated. It is given by

$$P_{+,z}^{s} = \chi_{+,zzz}^{s}(\omega_1,\omega_2)D_{1z}D_{2z} + 1 \leftrightarrow 2, \tag{2.43}$$

where $\chi_{+,zzz}^{s}(\omega_1,\omega_2)$ is the normal component of the SF susceptibility. Similar to Eq. (2.24), the SF surface susceptibility can be written in terms of the dimensionless parameter $a(\omega_1,\omega_2)$ [128] as

$$\chi_{+,zzz}^{s} = -\frac{a(\omega_1,\omega_2)}{64\pi^2 n_B e}\left(\frac{\epsilon_1-1}{\epsilon_1}\right)\left(\frac{\epsilon_2-1}{\epsilon_2}\right), \tag{2.44}$$

where

$$a(\omega_1,\omega_2) = -2\left[1+\frac{\left(1-\epsilon_{+}\right)\epsilon_1\epsilon_2\left(\epsilon_2\log(\epsilon_{+}/\epsilon_1)+\text{c.p.}\right)}{\left(\epsilon_1-\epsilon_2\right)\left(\epsilon_2-\epsilon_{+}\right)\left(\epsilon_{+}-\epsilon_1\right)}\right], \tag{2.45}$$

where c.p. denotes cyclic permutation of the indices $1, 2$, and ω_{+}.

The tangential component of the SF surface nonlinear polarization (analogous to Eq. (2.28)) will then be given by

$$\boldsymbol{P}^s_{+,\parallel} = \chi^s_{+,\parallel\parallel z}(\omega_1,\omega_2)\boldsymbol{E}_{1\parallel}D_{2z} + \chi^s_{+,\parallel z\parallel}(\omega_1,\omega_2)D_{1z}\boldsymbol{E}_{2\parallel} + 1 \leftrightarrow 2, \tag{2.46}$$

where the surface susceptibility can be parameterized as

$$\chi^s_{+,\parallel\parallel z}(\omega_1,\omega_2) = \chi^s_{+,\parallel z\parallel}(\omega_2,\omega_1) = -\frac{1}{32\pi^2 n_B e}\frac{(\epsilon_1-1)(\epsilon_2-1)}{\epsilon_2}\frac{\omega_1}{\omega_+}b(\omega_1,\omega_2), \tag{2.47}$$

$$\chi^s_{+,\parallel\parallel z}(\omega_2,\omega_1) = \chi^s_{+,\parallel z\parallel}(\omega_1,\omega_2) = -\frac{1}{32\pi^2 n_B e}\frac{(\epsilon_1-1)(\epsilon_2-1)}{\epsilon_1}\frac{\omega_2}{\omega_+}b(\omega_2,\omega_1), \tag{2.48}$$

with

$$b(\omega_1,\omega_2) = b(\omega_2,\omega_1) = -1. \tag{2.49}$$

The $\chi_{+,z\parallel\parallel}$ component of the surface SF susceptibility tensor is found to be equal to zero in this model. Other components are null due to the isotropy of the surface.

Dipolium model : SH response

The second harmonic (SH) response is simply the degenerate case of the SF response with $\omega_1 = \omega_2 = \omega$ where two incoming photons with equal energies interact to produce an outgoing photon with double the energy ($\omega_{\rm sh} = 2\omega$). To study the SH response, we choose a monochromatic external field oscillating with frequency ω incident on the material producing a SH field at $\omega_{\rm sh} = 2\omega$. Hence substituting this limit in the expressions of the previous section, the SH response of the semi-infinite system can be obtained.

Substituting the condition of the equality of frequency and choosing only one incident field in Eqs. (2.39) and (2.40), the microscopic SH dipole moment induced is obtained to

$$\boldsymbol{p}^{(2)}_{\rm sh} = -\frac{1}{2e}\alpha_\omega\alpha_{\rm sh}[\nabla E^2_\omega - 4\boldsymbol{E}_\omega \times (\nabla \times \boldsymbol{E}_\omega)], \tag{2.50}$$

and the quadrupole moment as

$$\boldsymbol{q}^{(2)}_{\rm sh} = -\frac{1}{e}\alpha^2_\omega \boldsymbol{E}_\omega \boldsymbol{E}_\omega. \tag{2.51}$$

Notice that imposing this limit to Eq. (2.41), the nonlinear magnetic dipole in the system, gives zero and does not contribute to the SH polarization. The subscript sh denotes quantities at the SH frequency and ω at the fundamental frequency.

Substituting Eqs. (2.50) and (2.51) in Eq. (2.15) for the SH case, we obtain for the macroscopic SH

polarization,

$$\begin{aligned}\boldsymbol{P}_{\rm sh}(z) =& n(z)\alpha_{\rm sh}\boldsymbol{E}_{\rm sh} - \frac{n(z)}{2e}\alpha_\omega\,\alpha_{\rm sh}[\nabla \boldsymbol{E}_\omega^2 - 4\boldsymbol{E}_\omega \times (\nabla \times \boldsymbol{E}_\omega)] \\ &+ \frac{1}{2e}\alpha_\omega^2\,\nabla\cdot(n(z)\boldsymbol{E}_\omega\boldsymbol{E}_\omega).\end{aligned} \tag{2.52}$$

Using a procedure identical to the one discussed above for DF or SF case, the components of the SH surface polarization can be obtained from Eq. (2.52). Eq. (2.43) for the normal component of the surface SF polarization in the limit of a single incident field with frequency ω for the SH case is thus reduced to

$$P^s_{{\rm sh},z} = \chi^s_{{\rm sh},zzz}(\omega)\,D^2_\omega, \tag{2.53}$$

where the normal component of the SH susceptibility $\chi^s_{{\rm sh},zzz}(\omega)$ will be given by

$$\chi^s_{{\rm sh},zzz}(\omega) = -\frac{a(\omega)}{64\pi^2 n_B e}\left(\frac{\epsilon_\omega - 1}{\epsilon_\omega}\right)^2, \tag{2.54}$$

where

$$a(\omega) = 2\frac{\left(\epsilon_{\rm sh} - \epsilon_\omega\right)\left(2\epsilon_\omega - \epsilon_{\rm sh} - \epsilon_\omega\epsilon_{\rm sh}\right) + \epsilon_\omega^2\left(1 - \epsilon_{\rm sh}\right)\,\log\left(\epsilon_\omega/\epsilon_{\rm sh}\right)}{\left(\epsilon_{\rm sh} - \epsilon_\omega\right)^2}, \tag{2.55}$$

Eqs. (2.54) and (2.55) can be directly written down from Eqs. (2.44) and (2.45) by using the condition of equality of the frequency of the input frequencies.

The tangential component of the SH surface nonlinear polarization can be similarly obtained from Eq. (2.46). We get,

$$\boldsymbol{P}^s_{{\rm sh},\parallel} = \chi^s_{\parallel\parallel z}(\omega)\boldsymbol{E}_{\omega,\parallel}D_{\omega,z}, \tag{2.56}$$

with the tangential component of the surface SH susceptibility given by

$$\chi^s_{\parallel\parallel z}(\omega) = \chi^s_{\parallel z\parallel}(\omega) = -\frac{1}{32\pi^2 n_B e}\frac{(\epsilon_\omega - 1)^2}{\epsilon_\omega}\,b(\omega), \tag{2.57}$$

where

$$b(\omega) = -1. \tag{2.58}$$

Eqs. (2.57) and (2.58) can also be directly obtained from Eqs. (2.47) and (2.49) by employing the condition of equality of the incident frequencies.

Similar to the DF and SF case, the other component of the surface SH susceptibility tensor $\chi_{{\rm sh},z\parallel\parallel}$, although permitted by the isotropy of the surface, is zero within this model.

2.4 Jellium : The Hydrodynamic Model

The *jellium* or hydrodynamic model, applicable to metallic systems, represents a conductor as a semi-infinite electron gas with an equilibrium density interpolating smoothly between vacuum and an asymptotic bulk value. The Euler's hydrodynamic equation of motion describing the motion of the charged fluid, ignoring the pressure term is given by,

$$mn\left(\frac{\partial}{\partial t}+\frac{1}{\tau}\right)\boldsymbol{u}+mn(\boldsymbol{u}\cdot\nabla)\boldsymbol{u}=-en\boldsymbol{E}-\frac{e}{c}n\boldsymbol{u}\times\boldsymbol{B}, \tag{2.59}$$

where m, $-e$, and $n(\boldsymbol{r},t)$ are the mass, the charge and the density at point $\boldsymbol{r}$ and time t of the electron, respectively, $\boldsymbol{u}(\boldsymbol{r},t)$ is the velocity field, and $\boldsymbol{E}(\boldsymbol{r},t)$ and $\boldsymbol{B}(\boldsymbol{r},t)$ are the electric and magnetic fields respectively. The term proportional to ∇p with pressure p, which we didn't include in the equation above, adds a *nonlocal* correction to the polarization which may affect the linear response of the system and nonlinear response, especially at the surface [142], but this surface correction would depend on the detailed shape of surface density profile and is thus beyond the scope of this work. Here, the nonlinearity of the system arises due to the presence of the convective time derivative $\boldsymbol{u}\cdot\nabla\boldsymbol{u}$ and the magnetic Lorentz force term evident from Eq. (2.59). The aforementioned equation can be solved by considering two incident electromagnetic fields oscillating at frequencies ω_1 and ω_2 and writing down the time varying quantities as a superposition of different monochromatic waves with frequencies ω_1, ω_2, $2\omega_1$, $2\omega_2$, $\omega_1\pm\omega_2$, and $0=(\omega_1-\omega_1$ or, $\omega_2-\omega_2)$

$$\begin{aligned} h(\boldsymbol{r},t) \;=\; & h_0(\boldsymbol{r})+[h(\boldsymbol{r},\omega_1)e^{-i\omega_1 t}+h(\boldsymbol{r},\omega_2)e^{-i\omega_2 t}+h(\boldsymbol{r},2\omega_1)e^{-i2\omega_1 t}+h(\boldsymbol{r},2\omega_2)e^{-i2\omega_2 t} \\ & +h(\boldsymbol{r},\omega_1-\omega_2)e^{-i(\omega_2-\omega_1)t}+\cdots+\text{c.c.}], \end{aligned} \tag{2.60}$$

where h stands for either n, $\boldsymbol{u}$, $\boldsymbol{E}$, or $\boldsymbol{B}$. The nonlinear current induced in the system can be obtained from the solution of Eq. (2.59). Using the nonlinear current, the nonlinear polarization induced in the metal can be calculated and the nonlinear bulk and surface susceptibilities can be extracted from it. Ref. [125] reports explicit expressions for SF response from which the DF response can be obtained by changing $\omega_2\to-\omega_2$ and using the fact that the field amplitudes such as $\boldsymbol{E}(\omega_2)$ and the complex response functions like $\epsilon(\omega_2)$ become their conjugates when the sign of their frequency argument is inverted. The results from both the models are identical. This could be understood by regarding a local metal within the jellium model as a harmonic dipolium for which the restoring force is set equal to zero. For a detailed analysis on the comparison, Ref. [125] can be followed. We mention this model simply to show that the results of the dipolium model may be used to analyze metallic systems.

3

SH response of a nanowire: Analytical Calculation

Second harmonic generation (SHG) from the bulk of centrosymmetric materials, such as metals, is strongly suppressed and is actually null within the electric dipolar approximation. There may be excitation of higher multipoles such as an electric quadrupole or a magnetic dipole within the bulk contributing to SHG. This may prove to be useful for studying electric-dipole forbidden transitions [143, 144]. The dipolar second harmonic (SH) response from centrosymmetric systems is observed only at their surface where the inversion symmetry is locally lost. This selection rule is also applicable to nanoparticles made up of centrosymmetric materials, with a nonlinear dipolar contribution to the SH surface response which is comparable to its volumetric bulk response. However, if the nanoparticle has a symmetrical shape, there is an exact cancellation of the locally induced dipolar surface nonlinear polarization from opposite points of the surface, thus integrating to a null total response. For particles with size comparable to the wavelength of light, quadrupolar or higher multipoles may contribute towards the generation of a SH response owing to the presence of retardation effects [50, 145]. In order to extract a non-zero electric dipolar contribution to the surface SH response of nanoparticles made up of centrosymmetric materials, one of the following conditions must be met to break the symmetry: either an inhomogeneous field across the particle or nonsymmetric shape of the particle. Nanoparticles with symmetrical shapes, such as a sphere, when subjected to an inhomogeneous perturbing field generate a net SH response due to the contribution arising from the *non-local* excitation of dipole moments [51, 54, 55, 146, 147]. The reason behind this non-vanishing dipolar SH response is that the quadratic dipole moment density is induced with unequal magnitudes at different regions of the surface, which when integrated over the surface might yield a non-zero response. Another approach is to make the geometry of the nanoparticles noncentrosymmetric. In this scenario too, the quadratic dipolar SH response induced at different points on the surface when integrated over the entire nanoparticle results in a non-zero nonlinear dipolar response [20, 27, 30–32]. The importance of investigating distinct approaches to achieve highly efficient SHG from centrosymmetric materials, especially metals, is to take advantage of the plasmon resonances for local field enhancement resulting in stronger SH signals and higher efficiency for the conversion process [2]. SHG from nanoparticles, arrays of nanoparticles, and nanostructured

materials with a variety of geometries have been studied extensively under different experimental conditions [24, 27, 28, 148]. Many numerical studies employing various techniques such as finite differences in the time domain (FDTD) [29, 30], the finite element method (FEM) [21], the discrete dipole approximation (DDA) [34], and the surface integral method [31–33] have also been reported.

To the best of our knowledge, there have been no reports of *analytical* calculations to study the SH response of nanostructures made up of centrosymmetric materials with a noncentrosymmetric geometry. Here, we develop a theory that allows the analytical calculation of the nonlinear response corresponding to SHG from a nanowire made up of a centrosymmetric material with small deviations from a symmetrical circular cross-section, placed in vacuum and subjected to a homogeneous external field. We obtain the nonlinear polarization, the nonlinear susceptibility and its spectra, and discuss the results [22]. The geometry is made noncentrosymmetric by introducing a parameter which characterizes the extent of deformation away from a circular cross-section. We restrict ourselves to studying small deformations, as that permits us to employ a perturbative approach in order to analytically solve the field equations for the linear and SH induced fields within and beyond the surface of the nanowire. The resultant induced fields would be in the form of a series in powers of the deformation parameter which we terminate after the linear order term, the corrections due to the higher order terms being negligible for small enough deformations. The nonlinear polarization and charges induced in the system are calculated using the results of the *dipolium* model [124], and they play the role of the external sources for the SH fields. Having obtained the SH fields, we evaluate the quadratic dipolar and quadrupolar hyperpolarizabilities of the wire, thus obtaining analytical expressions for them in terms of the linear response at the fundamental and SH frequency, geometrical parameters of the nanowire, and some dimensionless parameters that characterize the nonlinear response. We analyze the resonant structure of their spectra, and identify the different contributions to it for a nanowire made up of any general metal or a dielectric material. We also study the relations between different components of the response tensor arising from the symmetry of our system. Our calculation, being performed within the long wavelength approximation, yields the near fields only. The calculated SH near fields are then utilized to calculate the electromagnetic fields in the radiation zone, which are further used to obtain and discuss the nature of the $2D$ SH radiation pattern. We also illustrate the ratio of the total SH power emitted as the dipolar and quadrupolar fields.

The structure of this chapter is the following. In Section 3.1, we describe our theory to analytically investigate SHG from a deformed infinite thin cylinder, obtaining expressions for the nonlinear dipolar and quadrupolar hyperpolarizabilities. We discuss the effect of symmetry of our system on the results in Section 3.2 and the SH radiation patterns Section 3.3. In Section 3.4, we illustrate our results for deformed cylinders made up of a Drude metal and a resonant dispersive dielectric, and discuss them in detail. Finally, we present some conclusions in Section 3.5.

3.1 Nonlinear response of the nanowire

The nanowire is modeled by choosing an isolated, infinitely long cylinder placed in vacuum with translational symmetry along its axis which is aligned with the $\hat{\boldsymbol{z}}$ direction. We consider the simplest geometry for its cross-section that lacks inversion symmetry, a slight deformation from a circular shape with three protruding lobes having a threefold symmetry. The transverse cross-section in the $x-y$ plane is defined in polar (r,θ) coordinates by the following condition,

$$r_s(\theta) = r_0(1+\xi\cos 3\theta), \tag{3.1}$$

where r_0 is the radius of a symmetric nominal circular cylinder and ξ is a small deformation parameter (See Fig. 3.1). It must be pointed out that the $\cos 3\theta$ term is used to modify the transverse cross-section as its the simplest term possible to make it noncentrosymmetric. If a $\cos\theta$ term were used instead, the cross-section would still remain circular with its origin shifted by a distance equal to ξ; if instead a $\cos 2\theta$ term were used, then the cross-section would have the form of an ellipse which is centrosymmetric. We would like to emphasize that, besides its translational symmetry along z, our system belongs to the $D_{3\mathrm{h}}$ group possessing a vertical mirror plane $(x-z)$ and a three-fold rotational symmetry around the z axis and a horizontal mirror plane $x-y$. The calculations have been performed in $2D$ owing to the translational symmetry along the axis of the cylinder. Also, the radius r_0 of the nominal circular cylinder to which the deformation is applied is considered to be much smaller than the wavelength of the incident electromagnetic field, which allows us to ignore the effects of retardation. We choose an external field that propagates along the $2D$ plane and thus has no variations along the $\hat{\boldsymbol{z}}$ direction. We remark that in an experimental setup, the nanowire would certainly be of a finite length with our results being applicable only when the length of the nanowire l is much larger than the radius of its cross-section r_0. For a detailed discussion on the effect of finiteness of the nanowire on our results, see Sec. 3.4.

If the polarization of the incident field were along the $\hat{\boldsymbol{z}}$ direction, the $\chi_{\perp\parallel\parallel}$ component of the nonlinear surface susceptibility, Eq. (3.19), would couple the linear fields to the surface nonlinear polarization, but within our model it is zero. The derivatives of the nonretarded field in $x-y$ plane would also be zero producing no bulk contribution. Thus, this case is not interesting as it does would not produce any SH signal. It has been shown that even for larger particles, the SH signal produced by incident fields polarized along z axis is much smaller than those polarized in the plane of the cross-section. Thus, we subject the nanowire to an external electric field $\boldsymbol{E}^{\mathrm{ex}}$ oscillating within the $x-y$ plane. We explore the nonlinear dipolar $\boldsymbol{p}$ and quadrupolar $\boldsymbol{Q}$ moments per unit wire length induced in our system. We neglect the spatial variation of the external field across the narrow particle. Since the cylinder is made of a centrosymmetric material and present under the influence of a homogeneous field, the quadratic dipole moment $\boldsymbol{p}$ does not have a nonlocal contribution arising from the spatial variation of the external field. However, owing to the overall non-centrosymmetry of the geometry of the particle, $\boldsymbol{p}$ is expected to have a local contribution proportional to $\boldsymbol{E}^{\mathrm{ex}}\boldsymbol{E}^{\mathrm{ex}}$,

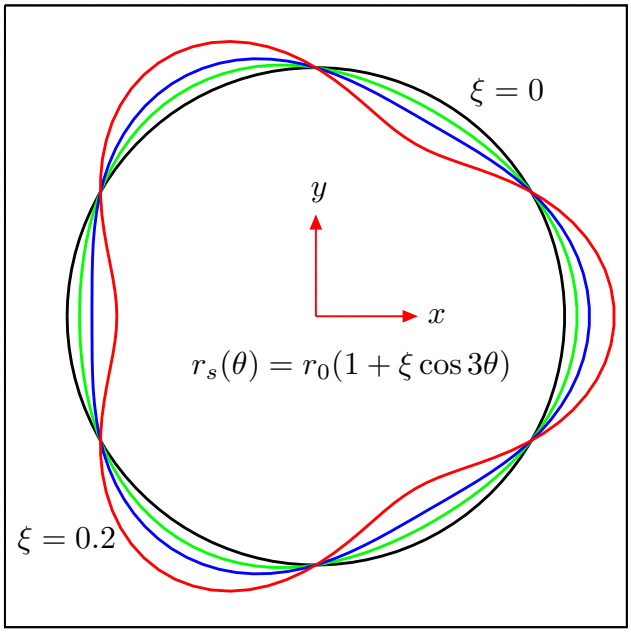

Figure 3.1: Cross-section of a deformed cylinder described by Eq. (3.1) for various values of the deformation parameter $\xi = 0.0 \ldots 0.2$.

whose components p_i we write as

$$p_i = \gamma^d_{ijk} E^{\text{ex}}_j E^{\text{ex}}_k, \tag{3.2}$$

where γ^d_{ijk} is the dipolar hyperpolarizability, a third rank tensor symmetric in the last two indices jk, and we use Einstein summation convention. Similarly, the components of the induced quadratic 2D quadrupole moment, which we define as

$$Q_{ij} = \int d^2r\, \rho(\boldsymbol{r})(2r_i r_j - r^2\delta_{ij}), \tag{3.3}$$

(notice the difference with the usual 3D definition) is given by

$$Q_{ij} = \gamma^Q_{ijkl} E^{\text{ex}}_k E^{\text{ex}}_l, \tag{3.4}$$

where γ^Q_{ijkl} is the quadrupolar hyperpolarizability, a rank four tensor symmetric in the first ij and last kl pairs of indices. Here, $\rho(\boldsymbol{r})$ is the charge density. The above definitions for the response tensors $\boldsymbol{\gamma^d}$ and $\boldsymbol{\gamma^Q}$ are used for any general hyperpolarizability and we will use $(\boldsymbol{\gamma^d_{\text{sh}}}, \boldsymbol{\gamma^Q_{\text{sh}}})$ for the SH response [Chapter 3], $(\boldsymbol{\gamma^d_-}, \boldsymbol{\gamma^Q_-})$ for the difference frequency (DF) response [Chapter 4] and $(\boldsymbol{\gamma^d_+}, \boldsymbol{\gamma^Q_+})$ for the sum frequency (SF) response [Chapter 4] respectively.

For simplicity, we first assume that the external field is a monochromatic wave oscillating at frequency ω_1 and polarized along the $\hat{\boldsymbol{x}}$ direction, $\boldsymbol{E}^{\text{ex}} = E_0\hat{\boldsymbol{x}}$. Given the direction of the external field and the symmetries in the system, inversion ($y \to -y$) and the three-fold rotation (120° in $x - y$ plane) symmetry, the only nonzero component of the nonlinear dipole moment induced in this case

is p_x, which we write as

$$p_x = \gamma^d_{\rm sh} E_0^2, \tag{3.5}$$

and the nonlinear quadrupole moment has only two nonzero components, given by

$$Q_{xx} = -Q_{yy} = \gamma^Q_{\rm sh} E_0^2, \tag{3.6}$$

where the quadratic moments have been written in terms of nonlinear dipolar $\gamma^d_{\rm sh}$ and quadrupolar $\gamma^Q_{\rm sh}$ scalar response functions, related to the full dipolar $\gamma^d_{{\rm sh},ijk}$ and quadrupolar $\gamma^Q_{{\rm sh},ijkl}$ hyperpolarizabilities respectively. The non-zero components of $\boldsymbol{p}$ and $\boldsymbol{Q}$ tensor are directly related to those of $\boldsymbol{\gamma}^d_{\rm sh}$ and $\boldsymbol{\gamma}^Q_{\rm sh}$ respectively. A detailed description about the effect of the symmetries of the system and their implications for the components of the response tensors is provided in Sec. 3.2. In what follows, we will calculate analytical expressions for $\gamma^d_{\rm sh}$ and $\gamma^Q_{\rm sh}$.

In the nonretarded regime, the linear self-consistent near field may be obtained by solving Laplace's equation beyond and within and beyond the particle,

$$\nabla^2 \phi_\omega = 0, \tag{3.7}$$

where the subscript ω corresponds to the fundamental frequency. The following boundary conditions should hold at the interface [150],

$$\phi_\omega(r_S^-) = \phi_\omega(r_S^+) \tag{3.8}$$

$$-\epsilon_\omega \hat{\boldsymbol{n}} \cdot \nabla \phi_\omega(r_S^-) = -\hat{\boldsymbol{n}} \cdot \nabla \phi_\omega(r_S^+). \tag{3.9}$$

where (r_S^-), and (r_S^+) indicate the position just inside and outside the surface of the deformed cylinder respectively, $\hat{\boldsymbol{n}}$ is the unit vector normal to the surface pointing outwards, given by

$$\hat{\boldsymbol{n}} = \hat{\boldsymbol{r}} + 3\xi \sin 3\theta \, \hat{\boldsymbol{\theta}}, \tag{3.10}$$

to first order in ξ, and ϵ_g is the dielectric response of the particle at g-th harmonic frequency, $g = \omega, {\rm sh}$ for the fundamental and the second harmonic respectively. We start with the general solution of Laplace's equation outside

$$\phi^{\rm out}_\omega = \phi^{\rm ex} + \sum_{l=0}^{\infty} r^{-l}(s_l \cos l\theta + t_l \sin l\theta) \tag{3.11a}$$

and within

$$\phi^{\rm in}_\omega = \sum_{l=0}^{\infty} r^{l}(u_l \cos l\theta + v_l \sin l\theta), \tag{3.11b}$$

the particle, where the external scalar potential is given by $\phi^{\rm ex} = -E_0 r \cos\theta$ and we imposed

regularity conditions at the origin and at infinity. We expand the multipolar coefficients ζ_l as a power series on the deformation parameter ξ

$$\zeta_l = \sum_{n=0}^{\infty} \zeta_l^{(n)} \xi^n, \tag{3.12}$$

where the generic coefficients ζ_l stand for any of s_l, t_l, u_l or v_l. As mentioned previously, we restrict ourselves to small deformations, and we consider terms up to linear order in ξ only. Using the trial solution given by Eq. (3.11) and imposing the boundary conditions [Eqs. (3.8) and (3.9)], we obtain the self-consistent linear potential,

$$\frac{\phi_\omega^{\text{out}}}{E_0} = -r\cos\theta - \frac{1-\epsilon_\omega}{1+\epsilon_\omega}\frac{r_0^2}{r}\cos\theta + \xi\left[\left(\frac{1-\epsilon_\omega}{1+\epsilon_\omega}\right)^2 \frac{r_0^3}{r^2}\cos 2\theta - \frac{1-\epsilon_\omega}{1+\epsilon_\omega}\frac{r_0^5}{r^4}\cos 4\theta\right], \tag{3.13a}$$

$$\frac{\phi_\omega^{\text{in}}}{E_0} = -\frac{2}{1+\epsilon_\omega} r\cos\theta + 2\xi\frac{1-\epsilon_\omega}{(1+\epsilon_\omega)^2}\frac{r^2}{r_0}\cos 2\theta, \tag{3.13b}$$

The linear self-consistent electric field $\boldsymbol{E}_\omega$ can then be obtained by evaluating $\boldsymbol{E}_\omega = -\nabla\phi_\omega$. Note that the zeroth order terms are the well known solutions for an infinite circular cylinder [53]. It must be pointed out here that even though the external field is homogeneous, the self-consistent induced field within and beyond the particle is not. The spatial variation of the self-consistent field within the particle induces a nonlinear polarization [150] defined by,

$$\boldsymbol{P}_{\text{sh}}^{(2)} = n\boldsymbol{p}_{\text{sh}}^{(2)} - \frac{1}{2}\nabla\cdot n\,\boldsymbol{q}_{\text{sh}}^{(2)}, \tag{3.14}$$

where we have included the contributions from the nonlinear dipole $\boldsymbol{p}^{\text{nl}}$ and quadrupole $\boldsymbol{q}^{\text{nl}}$ moments of each microscopic polarizable entity within the material, whose number density n is assumed to be constant within the wire. Note that here $\boldsymbol{q}^{\text{nl}}$ is just the second moment tensor of the charge density and may have a finite trace. The dipole and the quadrupole moments induced within the bulk of the nanowire can be calculated by substituting the self consistent linear fields inside the nanowire in Eqs. (2.50) and (2.51) respectively. Note that the terms corresponding to the *curl* of the fields in Eq. (2.50) would be negligible near the nanowire in the long wavelength approximation. Thus, the polarization obtained from Eq. (3.14) due to its spatial variations yields a nonlinear bulk charge density given by

$$\rho_{\text{sh}}^{(2)} = -\nabla\cdot\boldsymbol{P}_{\text{sh}}^{(2)}, \tag{3.15}$$

which evaluates to zero up to linear order in ξ, though it would be nonzero at higher orders.

The termination of this nonlinear bulk polarization at the surface of the particle induces a *bulk-originated* nonlinear surface charge with density $\sigma_{\text{sh}}^b = \boldsymbol{P}_{\text{sh}}^{(2)}(r_s^-)\cdot\hat{\boldsymbol{n}}$. We employ the super-index b to denote the bulk origin of this surface charge. Using Eqs. (2.50), (2.51), (3.13) and (3.14) and the

relation defining $\sigma^b_{\rm sh}$, we get

$$\sigma^b_{\rm sh} = 4\xi \frac{n}{er_0} \frac{(1-\epsilon_\omega)}{(1+\epsilon_\omega)^3} \alpha_\omega (2\alpha_{\rm sh} - \alpha_\omega) \cos\theta E_0^2. \tag{3.16}$$

Beyond the bulk quadratic polarization, the total nonlinear polarization induced in the system contains a contribution from the surface. This response of the system is due to the lack of local inversion symmetry at the thin selvedge region near the surface. We will assume that the thickness of the selvedge region is much smaller than the radius of the cylinder and thus, the surface is considered to be locally flat. We will further assume *local* invariance under rotations around the surface normal. The normal and the tangential components of the nonlinear surface polarization will be given by Eqs. (2.53) and (2.56) respectively with the corresponding susceptibilities given by Eqs. (2.54) and (2.57). Eqs. (2.53) and (2.56) can be combined to obtain, a relation similar to Eq. (2.22), the quadratic SH polarization,

$$P^s_{{\rm sh},i} = \chi^s_{{\rm sh},ijk}(\omega) F_{\omega,j} F_{\omega,k}, \tag{3.17}$$

where the field $\boldsymbol{F}$, as discussed in Sec. 2.2, is defined in terms of quantities that are continuous across the surface to avoid the ambiguity about the position in the selvedge where the fields are to be calculated; $\boldsymbol{F}$ is made up of the normal projection of the displacement field and the parallel projection of the electric field evaluated at the surface $r_s(\theta)$. Thus,

$$\boldsymbol{F}_\omega(r_s) = \boldsymbol{E}_\omega(r_s^+) = \epsilon_\omega \boldsymbol{E}^\perp_\omega(r_s^-) + \boldsymbol{E}^\parallel_\omega(r_s^-), \tag{3.18}$$

where $\boldsymbol{E}_\omega(r_s^-) = -\nabla\phi^{\rm in}_\omega(r_s)$ and $\boldsymbol{E}_\omega(r_s^+) = -\nabla\phi^{\rm out}_\omega(r_s^+)$ and $\perp$ and $\parallel$ denote the projections normal and parallel to the surface. The nonlinear surface susceptibility in Eq. (3.17) is obtained by using Eqs. (2.54) and (2.57), and including the component $\chi_{{\rm sh},\perp\parallel\parallel}$ (zero within the scope of the model employed here). We get,

$$\begin{aligned}\chi^s_{{\rm sh},ijk} =& \frac{(\epsilon_\omega - 1)^2}{64\pi^2 ne} \Big(\delta_{i\perp}\delta_{j\perp}\delta_{k\perp} \frac{a}{\epsilon_\omega^2} + [(1-\delta_{i\perp})(1-\delta_{j\perp})\delta_{k\perp} \\ &+ (1-\delta_{i\perp})\delta_{j\perp}(1-\delta_{k\perp})] \frac{b}{\epsilon_\omega} + \delta_{i\perp}(1-\delta_{j\perp})(1-\delta_{k\perp}) f \Big),\end{aligned} \tag{3.19}$$

in a local reference frame where one of the Cartesian directions is perpendicular and the others are parallel to the surface. Here, the dimensionless parameters a and b are functions of ω used to parameterize the response of the surface; they are given by Eqs. (2.55) and (2.58) of Sec. 2.3. The third parameter, f, corresponding to the component $\chi_{{\rm sh},\perp\parallel\parallel}$ is zero.

The nonlinear polarization induced on the surface of the cylinder is obtained by substituting Eqs. (3.18) and (3.19) in Eq. (3.17), with the fields in Eq. (3.18) obtained by taking the gradi-

ent of the scalar potential given by Eq. (3.13). Its perpendicular component is

$$P^s_{\mathrm{sh},\perp} = \frac{1}{32\pi^2 ne}\left(\frac{1-\epsilon_\omega}{1+\epsilon_\omega}\right)^2 \Bigg\{(a+f)+(a-f)\cos 2\theta - \xi\left[\left(4\frac{1-\epsilon_\omega}{1+\epsilon_\omega}(a+f)+3(a-f)\right)\cos\theta + 4\frac{1-\epsilon_\omega}{1+\epsilon_\omega}(a-f)\cos 3\theta - 3(a-f)\cos 5\theta\right]\Bigg\} E_0^2, \tag{3.20}$$

and the tangential component is

$$P^s_{\mathrm{sh},\parallel} = \frac{b}{16\pi^2 ne}\left(\frac{1-\epsilon_\omega}{1+\epsilon_\omega}\right)^2 \left\{-\sin 2\theta + \xi\left[4\left(\frac{1-\epsilon_\omega}{1+\epsilon_\omega}\right)\sin 3\theta - 3\sin\theta - 3\sin 5\theta\right]\right\} E_0^2. \tag{3.21}$$

The terms in the above expressions, Eqs. (3.20) and (3.21), independent of the deformation ξ are the components of the local surface nonlinear polarization for a circular cylinder. We can integrate this quadratic polarization over the boundary of the surface to obtain the net quadratic surface dipole moment per unit length for the circular cylinder $\boldsymbol{p}^s_{\mathrm{circ}}$. We write,

$$\boldsymbol{p}^s_{\mathrm{circ}} = \int_0^{2\pi} (P^s_{\mathrm{sh},\perp}(\xi=0)\,\hat{\boldsymbol{r}} + P^s_{\mathrm{sh},\parallel}(\xi=0)\,\hat{\boldsymbol{\theta}})\, r_0\, d\theta, \tag{3.22}$$

where $\hat{\boldsymbol{r}}$ is the unit vector normal and $\hat{\boldsymbol{\theta}}$ is the unit vector tangential to the circular surface respectively. The integral in Eq. (3.22) after substituting the unit vectors and the ξ independent terms of Eqs. (3.20) and (3.21), evaluates to zero. Thus, even though a nonlinear polarization is induced locally at each point of the surface of the circular cylinder, it sums to zero due to the symmetrical form.

The variation of the tangential component $P^s_{\mathrm{sh},\parallel}$ along the surface yields a *surface-originated* contribution to the surface charge σ^s_{sh} beyond that due to the termination of the bulk nonlinear polarization σ^b_{sh}, where we use the superscript s to denote its surface origin. It is given by

$$\sigma^s_{\mathrm{sh}} = -\nabla_\parallel \cdot \boldsymbol{P}^s_{\mathrm{sh},\parallel}, \tag{3.23}$$

where $\nabla_\parallel$ is the gradient operator projected along the surface. Multiplying the tangential component of the surface polarization [Eq. (3.21)] with the unit vector tangential to the surface, given by

$$\hat{\boldsymbol{t}} = \hat{\boldsymbol{\theta}} - 3\xi \sin 3\theta\, \hat{\boldsymbol{r}}, \tag{3.24}$$

and substituting it in Eq. (3.23), we obtain

$$\sigma^s_{\mathrm{sh}} = \frac{b}{8\pi^2 ner_0}\left(\frac{1-\epsilon_\omega}{1+\epsilon_\omega}\right)^2 \left[\cos 2\theta + \xi\left(\cos\theta - 6\frac{1-\epsilon_\omega}{1+\epsilon_\omega}\cos 3\theta + 7\cos 5\theta\right)\right] E_0^2. \tag{3.25}$$

The screened scalar potential ϕ_{sh} induced at the SH frequency has $\rho^{(2)}_{\mathrm{sh}}$ $(=0)$ as an *external bulk*

source and the total nonlinear charges induced at the surface $\sigma^b_{\rm sh}$ and $\sigma^s_{\rm sh}$ as *external surface* sources, together with the normal polarization $P^s_\perp$, which are accounted for through the boundary conditions. The external sources have to be screened by the linear response $\epsilon_{\rm sh}$ of the particle at the SH frequency. Thus the equation to be solved for the quadratic scalar potential is

$$\nabla^2\phi_{\rm sh} = \begin{cases} 0, & \text{(outside)} \\ -4\pi\rho^{(2)}_{\rm sh}/\epsilon_{\rm sh} = 0, & \text{(inside)} \end{cases} \tag{3.26}$$

subjected to the boundary conditions

$$\hat{\boldsymbol{n}}\cdot\nabla\phi_{\rm sh}(r_s^+) - \epsilon_{\rm sh}\hat{\boldsymbol{n}}\cdot\nabla\phi_{\rm sh}(r_s^-) = -4\pi(\sigma^b_{\rm sh}+\sigma^s_{\rm sh}) \tag{3.27}$$

and

$$\phi_{\rm sh}(r_s^+) - \phi_{\rm sh}(r_s^-) = 4\pi P^s_\perp \tag{3.28}$$

Eq. (3.27) is the discontinuity of the normal component of the displacement field due to the presence of the nonlinear surface charge. Eq. (3.28) is the discontinuity of the scalar potential due to the presence of the normal nonlinear surface polarization $P^s_\perp$, which is a dipole layer across the selvedge of the particle. Using a trial solution similar to Eqs. (3.11a) and (3.11b) along with the boundary conditions Eqs. (3.27) and (3.28), we solve Eq. (3.26) to obtain the self-consistent scalar potential at the SH frequency with terms up to linear order in ξ. We obtain,

$$\begin{aligned}\frac{\phi^{\rm out}_{\rm sh}}{E_0^2} =& \frac{\xi}{4\pi ne}\frac{(1-\epsilon_\omega)^2}{(1+\epsilon_{\rm sh})(1+\epsilon_\omega)^2}\left(4\frac{\epsilon_\omega-2\epsilon_{\rm sh}+1}{1+\epsilon_\omega}+2b\frac{1+3\epsilon_{\rm sh}}{1+\epsilon_{\rm sh}}+\frac{\epsilon_{\rm sh}}{2}\frac{(\epsilon_{\rm sh}-3)(a-f)}{1+\epsilon_{\rm sh}}\right.\\ &\left.+\frac{\epsilon_{\rm sh}}{2}\frac{(7\epsilon_\omega-1)f+(\epsilon_\omega-7)a}{1+\epsilon_\omega}\right)\frac{r_0}{r}\cos\theta\\ &+\frac{1}{8\pi ne}\left(\frac{1-\epsilon_\omega}{1+\epsilon_\omega}\right)^2\frac{\epsilon_{\rm sh}(a-f)+2b}{1+\epsilon_{\rm sh}}\frac{r_0^2}{r^2}\cos 2\theta+\ldots\end{aligned} \tag{3.29}$$

on the outside, where we only kept the dipolar and quadrupolar contributions, and neglected higher multipoles, all of which are at least of order ξ, and their contribution to the radiation fields would be insignificant for small particles, at least by a factor of order r_0/λ, with λ the wavelength.

The general expression of the $2D$ scalar potential in polar coordinates, after taking into account the symmetry properties of our system can be written as

$$\phi^{\rm out} = 2p_x\frac{\cos\theta}{r}+Q_{xx}\frac{\cos 2\theta}{r^2}+\ldots \tag{3.30}$$

Finally, comparing Eq. (3.29) and Eq. (3.30) we identify the corresponding components of the

multipolar moments p_x and Q_{xx}, and from Eqs. (3.5) and (3.6) we obtain the dipolar

$$\gamma_{\rm sh}^{d} = \frac{\xi r_0}{8\pi n e}\frac{(1-\epsilon_\omega)^2}{(1+\epsilon_{\rm sh})(1+\epsilon_\omega)^2}\left[4\frac{\epsilon_\omega - 2\epsilon_{\rm sh}+1}{1+\epsilon_\omega} + 2b\frac{1+3\epsilon_{\rm sh}}{1+\epsilon_{\rm sh}} + \frac{\epsilon_{\rm sh}}{2}\frac{(\epsilon_{\rm sh}-3)(a-f)}{1+\epsilon_{\rm sh}} + \frac{\epsilon_{\rm sh}}{2}\frac{(7\epsilon_\omega-1)f+(\epsilon_\omega-7)a}{1+\epsilon_\omega}\right] \tag{3.31}$$

and quadrupolar

$$\gamma_{\rm sh}^{Q} = \frac{r_0^2}{8\pi n e}\left(\frac{1-\epsilon_\omega}{1+\epsilon_\omega}\right)^2\left[\frac{\epsilon_{\rm sh}(a-f)+2b}{1+\epsilon_{\rm sh}}\right] \tag{3.32}$$

nonlinear response functions.

To the lowest order in the deformation parameter, $\gamma_{\rm sh}^{d}$ is proportional to ξ, and thus, as expected, the dipolar response would disappear for a centrosymmetric circular cross-section. On the other hand, $\gamma_{\rm sh}^{Q}$ is independent of ξ, and therefore is the nonlinear response for a symmetric circular cylinder.

There are previous calculations of the nonlinear response of a circular cylinder. An analytical calculation in the retarded regime of the fields radiated at the SH frequency by an infinite circular cylinder can been found in the work by Valencia et al. [53]. However, their results cannot be directly compared with Eq. (3.32) as their calculation was performed for a radius comparable with the wavelength, they took the nonlinear bulk and surface response as parameters and their calculation is not self-consistent in the SH frequency.

From Eqs. (3.31) and (3.32) we can easily identify the contributions arising from the bulk and the surface to the nonlinear hyperpolarizabilities as the latter are proportional to the surface parameters a, b, and f. Thus, $\gamma_{\rm sh}^{d}$ has both surface and bulk contributions, while $\gamma_{\rm sh}^{Q}$ has only surface contributions. Both $\gamma_{\rm sh}^{d}$ and $\gamma_{\rm sh}^{Q}$ inherit the spectral structure of the surface parameters, namely, of $a(\omega)$, and also exhibit additional resonances corresponding to the excitation of surface plasmons or surface plasmon-polaritons at the fundamental and the second harmonic frequencies, given by $\epsilon_\omega = -1$ and $\epsilon_{\rm sh} = -1$ respectively.

3.2 Influence of system symmetry on the SH response

In Sec. 3.1, we have explicitly shown the calculation of the nonlinear response of the infinite cylinder with the external electromagnetic field polarized in the $\hat{\boldsymbol{x}}$ direction. The response of the particle to a perturbing field pointing in any other direction can be evaluated following the procedure demonstrated in the previous section. Thus, the process can be repeated to obtain the different components of the response tensor. It is, however, not necessary to perform such calculations as the presence of different symmetries in the system reduces the number of independent components of the tensor. Our system possesses a mirror symmetry with $x-z$ as the plane of inversion and a

three-fold rotational symmetry in the $x-y$ plane. Taking advantage of the symmetries present in the system, we can calculate the non-zero components of the response tensors and the dependence among them.

We first consider the SH dipolar hyperpolarizability tensor $\boldsymbol{\gamma}^{\boldsymbol{d}}_{\mathbf{sh}}$. The intrinsic permutation symmetry of the SH response tensor ensures that the components of the tensor are equal when the last two Cartesian indices are interchanged, i.e. $\gamma^d_{\mathrm{sh},ijk} = \gamma^d_{\mathrm{sh},ikj}$. The inversion symmetry present in our system can be expressed by the following inversion operator

$$I_y = \begin{pmatrix} 1 & 0 \\ 0 & -1 \end{pmatrix}. \tag{3.33}$$

Applying this symmetry to the different components of the $\boldsymbol{\gamma}^{\boldsymbol{d}}_{\mathbf{sh}}$ tensor,

$$\gamma^d_{\mathrm{sh},ijk} = \sum_{l,m,n} I^{il} I^{jm} I^{kn} \gamma^d_{\mathrm{sh},klm}, \tag{3.34}$$

we obtain the relation

$$\gamma^d_{\mathrm{sh},xxy} = \gamma^d_{\mathrm{sh},xyx} = \gamma^d_{\mathrm{sh},yxx} = \gamma^d_{\mathrm{sh},yyy} = 0 \tag{3.35}$$

Next, we employ the rotational symmetry present in the system to find the relation between the remaining non-zero components. The matrix representing a 120° rotation around the $\hat{z}$ axis is given by

$$R_{2\pi/3} = \begin{pmatrix} -1/2 & -\sqrt{3}/2 \\ \sqrt{3}/2 & -1/2 \end{pmatrix}. \tag{3.36}$$

We apply this symmetry to $\boldsymbol{\gamma}^{\boldsymbol{d}}_{\mathbf{sh}}$,

$$\gamma^d_{\mathrm{sh},ijk} = \sum_{l,m,n} R^{il} R^{jm} R^{kn} \gamma^d_{\mathrm{sh},klm}. \tag{3.37}$$

This leads to the following relation between the non-zero components of the dipolar hyperpolarizability tensor

$$\gamma^d_{\mathrm{sh},xyy} = \gamma^d_{\mathrm{sh},yxy} = \gamma^d_{\mathrm{sh},yyx} = -\gamma^d_{\mathrm{sh},xxx} = -\gamma^d_{\mathrm{sh}}, \tag{3.38}$$

with all the other in-plane components being zero. We verified these results by repeating the calculations presented in Sec. 3.1 for external electric fields pointing along different directions. It turns out that given these symmetry related relations, the nonlinear dipole moment induced in the deformed cylinder rotates clockwise by an angle 2θ when the external electric field is rotated anticlockwise by θ (see Fig. 3.2). Choosing the perturbing field as $\boldsymbol{E}_{\mathrm{ex}} = E_{\mathrm{ex}}(\cos\theta, \sin\theta)$, the local quadratic dipole moment induced in the infinite cylinder is $\boldsymbol{p} = p(\cos 2\theta, -\sin 2\theta)$ with $p = \gamma^d E^2_{\mathrm{ex}}$.

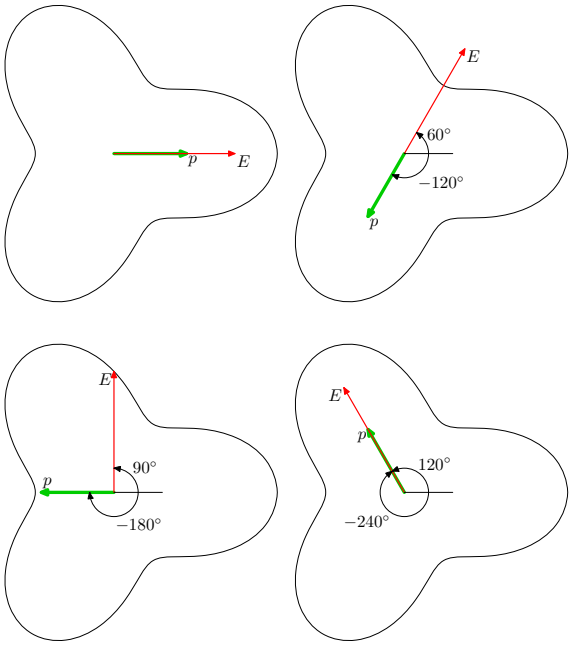

Figure 3.2: Direction of the quadratic dipole moment induced in a deformed cylinder by an external field with different directions with respect to the horizontal. As the field rotates counterclockwise by an angle θ the dipole rotates clockwise by 2θ (color online).

Next, we consider the symmetric, traceless tensor $\boldsymbol{Q}$

$$\boldsymbol{Q} = \begin{pmatrix} Q_{xx} & Q_{xy} \\ Q_{yx} & Q_{yy} \end{pmatrix}, \tag{3.39}$$

with $Q_{xy} = Q_{yx}$ and $Q_{xx}+Q_{yy} = 0$. Thus, Q_{xy} and $Q_{xx}-Q_{yy}$ are the only independent components of the tensor. $\boldsymbol{Q}$ is proportional to $\boldsymbol{EE}$ which is also a symmetric matrix but with 3 independent components E_xE_y, $E_x^2 - E_y^2$ and $E_x^2 + E_y^2 = E^2$. The components of $\boldsymbol{Q}$ can be written as

$$Q_{xx} - Q_{yy} = u(E_x^2 - E_y^2) + v(E_x^2 + E_y^2) + w(E_xE_y) \tag{3.40}$$

$$Q_{xy} = a(E_x^2 - E_y^2) + b(E_x^2 + E_y^2) + c(E_xE_y) \tag{3.41}$$

Applying the inversion symmetry operation, I_y [Eq. (3.33)], $Q_{xx} - Q_{yy}$ should remain unchanged and also $(E_x^2-E_y^2)$ and $(E_x^2+E_y^2)$ terms in Eq. (3.40), but E_xE_y changes sign and hence we conclude $w = 0$. Similarly, applying the inversion symmetry operation to Eq. (3.41), we find that $a = b = 0$ as they remain the same even though Q_{xy} must change its sign. Next applying the rotational symmetry operation given by matrix $R_{2\pi/3}$ [Eq. (3.36)] to $\boldsymbol{Q}$, we get

$$Q'_{xx} - Q'_{yy} = -\frac{1}{2}(Q_{xx} - Q_{yy}) + \sqrt{3}Q_{xy}, \tag{3.42}$$

$$Q'_{xy} = -\frac{\sqrt{3}}{4}(Q_{xx} - Q_{yy}) - \frac{1}{2}Q_{xy}, \tag{3.43}$$

while by rotating the electric fields we get

$$Q'_{xx} - Q'_{yy} = -\frac{u}{2}(E_x^2 - E_y^2) + \sqrt{3}uE_xE_y + vE^2, \tag{3.44}$$

$$Q'_{xy} = -\frac{\sqrt{3}}{4}c(E_x^2 - E_y^2) - \frac{1}{2}cE_xE_y. \tag{3.45}$$

Comparing Eqs. (3.42) and (3.44) and using Eqs. (3.40) and (3.41) we obtain $u = u$, $v = 0$, and $c = v$ and comparing Eqs. (3.43) and (3.45) we obtain $c = v$ and $c = c$. Thus, there remains only one independent component of $\boldsymbol{Q}$ which is $(Q_{xx} - Q_{yy}) \propto (E_x^2 - E_y^2)$. Hence, the symmetry in our system leads to an isotropic quadrupolar response given by $Q_{ij} = \gamma_{\mathrm{sh}}^{Q}(2E_iE_j - E^2\delta_{ij})$. The quadratic quadrupolar moment has a principal axis along the external field and the only non-null components of the quadrupolar hyperpolarizability are,

$$\gamma^{Q}_{\mathrm{sh},xxxx} = -\gamma^{Q}_{\mathrm{sh},xxyy} = -\gamma^{Q}_{\mathrm{sh},yyxx} = \gamma^{Q}_{\mathrm{sh},yyyy} = \gamma^{Q}_{\mathrm{sh},xyxy} = \gamma^{Q}_{\mathrm{sh},yxxy} = \gamma^{Q}_{\mathrm{sh},xyyx} = \gamma^{Q}_{\mathrm{sh},yxyx} = \gamma^{Q}_{\mathrm{sh}}. \tag{3.46}$$

Thus, for this system our calculations of γ^{d}_{sh} and γ^{Q}_{sh} using an external field along $\hat{\boldsymbol{x}}$ are sufficient to obtain the full response of the particle.

The symmetry in our system also ensures that no nonlinear magnetic dipole is induced in our nanowire in the nonretarded regime. We write the magnetic dipole as a response function $m_z = \chi^{m}_{zij}E_iE_j$ where $\boldsymbol{m}$ is a pseudovector and $\boldsymbol{E}$ is a vector, so χ^{m}_{zij} is a pseudotensor; it is symmetric in the indices i, j. Applying the rotation operation given by Eq. (3.36) to the tensor, we obtain χ^{m}_{zij} proportional to δ_{ij} and then using the inversion operation, Eq. (3.33), gives $\chi^{m}_{zij} = 0$. Hence, it is not included in our work. The calculation to explicitly show the relations between the components of the quadratic magnetic susceptibility tensor is not presented here, but could be done in a similar fashion following the procedure for the electric dipolar hyperpolarizability in Eqs. (3.34) and (3.37). However, we should comment that as the particle size increases and the effects of retardation become important, the external field perturbing the system cannot be treated as homogeneous and its spatial variations must be taken into consideration. Some nonlinear response terms would require additional nonlocal contributions to the quadratic electric dipolar response. A nonzero nonlinear magnetic dipole may also be induced in such a situation. For larger particles, the magnetic contribution to the SH response may prove to be dominant over others. It has, however, been reported that excitation of this quadratic magnetic dipole from infinite cylinders with arbitrary shape of the cross-section is absent for cases where the cross-section is symmetric about an axis along the direction of incidence [44]. Klein et al. [5] demonstrated SHG from different metamaterials formed of arrays of split ring resonators SRRs, T shaped inclusions, and straight wires fragments; they found that the SHG for the SRR structure was largely dominated by a magnetic dipole resonance, but not for the straight wires fragments nor the T shaped structures. However, it was later reported otherwise in ref. [151]. They presented a theoretical calculation of SHG using the hydrodynamic model and showed that nonlinear optical properties of SRRs could be explained solely by contributions of electric origin.

3.3 SH radiation

We now turn our attention towards the calculation of the SH angular radiation pattern. Following a procedure similar to the $3D$ case, one can write down the expressions for the radiated electromagnetic fields in $2D$ due to localized distributions of charges and currents. Appendix A provides a detailed account of the theory of electromagnetic radiation in $2D$ and illustrates explicitly the derivation of the fields in the radiation zone.

In our case, the electric dipole and the electric quadrupole are the dominant contributions to the radiation fields as the other higher order terms are negligible in comparison. The quadrupolar contribution is usually smaller than the dipolar by r_0/λ, with r_0 the size of the particle. However, in our case the quadrupole is independent of the deformation while the dipole is null for zero deformation. Thus, both contributions to the radiated SH fields may be comparable. Adding the expressions for the $\boldsymbol{B}$ field from Eq. (A.20) and Eq. (A.38) [see Appendix (A)], the total $\boldsymbol{B}$ field radiated from the cylinder is

$$\boldsymbol{B} = (1+i)k^{3/2}\left((\hat{\boldsymbol{r}}\times\boldsymbol{p}) - \frac{i}{4}k(\hat{\boldsymbol{r}}\times(\boldsymbol{Q}\cdot\hat{\boldsymbol{r}}))\right)e^{ikr}\sqrt{\frac{\pi}{r}}, \tag{3.47}$$

where k is the wavenumber and $\hat{\boldsymbol{r}}$ is the unit vector in the direction of observation. The $\boldsymbol{E}$ field can be calculated from Eq. (3.47) by using

$$\boldsymbol{E} = \boldsymbol{B}\times\hat{\boldsymbol{r}}, \tag{3.48}$$

The time averaged power radiated per unit angle θ due to these radiated electromagnetic fields is given by

$$\frac{dP}{d\theta} = \frac{rc}{2\pi}\,\mathrm{Re}[\boldsymbol{E}\times\boldsymbol{B}^*]\cdot\hat{\boldsymbol{r}}. \tag{3.49}$$

Substituting Eqs. (3.47) and (3.48) in Eq. (3.49), and using the relations for the induced quadratic dipolar and quadrupolar moments in terms of the respective hyperpolarizabilities using Eqs. (3.2) and (3.4) to (3.6), we obtain

$$\begin{aligned}\frac{dP}{d\theta} =& \frac{cE_0^4k^3}{4}\Big(4|\gamma_{\mathrm{sh}}^d|^2\sin^2\theta - 4k\,\mathrm{Im}(\gamma_{\mathrm{sh}}^d\gamma_{\mathrm{sh}}^{Q*})\sin^2\theta\cos\theta \\ &+ k^2|\gamma_{\mathrm{sh}}^Q|^2\sin^2\theta\cos^2\theta\Big).\end{aligned} \tag{3.50}$$

The first and last terms correspond to dipolar and quadrupolar radiation, while the middle term corresponds to their interference.

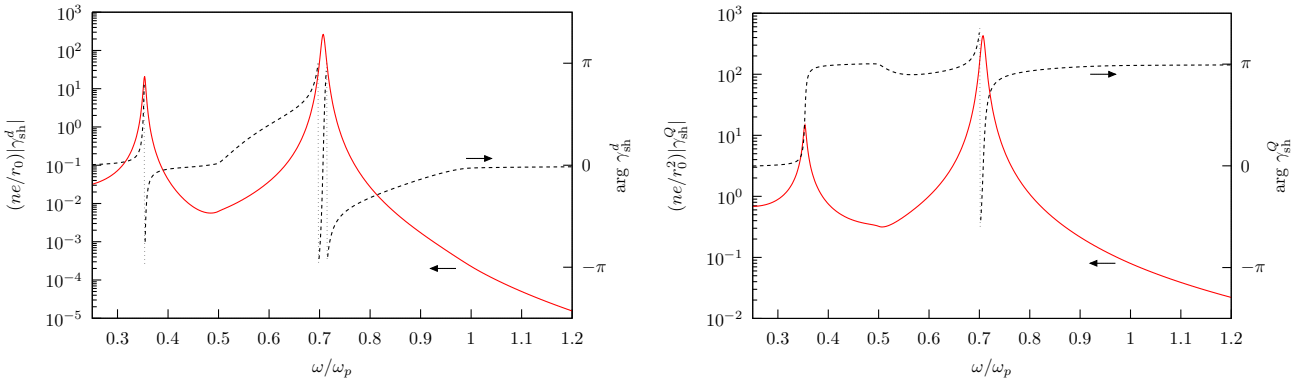

Figure 3.3: Normalized absolute value (solid) and phase (dashed) of the dipolar (left panel) and quadrupolar (right panel) nonlinear response functions $\gamma^d_{\rm sh}$ and $\gamma^Q_{\rm sh}$ for a cylinder with deformation parameter $\xi = 0.01$ made of a Drude metal as a function of the normalized frequency $\omega/\omega_{\rm p}$. The irrelevant abrupt 2π phase jumps are indicated with dotted vertical lines.

3.4 Results and Discussions

We consider an infinite cylinder made up of a Drude metal characterized by its bulk plasma frequency $\omega_{\rm p}$ and electronic relaxation time τ, with dielectric function [141]

$$\epsilon_{\rm m}(\omega) = 1 - \omega_{\rm p}^2/(\omega^2 + i\omega/\tau). \tag{3.51}$$

We consider a small deformation $\xi = 0.01$ and chose a small dissipation factor $1/\omega_{\rm p}\tau = 0.01$. The cylinder is illuminated by a TM electromagnetic wave propagating along the y axis with an electric field pointing along the x axis. We chose a nominal radius $r_0 = c/4\omega_{\rm p}$. Note that the frequencies we have chosen are of the order $\omega_{\rm p}$, which makes λ of the order of $2\pi c/\omega_{\rm p}$, so r_0/λ is of the order of $1/8\pi \approx 4\%$, the radius is small compared to the wavelength and we may assume the incoming field to be constant within the particle and use the expressions obtained in the previous section corresponding to a homogeneous external field. We reiterate that while the nonlinear dipolium model [124] was originally developed for insulating materials, as it corresponds to a continuous distribution of small polarizable entities around which the electrons are localized, its results agree with those of a nonlinear hydrodynamical calculation [125] on a local *jellium* model of a conducting electronic fluid as has been discussed in Chapter 2. Thus, the results of the dipolium model may as well be applied to metals as to semiconductors and insulators as long as the results are written in terms of the linear dielectric response evaluated at the fundamental and SH frequencies, though there may be corrections arising from the spatial dispersion of the electron gas [152].

In Fig. 3.3 we show the absolute values and phases of the nonlinear dipolar and quadrupolar response functions $\gamma^d_{\rm sh}$ and $\gamma^Q_{\rm sh}$ [Eqs. (3.31) and (3.32)]. Notice that both display very large resonant peaks corresponding to the surface plasmon resonance of the cylinder $\omega_{\rm sp} = \omega_{\rm p}/\sqrt{2}$ and its sub-harmonic. Beyond abrupt changes at these resonances, the phase of $\gamma^d_{\rm sh}$ shifts away from 0 in a wide region

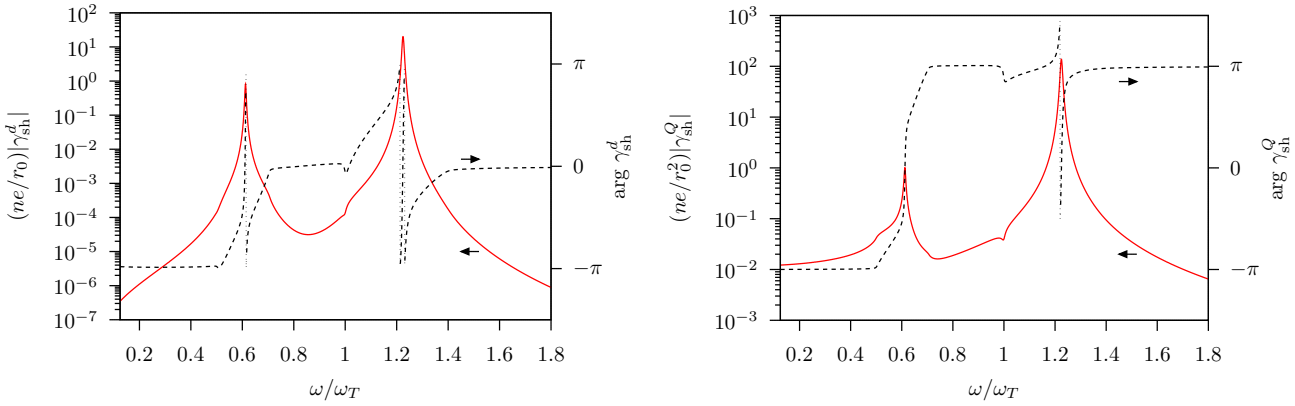

Figure 3.4: Normalized absolute value (solid) and phase (dashed) of the dipolar (left panel) and quadrupolar (right panel) nonlinear response functions $\gamma^d_{\rm sh}$ and $\gamma^Q_{\rm sh}$ for a cylinder made of a dispersive dielectric with a Lorentzian resonance characterized by a longitudinal $\omega_{\rm L}$ and a transverse $\omega_{\rm T}$ frequency with $\omega_{\rm L} = \sqrt{2}\omega_{\rm T}$, a lifetime $\tau = 100/\omega_{\rm T}$, and a deformation parameter $\xi = 0.01$, as a function of the normalized frequency $\omega/\omega_{\rm T}$. The irrelevant abrupt 2π phase jumps are indicated with dotted vertical lines.

that spans from $\omega_{\rm p}/2$ up to $\omega_{\rm p}$. This is due to the logarithm term in Eq. (2.55), whose argument changes sign as ω or 2ω sweeps across the plasma frequency [124]. The phase of $\gamma^Q_{\rm sh}$ also displays a smooth variation of around 2π in the same region.

In Fig. 3.4 we show the absolute values and phases of $\gamma^d_{\rm sh}$ and $\gamma^Q_{\rm sh}$ for a similar deformed cylinder but made up of a dispersive insulator with a dielectric function which we assume has a single Lorentzian resonance and of the form given by Eq. (2.26) with the frequencies of its longitudinal $\omega_{\rm L}$ and transvers $\omega_{\rm T}$ optical modes related by $\omega_{\rm L}^2 = 2\omega_{\rm T}^2$ and dissipation $\tau = 100/\omega_{\rm T}$. The dielectric function crosses zero at $\omega_{\rm L}$ and has a pole at $\omega_{\rm T}$. Both $\gamma^d_{\rm sh}$ and $\gamma^Q_{\rm sh}$ show strong resonant peaks corresponding to the excitation of the surface plasmon-polariton, which for our choice of parameters lies at $\omega = \omega_{\rm spp} = \omega_{\rm T}\sqrt{3/2}$, and its sub-harmonic. The phase of both $\gamma^d_{\rm sh}$ and $\gamma^Q_{\rm sh}$ grows smoothly between $\omega_{\rm T}/2$ and $\omega_{\rm L}/2$, and between $\omega_{\rm T}$ and $\omega_{\rm L}$, save for abrupt jumps at $\omega_{\rm spp}/2$, $\omega_{\rm T}$ and $\omega_{\rm spp}$, and remain constant otherwise. Some features in the phase of $\gamma^d_{\rm sh}$ and $\gamma^Q_{\rm sh}$ are inherited from those of the parameter a [124]. We remark that close to a simple resonance, a Lorentzian response displays a rapid change of phase of π due to the change of sign of its real part across a pole. For a double or triple resonance the corresponding change in phase would be 2π or 3π. We note that in our expressions for $\gamma^d_{\rm sh}$ and $\gamma^Q_{\rm sh}$ [Eqs. (3.31) and (3.32)] there are different terms displaying resonances of order 1, 2 and 3 and hence the total phase across a resonance depends on the competition between them. A logarithmic contribution to the phase is also present due to the contribution of the parameter a to some terms. The above leads to distinct changes of the phase across the different resonance peaks in Figs. 3.3 and 3.4, with a magnitude that depends on which term dominates. On the other hand, the vertical -2π abrupt jumps are irrelevant as they arise trivially from the fact that the phase is defined modulo 2π. Note that at resonance, the dipolar hyperpolarizability (per unit length) is an order of magnitude larger than r_0/ne, where r_0 is the nominal radius of the

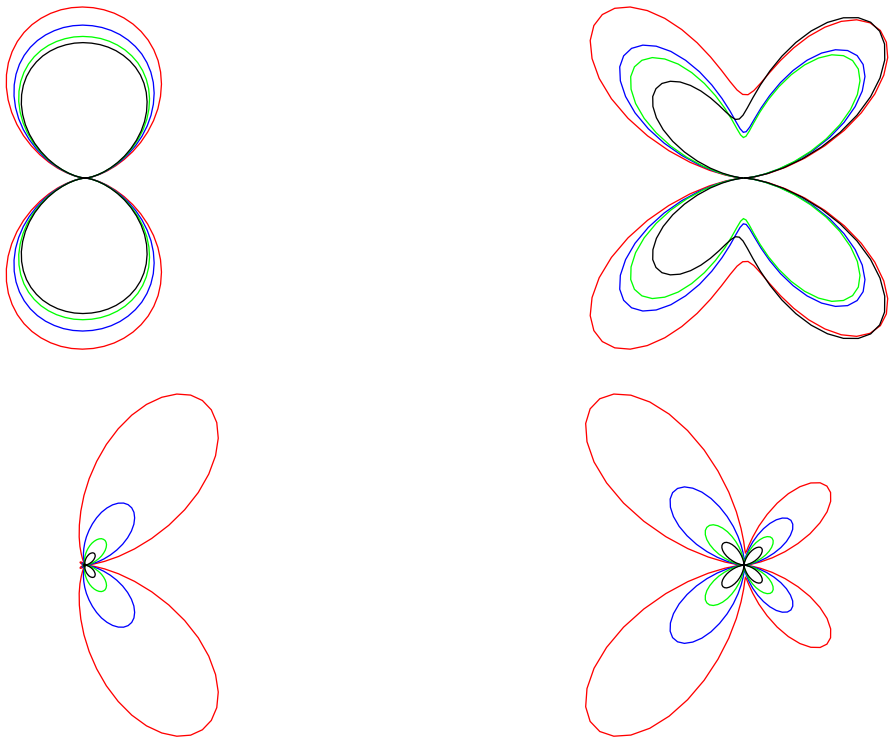

Figure 3.5: Angular radiation pattern for a deformed metallic cylinder with deformation parameter $\xi = 0.01$ described by a Drude response for frequencies ω approaching $\omega_{\rm sp}$ or to its sub-harmonic: $\omega < \omega_{\rm sp}/2$ (upper left), $\omega_{\rm sp}/2 < \omega$ (upper right), $\omega < \omega_{\rm sp}$ (bottom left), and $\omega_{\rm sp} < \omega$ (bottom right). As ω approaches a resonance the total radiated power increases

infinite cylinder, n is the polarizable entity or the electronic number density and e is the electronic charge (see Figs. 3.3 and 3.4). Thus, we expect that the dipolar nonlinear susceptibility of a metamaterial made up of these particles to be atleast an order of magnitude larger than $1/ner_0$. We assume the area of the unit cell of the metamaterial to be of the order r_0^2 and divide the dipolar hyperpolarizability by the area of the unit cell to obtain the dipolar nonlinear susceptibility of the metamaterial. The typical susceptibility of noncentrosymmetric materials is given by Eq. (1.2), of order $1/nea_b$. A metamaterial made of centrosymmetric materials with a noncentrosymmetric geometry, thus, may be a competitive source of SH provided a_b/r_0 is not too small.

In Fig. 3.5 we show a polar plot of the angular radiation pattern $dP/d\theta$ vs. the polar angle θ corresponding to a deformed metallic cylinder as the one in Fig. 3.3. Notice there is a competition between the dipolar and quadrupolar contributions to the radiation, and that their relative strength varies as the frequency increases. We remark that the SH dipole would be zero for the non-deformed cylinder, but for deformations as small as 1% its contribution to the radiation is comparable to the quadrupolar contribution. Fig. 3.5 shows that for low frequencies, $\omega < \omega_{\rm sp}/2$ displayed in the top left panel, the radiation is completely dominated by the dipolar term and it displays the typical

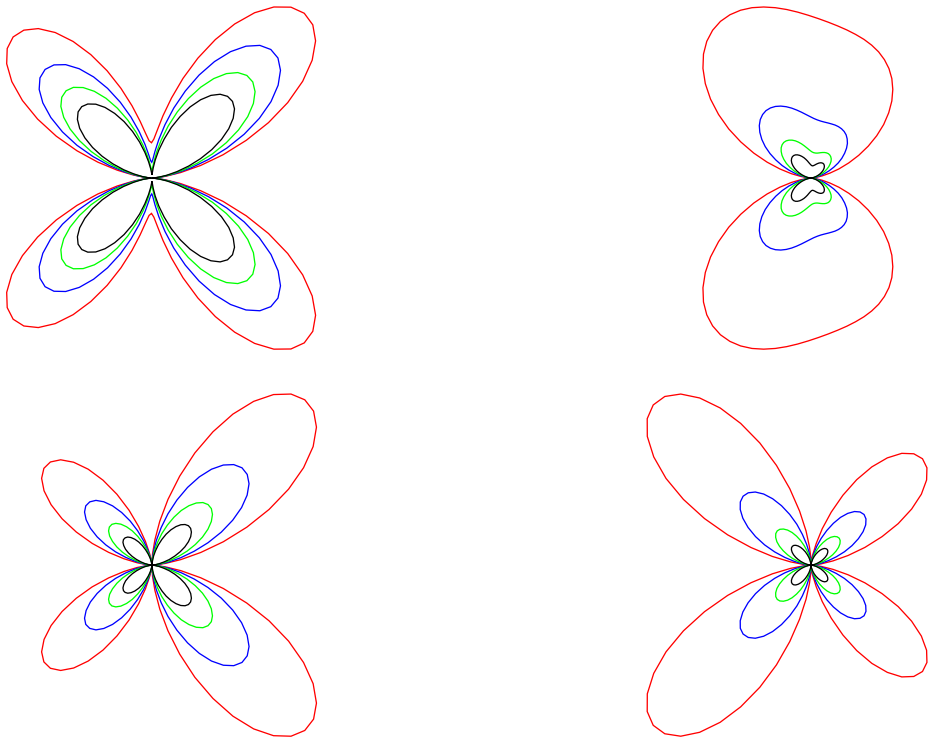

Figure 3.6: Angular radiation pattern for a deformed dielectric cylinder with deformation parameter $\xi = 0.01$ described by a simple Lorentzian response with negligible dissipation for frequencies ω close to $\omega_{\rm spp}$ or its sub-harmonic: $\omega < \omega_{\rm spp}/2$ (upper left), $\omega_{\rm spp}/2 < \omega$ (upper right), $\omega < \omega_{\rm spp}$ (bottom left), and $\omega_{\rm spp} < \omega$ (bottom right). As ω approaches a resonance the total radiated power increases.

pattern consisting of two symmetrical lobes. As the frequency moves towards the resonance the total radiated power increases, hence, the outermost curve in the top left panel corresponds to a frequency slightly below the resonance at $\omega_{\rm sp}/2$. For higher frequencies the pattern becomes largely quadrupolar. The top right panel corresponds to $\omega > \omega_{\rm sp}/2$ for which the quadrupolar contribution overshadows the dipolar contribution and a four lobed pattern emerges. It is somewhat asymmetrical due to the interference with the dipolar field. Also note the shift in the size of the lobes from left to right as one moves away from the resonance at $\omega_{\rm sp}/2$. The bottom left panel illustrates the radiation pattern for frequencies approaching $\omega_{\rm sp}$ from below and is predominantly dipolar with an influence of the quadrupolar contribution which makes it asymmetrical. Radiation at frequencies above that of the surface plasmon $\omega > \omega_{\rm sp}$ is shown in the bottom right panel. In this region too, the pattern is mostly quadrupolar displaying four lobes which are asymmetrical due to the interference with the dipolar contribution to the radiation.

In Fig. 3.6 we show the SH angular radiation pattern as in Fig. 3.5 but corresponding to a dielectric particle as in Fig. 3.4. Here, we also see the competition between the dipolar and the quadrupolar radiation with the variation in frequency and the asymmetry in the different lobes of the quadrupolar

pattern arising due to the phase difference between the two terms. Similar to Fig. 3.5, as the frequency approaches a resonance the total radiated power increases. However, the quadrupolar contribution to the radiation is stronger at lower frequencies in this case unlike the metallic case (Fig. 3.5). In the top left panel we plot the patterns for $\omega < \omega_{\text{spp}}/2$ where the quadrupolar contribution to the radiation dominates the dipolar one and is therefore almost symmetric. The top right panel illustrates the radiation for frequencies $\omega > \omega_{\text{spp}}/2$. The outermost curve, closest and slightly above the resonance at $\omega_{\text{spp}}/2$ displays a slightly distorted dipolar pattern. Moving away from the resonance, the quadrupolar term gets relatively stronger and the competition between the two terms gives rise to an asymmetry in the pattern. The bottom left panel shows the pattern for $\omega < \omega_{\text{spp}}$ and it shows asymmetrical quadrupolar patterns. The bottom right panel shows the radiation at higher frequencies $\omega > \omega_{\text{spp}}$ which is also symmetric and almost quadrupolar like radiation.

As demonstrated in Sec. 3.2, the dipolar and the quadrupolar response remains of the same size as the polarization direction of the incoming light rotates. However, as already discussed, as the polarization of the incoming field rotates away by an angle θ away from the x axis, the induced quadratic dipolar moment rotates by twice the angle in the opposite direction, while the axes of the quadrupole moment rotate with the external field (see Sec. 3.2). The effect of these rotations is illustrated in Fig. 3.7 where the radiation patterns for various directions of the external field have been plotted for the same cylinder as in Fig. 3.6. We remark that the dipole changes sign with a 180 rotation and the quadrupole with a 90 degrees rotation. Hence, when the polarization of the incident light is rotated by an angle of 90 degrees anticlockwise, the quadratic dipole moment changes sign and the quadrupole interchanges its principal axes, so the radiation patterns for the external field polarized at 0 degrees (Fig. 3.6) and 90 degrees (bottom right panel of Fig. 3.7) look identical, though the overall phase of the radiated fields is reversed. The radiation pattern for the incident field after a counterclockwise rotation by an angle of 30 degrees (top left panel of Fig. 3.7) is also identical to the one with 0 degrees, except for being rotated anticlockwise in the $x-y$ plane by an angle of 120 degrees; and accompanied with a change of sign in the overall phase. Notice, that every 30 degrees rotation of the polarization is equivalent to a 120 degrees rotation of the radiation pattern in the same clock direction with an overall inversion in the sign of the phase. Thus, when the polarization is rotated by 60 degrees counterclockwise (bottom left panel of Fig. 3.7), the radiation pattern rotates by 240 degrees with no change in the form of the pattern and the sign of the phase compared to that of 0 degrees (Fig. 3.6). The 45 degrees (top right panel of Fig. 3.7) case is different than the others, as it does not mimic any of the symmetry condition of the original case, thus producing not just a rotation in the patterns but also a considerable change in its shape. The effect of the polarization of light on the efficiency of SHG has been demonstrated experimentally by Czaplicki et al. [20]. They studied arrays of noncentrosymmetric nanoparticles with the form of letter T and L to illustrate the effect on geometry combined with polarization on the efficiency of the SH conversion process.

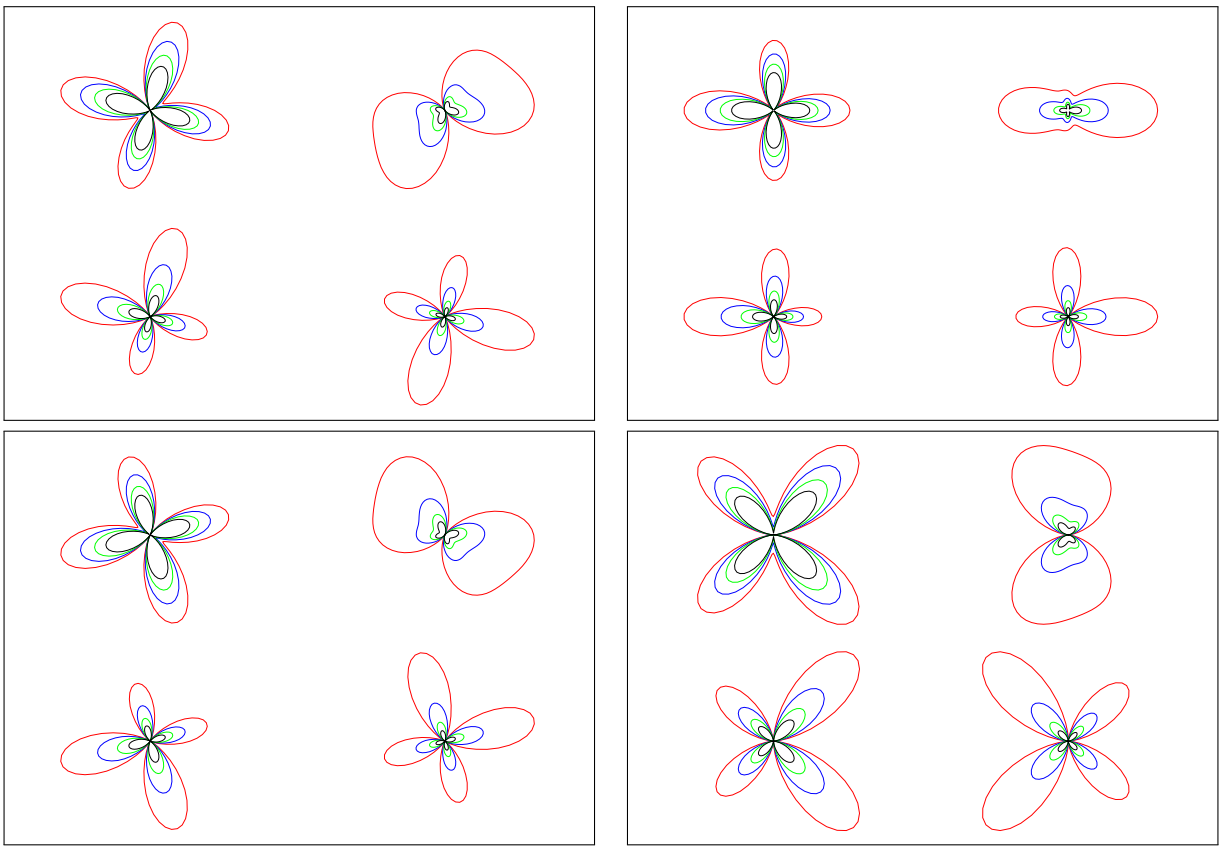

Figure 3.7: Angular radiation pattern of the same deformed dielectric cylinder as in Fig. 3.6 for different frequencies below, between, and above the resonances at the fundamental and SH frequency for various external polarization. The curves for different frequencies follow the same pattern as in Fig. 3.6 The angle ϕ formed between the external electric field and the $\hat{x}$-axis for each figure are 30°(top left panel), 45°(top right panel), 60°(bottom left panel), and 90°(bottom right panel).

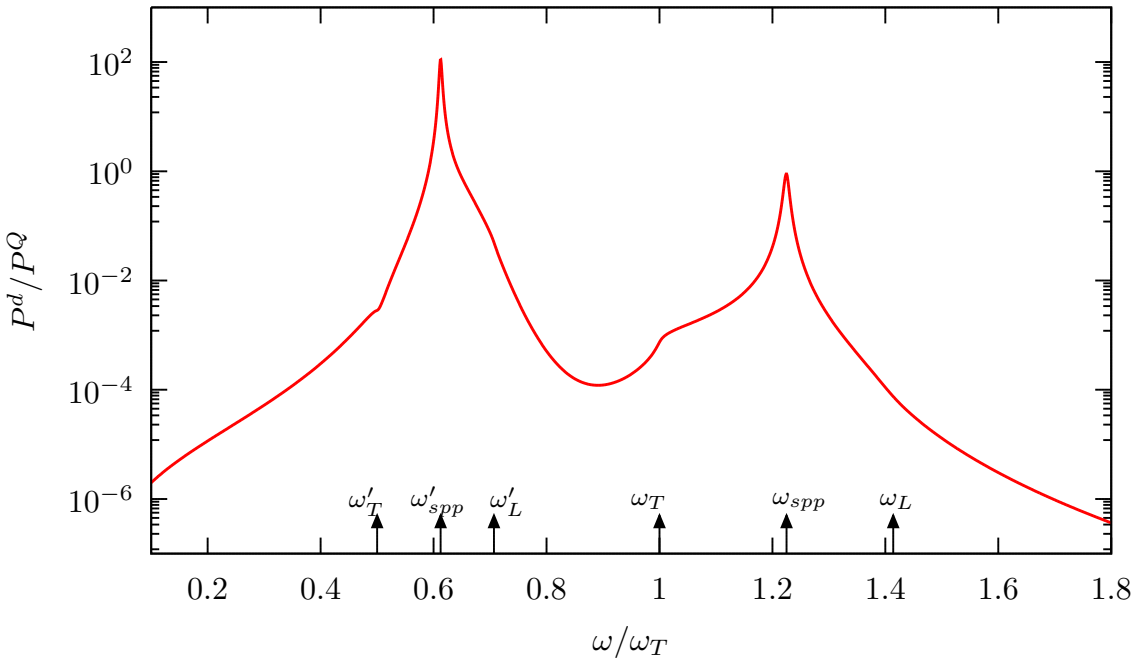

Figure 3.8: Ratio of the total power emitted as dipolar radiation to quadrupolar radiation for the same deformed dielectric cylinder as in Fig. 3.6.

Integrating the expression for the angular radiation pattern we may obtain the total power radiated. In Fig. 3.8 we show the ratio between the total power emitted as by the SH dipole and quadrupole moments for the same dielectric particle as in Fig. 3.6. The peak total power emitted as dipolar radiation is two orders of magnitude higher than the quadrupole at the subharmonic of the surface plasmon polariton, of the same order at the fundamental resonant frequency. We recall that this calculation corresponds to a small deformation $\xi = 0.01$, so it is clear that the dipolar response is essential even for very small deformations. Similar to that of the dielectric cylinder [Fig. 3.8], the ratio between the dipolar and quadrupolar contribution to total SH power for the same metallic deformed cylinder as in Fig. 3.3 is shown in Fig. 3.9. Resembling the dielectric case, the peak power emitted as the dipolar radiation is higher than the quadrupolar at the sub-harmonic of the surface plasmon polariton. Notice, for both metallic and dielectric cylinders, that out of resonance the quadrupole may reach values up to four orders of magnitude higher than the dipole.

Finally, we emphasize that our results above are applicable to systems strictly in $2D$, while experimental realizations would most certainly be 3D, and we expect any nanowire to be of finite length. Nevertheless, our results may still be partially applicable for finite cylinders. Our calculation of the dipolar and quadrupolar nonlinear hyperpolarizabilities will hold true as long as the length l of the finite cylindrical nanowire is much larger than its nominal radius r_0, a condition which is mostly obeyed in the experimental realization of nanowires. The $2D$ electromagnetic radiation in the plane of the cross-section of the infinite cylinder was obtained in the radiation zone, where we assumed the distance r to the axis of the cylinder to be much larger than the wavelength. However, it must hold

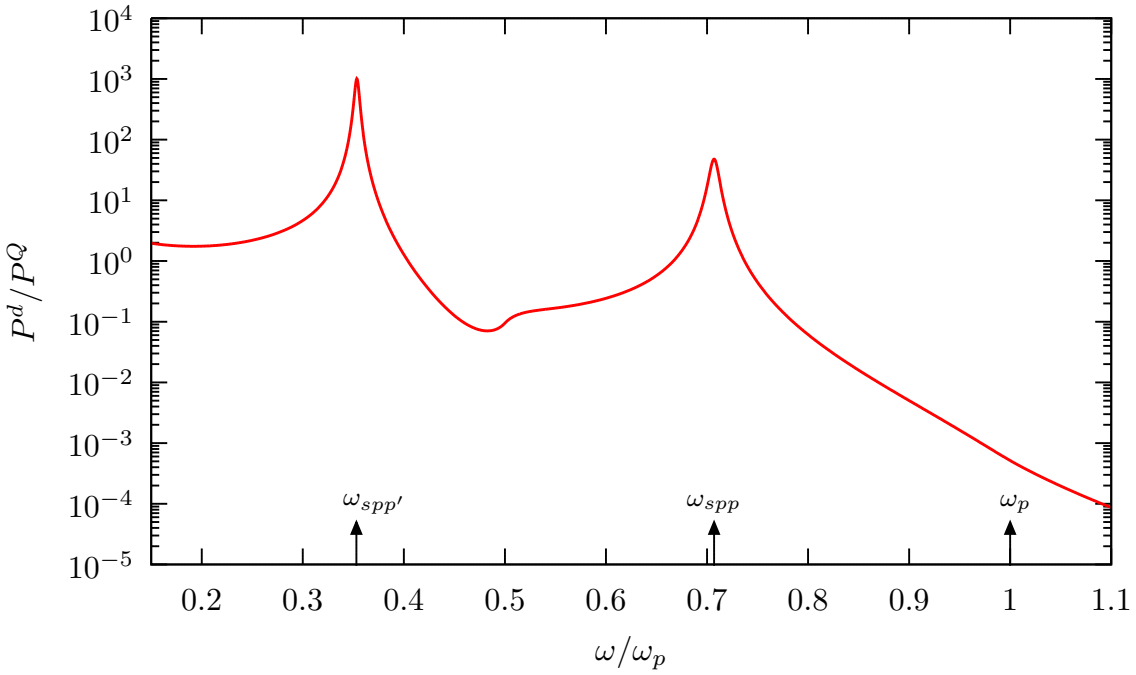

Figure 3.9: Ratio of the total power emitted as dipolar radiation to quadrupolar radiation for the same deformed metallic cylinder as in Fig. 3.5.

that this distance is smaller than the length of the cylinder. Thus, our calculated patterns would only be observable where the condition $r_0 \ll \lambda \ll r \ll l$ may be satisfied. Farther away, the 3D nature of the radiation pattern ought to be accounted for, and it might be calculated using antenna theory. Nevertheless, we emphasize that we expect that the *relative* magnitude between the dipolar and quadrupolar contributions to the radiation will remain as calculated above. A discussion of the effect of the finite length of the cylinder can be found in the work by Dadap [54].

3.5 Conclusions

An analytical perturbative formalism to study the SH response of an isolated particle made of centrosymmetric material with a cross-section slightly deformed away from that of a symmetrical geometry was developed. The exact solution for a perfect cylinder being known, choosing the extent of this deformation as a smallness parameter permits the development of a perturbative approach to find approximate solutions for the noncentrosymmetric system. Closed form expressions for the self-consistent near fields induced at the fundamental and SH frequency within and beyond the cylinder were thus obtained. The linear fields within and near the surface of the particle were employed to calculate the nonlinear polarization induced within the bulk and on the surface of the particle by using the results of the dipolium model [124]. The induced nonlinear polarization was then utilized to calculate the self consistent SH fields and the nonlinear hyperpolarizabilities. The zeroth order term in their expansion in powers of the deformation parameter corresponds to

the case of a symmetric cylinder yielding no SH dipole but a nonzero quadrupolar response. At first order in the deformation, the existence of a small deviation from centrosymmetrical geometry yields a dipolar contribution which increases linearly with the deformation and competes with that of the quadrupole already for very slightly deformations in metallic and dielectric particles. There are higher order multipoles, but they were found to generate a much weaker signal and were hence ignored in our analysis. The quadratic hyperpolarizabilities obtained are written in terms of the linear dielectric response of the material at the fundamental and SH frequencies and were found to have resonant structures corresponding to the poles and zeroes of the dielectric function, and to the surface plasmon or surface plasmon-polariton frequencies of the undeformed particle, and to their sub-harmonics, as well as additional structure due to the normal nonlinear surface parameter a. Finally, the radiated SH fields were also evaluated to illustrate the $2D$ angular radiation patterns and we showed that the dipolar SH radiation is comparable and may overshadow the quadrupolar contribution for deformations as small as 1%.

We remark that our calculation of the nonlinear response of a particle showed that there are some subtleties that have to be accounted for: bulk contributions, bulk induced surface charges, surface originated surface charges and surface dipolar layers. All of these have to be appropriately screened to get consistent expressions for the hyperpolarizabilities and have not received the required attention previously. We must point out that we expect our calculation to fail to describe spectral features in the nonlinear response arising from intrinsic surface effects such as those due to transitions to and from the surface states, surface reconstruction and relaxation etc., as these effects are ignored in the *dipolium* model. Local field effects and crystal structure have also not been accounted for. However, the comparison of our calculation with experimental results may allow us to identify the importance of those contributions we left out.

One of the purposes of this analytical calculation on the simplest possible noncentrosymmetric system is to establish a testing framework for different numerical methods employed to analyze SH response. One can compare and calibrate the numerical calculations by comparing their results to these expressions, and if proved correct, apply them to the analysis of a larger class of systems. One such attempt has been performed by us and the results are presented in Chapter 5 of this thesis.

4

Three wave mixing in a nanowire

Not only second harmonic generation (SHG) (see Chapter 3), but all second order processes, such as sum frequency generation (SFG), difference frequency generation (DFG), and optical rectification (OR), are null in the bulk of centrosymmetric system within the dipolar approximation. Multipolar excitations may produce a second order response from the bulk of such systems together with a dipolar contribution arising only from their surface where the inversion symmetry is locally lost. As previously discussed, in Chapter 3 for SHG, the symmetry reduction also governs the dipolar SF/DF response from nanoparticles and nanostructures made up of centrosymmetric materials. DFG from a monolayer of MoS_2, which is centrosymmetric, has been observed by Wang et. al [153]. To obtain a dipolar SF/DF response from nanoparticles made of centrosymmetric materials it is necessary to destroy their overall symmetry either by applying external fields, or by using a noncentrosymmetric geometry. Efficient SHG and SFG from a silicon metasurface have been demonstrated experimentally [154]. Plasmonic noncentrosymmetric structures might offer an advantage due to their enhancement of local fields, yielding higher nonlinear conversion efficiencies. Theoretical calculation of the DF response from arbitrary plasmonic systems by solving the hydrodynamic equations have been reported [60]. The authors employed their theory to solve the equations using the *COMSOL Multiphysics* commercial computational system to study the DFG efficiency from noncentrosymmetric gold nanoantennas. Generation of terahertz (THz) radiation, as discussed in Sec. 1.1, is an important application of DFG and OR processes and has been extensively studied [59, 155, 156]. Surface Lattice Resonances (SLRs) for enhancing DFG processes leading to both optical rectification (OR) and Terahertz (THz) generation from equilateral triangular gold nanoprisms has been theoretically investigated using the Discrete Dipole Approximation (DDA) by Huttunen et. al [59]. A finite difference time domain (FDTD) calculation based on the Maxwell-hydrodynamic model to theoretically investigate THz generation as a result of DFG process from a plasmonic metasurface has been published by Fang et. al [155].

Here, we present a theory to analytically compute the second order susceptibility of an isolated nanowire made up of a centrosymmetric material with a noncentrosymmetric geometry, with em-

phasis on difference frequency (DF) response. We chose the same shape same as in Chapter 3. To be able to find an approximate analytical solution to the problem, the perturbative technique employed in the previous chapter is used. The linear and nonlinear self-consistent induced fields within and beyond the nanowire are calculated; they are then used to evaluate the nonlinear polarization which acts as a source for the DF fields. We identify the DF response from the obtained near DF fields. Once the DF hyperpolarizability is obtained, the sign of one of the input frequencies is reversed and the complex conjugate of the corresponding dielectric permittivity is substituted in the equations to obtain the SF hyperpolarizabilities. The degenerate SH hyperpolarizabilities are simply found by adding the condition of equality of the input frequencies in the SF response. We unite the SF and the DF response, and discuss their spectral features. Furthermore, we employ the near fields to calculate the far fields and find the SF/DF angular radiation pattern and the radiated SF/DF power from which we evaluate the efficiency of the SF/DF nonlinear conversion process. To calculate the nonlinear surface and bulk polarization, we use the dipolium model [124] discussed in Sec. 2.2. We also discuss the viability of utilizing this structure for the generation of Terahertz (THz) radiation.

We devote Sec. 4.1 to demonstrate a detailed derivation of the DF dipolar and quadrupolar hyperpolarizability of the thin deformed infinitely long cylinder following the methodology developed in Sec. 3.1. The SF response is then identified from the DF response. We present the calculation of the efficiency of the SFG/DFG process from the cylinder in Sec. 4.2. We illustrate and discuss our results for a dielectric and a metallic cylinder in Sec. 4.3. We summarize our findings in Sec. 4.4.

4.1 Three wave mixing in the isolated infinite cylinder

We choose a single infinitely long isolated cylinder made of a centrosymmetrical material placed in vacuum, identical to the one whose SH response was calculated in Chapter 3. The cylinder possesses translational symmetry along its axis ($\hat{z}$ direction), allowing us to perform all calculations in $2D$. The transverse cross-section of the cylinder in the $x-y$ plane is given by Eq. (3.1) [See Fig. 3.1]. We perturb the system by two monochromatic beams of light oscillating at frequencies ω_1 and ω_2. We choose both the incident beams to be polarized in the plane of the cross-section and perpendicular to each other. Our choice stems from the fact that efficient SHG of the quadrupolar type from isotropic media has been reported previously for crossed polarizations [157]. The total external field is

$$\boldsymbol{E}^{\text{ext}}(t) = E_1 e^{-i\omega_1 t}\hat{\boldsymbol{x}} + E_2 e^{-i\omega_2 t}\hat{\boldsymbol{y}} + c.c., \tag{4.1}$$

where E_1 and E_2 are the constant complex amplitudes of the two fields polarized along $\hat{\boldsymbol{x}}$ and $\hat{\boldsymbol{y}}$ directions oscillating with frequencies ω_1 and ω_2 respectively. Following the perturbative approach introduced in the previous chapter and choosing the trial solution Eqs. (3.11) and (3.12), we solve the Laplace's equation independently for both frequencies to obtain the corresponding self consistent

linear scalar potentials. The external potentials are $\phi_1^{\rm ext} = -E_1 r\cos\theta$ and $\phi_2^{\rm ext} = -E_2 r\sin\theta$. The boundary conditions obeyed by the fields at the interface of the cylinder are identical to Eqs. (3.8) and (3.9) with a set for each of the incident fields. We evaluate the self consistent linear potential for fields oscillating at frequency ω_1 and ω_2 to linear order in the deformation ξ and obtain

$$\frac{\phi_1^{\rm out}}{E_1} = -r\cos\theta - \frac{1-\epsilon_1}{1+\epsilon_1}\frac{r_0^2}{r}\cos\theta + \xi\left[\left(\frac{1-\epsilon_1}{1+\epsilon_1}\right)^2\frac{r_0^3}{r^2}\cos 2\theta - \frac{1-\epsilon_1}{1+\epsilon_1}\frac{r_0^5}{r^4}\cos 4\theta\right], \tag{4.2a}$$

$$\frac{\phi_1^{\rm in}}{E_1} = -\frac{2}{1+\epsilon_1}r\cos\theta + 2\xi\frac{1-\epsilon_1}{(1+\epsilon_1)^2}\frac{r^2}{r_0}\cos 2\theta, \tag{4.2b}$$

$$\frac{\phi_2^{\rm out}}{E_2} = -r\sin\theta - \frac{1-\epsilon_2}{1+\epsilon_2}\frac{r_0^2}{r}\sin\theta - \xi\left[\left(\frac{1-\epsilon_2}{1+\epsilon_2}\right)^2\frac{r_0^3}{r^2}\sin 2\theta + \frac{1-\epsilon_2}{1+\epsilon_2}\frac{r_0^5}{r^4}\sin 4\theta\right], \tag{4.2c}$$

$$\frac{\phi_2^{\rm in}}{E_2} = -\frac{2}{1+\epsilon_2}r\sin\theta - 2\xi\frac{1-\epsilon_2}{(1+\epsilon_2)^2}\frac{r^2}{r_0}\sin 2\theta, \tag{4.2d}$$

where $\epsilon_g \equiv \epsilon(\omega_g)$ is the dielectric permittivity at the frequencies ω_g, $g = 1, 2$. Throughout this chapter we will employ the abbreviated notation, $f_g \equiv f(\omega_g)$, for any function f dependent on frequency. We must remark that in an experimental setup, the system would not be excited by homogeneous fields, but monochromatic laser beams. This, however, would not invalidate our calculations as we concentrate our attention on the fields not far from the wire, and we restrict ourselves to the long wavelength approximation.

Using the potentials [Eq. (4.2)], we can evaluate the linear self-consistent fields $\boldsymbol{E}_g = -\nabla\phi_g$,

$$\begin{aligned}\boldsymbol{E}_1^{\rm in} = -\nabla\phi_1^{\rm in} = &\left\{\frac{2E_1}{(\epsilon_1+1)}\cos\theta - 4E_1\xi\frac{(1-\epsilon_1}{(1+\epsilon_1)^2}\frac{r}{r_0}\cos 2\theta\right\}\hat{r}\\ &+\left\{-\frac{2E_1}{(\epsilon_1+1)}\sin\theta + 4E_1\xi\frac{(1-\epsilon_1)}{(1+\epsilon_1)^2}\frac{r}{r_0}\sin 2\theta\right\}\hat{\theta},\end{aligned} \tag{4.3}$$

$$\begin{aligned}\boldsymbol{E}_2^{\rm in} = -\nabla\phi_2^{\rm in} = &\left\{\frac{2E_2}{(\epsilon_2+1)}\sin\theta + 4E_2\xi\frac{(1-\epsilon_2}{(1+\epsilon_2)^2}\frac{r}{r_0}\sin 2\theta\right\}\hat{r}\\ &+\left\{\frac{2E_2}{(\epsilon_2+1)}\cos\theta + 4E_2\xi\frac{(1-\epsilon_2)}{(1+\epsilon_2)^2}\frac{r}{r_0}\cos 2\theta\right\}\hat{\theta}.\end{aligned} \tag{4.4}$$

The spatial variations of the linear self-consistent fields [Eqs. (4.3) and (4.4)] induce a macroscopic nonlinear polarization within the bulk of the cylinder given by

$$\boldsymbol{P}_- = n\,\boldsymbol{p}_-^{(2)} - \frac{1}{2}n\,\nabla\cdot\boldsymbol{Q}_-^{(2)} + \frac{ic}{\omega_-}n\,\nabla\times\boldsymbol{\mu}_-^{(2)} \tag{4.5}$$

where the subscript $-$ signifies the macroscopic nonlinear polarization and the quadratic moments are evaluated at the DF frequency $\omega_- = \omega_1 - \omega_2$. Eq. (4.5) corresponds to Eq. (2.15) but with a position independent density n of polarizable entities within the homogeneous cylinder. The

quadratic electric dipole $\boldsymbol{p}_-^{(2)}$, quadrupole $\boldsymbol{Q}_-^{(2)}$, and magnetic dipole $\boldsymbol{\mu}_-^{(2)}$ moments induced in the cylinder are given by Eqs. (2.11), (2.12) and (2.14), yielding

$$\begin{aligned}\boldsymbol{P}_- =& \underbrace{-\frac{n}{e}\alpha_-\left[\alpha_1\left(\boldsymbol{E}_1.\nabla\right)\boldsymbol{E}_2^* + \alpha_2^*\left(\boldsymbol{E}_2^*.\nabla\right)\boldsymbol{E}_1\right]}_{\text{Electric dipolar term}} + \underbrace{\frac{n}{2e}\alpha_1\alpha_2^*\nabla\cdot\left(\boldsymbol{E_1}\boldsymbol{E_2^*} + \boldsymbol{E_2^*}\boldsymbol{E_1}\right)}_{\text{Electric quadrupolar term}} \\ &+ \underbrace{\frac{n}{2e}\alpha_1\alpha_2^*\left(\frac{\omega_1+\omega_2}{\omega_-}\right)\nabla\times\left(\boldsymbol{E_1}\times\boldsymbol{E_2^*}\right)}_{\text{Magnetic dipolar term}},\end{aligned} \tag{4.6}$$

The induced fields from Eqs. (4.3) and (4.4) are then substituted in Eq. (4.6) to obtain the nonlinear bulk nonlinear polarization induced in the cylinder. To calculate the electric quadrupolar term, the vector identity $\nabla\cdot(\boldsymbol{AB}) = (\nabla\cdot\boldsymbol{A})\boldsymbol{B} + (\boldsymbol{A}\cdot\nabla)\boldsymbol{B}$ is used. Note that $\nabla\cdot\boldsymbol{E}_1$ and $\nabla\cdot\boldsymbol{E}_2$ are zero as there are no external charges. Thus, we get,

$$\begin{aligned}\boldsymbol{P}_- =& \frac{E_1E_2^*\xi}{2\pi^2 ner_0}\frac{(1-\epsilon_1)(1-\epsilon_2^*)}{(1+\epsilon_1)^2(1+\epsilon_2^*)^2}\Bigg[-(1-\epsilon_-)(2+\epsilon_1+\epsilon_2^*)+(1-\epsilon_1\epsilon_2^*) \\ &+\left(\frac{\omega_1+\omega_2}{\omega_-}\right)(\epsilon_2^*-\epsilon_1)\Bigg]\left\{\sin\theta\,\hat{r}+\cos\theta\,\hat{\theta}\right\}.\end{aligned} \tag{4.7}$$

The spatial variations in the nonlinear bulk polarization induces a bulk nonlinear charge within the cylinder, given by

$$\rho_-^{\text{nl}} = -\nabla\cdot\boldsymbol{P}_-. \tag{4.8}$$

Up to linear order in the deformation parameter, ξ, this is equal to zero. The termination of the bulk polarization at the surface of the cylinder induces a *bulk originated* surface nonlinear charge, $\sigma_-^b = \boldsymbol{P}_-\cdot\hat{\boldsymbol{n}}$ where $\hat{\boldsymbol{n}}$ is the unit normal to the surface pointing outwards given by Eq. (3.10). Substituting Eq. (4.7) we obtain

$$\begin{aligned}\sigma_-^b =& \frac{E_1E_2^*\xi}{2\pi^2 ner_0}\frac{(1-\epsilon_1)(1-\epsilon_2^*)}{(1+\epsilon_1)^2(1+\epsilon_2^*)^2}\Bigg[-(1-\epsilon_-)(2+\epsilon_1+\epsilon_2^*)+(1-\epsilon_1\epsilon_2^*) \\ &+\left(\frac{\omega_1+\omega_2}{\omega_-}\right)(\epsilon_2^*-\epsilon_1)\Bigg]\sin\theta.\end{aligned} \tag{4.9}$$

We now turn our attention towards the surface of the cylinder and calculate its nonlinear surface polarization. The expressions for the normal and tangential component of the nonlinear surface DF polarization are given by Eqs. (2.23) and (2.28). Both of these expressions were however written down for a semi-infinite surface lying at $z = 0$ with the positive $\hat{\boldsymbol{z}}$ direction pointing out of the material. In order to apply it for the curved cylindrical surface, we assume the thickness of the selvedge to be much smaller than the nominal radius r_0 of the cylinder. This permits us to assume, as in Chapter 3, that the surface is locally flat so the results of the dipolium model described in

Sec. 2.2 become applicable. We also assume a local Cartesian system on the surface with $\perp$ pointing along the outwards pointing normal $\parallel$ as the direction tangential to the surface. The components of the nonlinear surface polarization induced at each point on the surface can then be written as, $P_i^s = \chi_{ijk}^s F_j F_k$ where χ_{ijk}^s are the components of the local nonlinear surface susceptibility and $\boldsymbol{F}$ is made up of the normal projection of the displacement field and the parallel projection of the electric field evaluated at the surface $r_s(\theta)$,

$$\boldsymbol{F}_g(r_s) = \boldsymbol{E}_g(r_s^+) = \epsilon_g \boldsymbol{E}_g^{\perp}(r_s^-) + \boldsymbol{E}_g^{\parallel}(r_s^-), \tag{4.10}$$

Notice that the fields $\boldsymbol{F}_g$ for $g = 1, 2$ are continuous across the surface. Thus, rotating Eq. (2.23) to the local frame and substituting Eq. (2.24) we find the normal component of the nonlinear surface polarization,

$$P_{-,\perp}^s = \frac{(1-\epsilon_1)(1-\epsilon_2^*)}{64\pi^2 ne}\left[aE_{1,\perp}E_{2,\perp}^* + fE_{1,\parallel}E_{2,\parallel}^*\right], \tag{4.11}$$

where the parameter a is given by Eq. (2.25) and f=0. Following a similar approach but using Eqs. (2.28) to (2.30) and (4.10) we can find the tangential component of the nonlinear surface polarization. We get,

$$P_{-,\parallel}^s = \frac{(1-\epsilon_1)(1-\epsilon_2^*)}{64\pi^2 ne} 2b\left[\frac{\omega_1}{\omega_-}E_{1,\parallel}E_{2,\perp}^* - \frac{\omega_2}{\omega_-}E_{1,\perp}E_{2,\parallel}^*\right], \tag{4.12}$$

with $b = -1$. Using the fields Eqs. (4.3) and (4.4), the normal and tangential unit vectors Eqs. (3.10) and (3.24), Eq. (4.11) and Eq. (4.12) yield

$$\begin{aligned} P_{-,\perp}^s =& \frac{E_1 E_2^*}{64\pi^2 ne}\frac{(1-\epsilon_1)(1-\epsilon_2^*)}{(1+\epsilon_1)(1+\epsilon_2^*)}\Bigg[2(a-f)\sin 2\theta + 6\xi(a-f)(\sin\theta + \sin 5\theta) \\ &+8\xi(a-f)\sin 3\theta\left\{\frac{\epsilon_1 - \epsilon_2^*}{(1+\epsilon_1)(1+\epsilon_2^*)}\right\} + 8\xi(a+f)\sin\theta\left\{\frac{1-\epsilon_1\epsilon_2^*}{(1+\epsilon_1)(1+\epsilon_2^*)}\right\}\Bigg]. \end{aligned} \tag{4.13}$$

and

$$\begin{aligned} P_{-,\parallel}^s =& \frac{E_1 E_2^*}{32\pi^2 ne}\, b\, \frac{(1-\epsilon_1)(1-\epsilon_2^*)}{(1+\epsilon_1)(1+\epsilon_2^*)}\Bigg[-2\frac{\omega_1+\omega_2}{\omega_-} + 2\cos 2\theta + 6\xi(\cos 5\theta - \cos\theta) \\ &+8\xi\frac{\epsilon_2^* - \epsilon_1}{(1+\epsilon_1)(1+\epsilon_2^*)}\left\{\frac{\omega_1+\omega_2}{\omega_-}\cos\theta - \cos 3\theta\right\}\Bigg]. \end{aligned} \tag{4.14}$$

The spatial variations in the tangential component of the induced surface nonlinear polarization gives rise to a *surface originated* nonlinear surface charge $\sigma_-^s = -\nabla\cdot\boldsymbol{P}_{-,\parallel}^s$ given by

$$\begin{aligned} \sigma_-^s =& \frac{E_1 E_2^*}{32\pi^2 ner_0}\, b\, \frac{(1-\epsilon_1)(1-\epsilon_2^*)}{(1+\epsilon_1)(1+\epsilon_2^*)}\Bigg[4\sin 2\theta - 4\xi\sin\theta + 28\xi\sin 5\theta \\ &+8\xi\frac{\epsilon_2^* - \epsilon_1}{(1+\epsilon_1)(1+\epsilon_2^*)}\left\{\frac{\omega_1+\omega_2}{\omega_-}\sin\theta - 3\sin 3\theta\right\}\Bigg]. \end{aligned} \tag{4.15}$$

Now that we have calculated its external sources, we can calculate the DF field in a way similar to how we calculated the SH field Sec. 3.1. The screened DF scalar potential ϕ_- has $\rho_-^{\rm nl}=0$ as an *external bulk* source and the total nonlinear charges induced at the surface σ_-^b and σ_-^s as *external surface* sources, together with the normal component of the surface polarization $P^s_{-,\perp}$, all of which are accounted through the boundary conditions. The external sources have to be screened by the linear response ϵ_- of the particle at the DF frequency. Thus, we need to solve the following equation to obtain the quadratic self-consistent scalar potential,

$$\nabla^2\phi_- = \begin{cases} 0, & \text{(outside)} \\ -4\pi\rho^{\rm nl}/\epsilon_- = 0, & \text{(inside)} \end{cases} \tag{4.16}$$

subjected to the boundary conditions

$$\phi_-(r_s^+) - \phi_-(r_s^-) = 4\pi P^s_{-,\perp}, \tag{4.17}$$

and

$$\hat{\boldsymbol{n}}\cdot\nabla\phi_-(r_s^+) - \epsilon_-\hat{\boldsymbol{n}}\cdot\nabla\phi_-(r_s^-) = -4\pi(\sigma_-^b+\sigma_-^s). \tag{4.18}$$

Eq. (4.17) is the discontinuity of the scalar potential due to the presence of the normal nonlinear surface polarization $P^s_{-,\perp}$ which is a dipole layer across the selvedge of the particle. Eq. (4.18) is the discontinuity of the normal component of the displacement field due to the presence of the nonlinear surface charge. We solve Eq. (4.16) perturbatively using Eqs. (3.11) and (3.12) to obtain the self-consistent scalar potential at the DF frequency with terms up to linear order in ξ. Outside the cylinder the DF self consistent scalar potential is

$$\begin{aligned}\frac{\phi_-^{\rm out}}{E_1E_2^*} =& \frac{\xi}{\pi ne}\frac{(1-\epsilon_1)(1-\epsilon_2^*)}{(1+\epsilon_1)(1+\epsilon_2^*)(1+\epsilon_-)}\Bigg[\frac{1}{(1+\epsilon_1)(1+\epsilon_2^*)}\Bigg\{-(1-\epsilon_-)(2+\epsilon_1+\epsilon_2^*)+(1-\epsilon_1\epsilon_2^*) \\ &+(\epsilon_2^*-\epsilon_1)\left(\frac{\omega_1+\omega_2}{\omega_-}\right)\Bigg\} - \frac{b}{2}\frac{1+3\epsilon_-}{1+\epsilon_-} + b\frac{\epsilon_2^*-\epsilon_1}{(1+\epsilon_1)(1+\epsilon_2^*)}\left(\frac{\omega_1+\omega_2}{\omega_-}\right) + \frac{\epsilon_-}{8}\frac{(3-\epsilon_-)(a-f)}{1+\epsilon_-} \\ &+\frac{\epsilon_-}{8}\left\{3(a-f)+\frac{4(a+f)(1-\epsilon_1\epsilon_2^*)}{(1+\epsilon_1)(1+\epsilon_2^*)}\right\}\Bigg]\frac{r_0}{r}\sin\theta \\ &+\frac{1}{8\pi ne}\frac{(1-\epsilon_1)(1-\epsilon_2^*)}{(1+\epsilon_1)(1+\epsilon_2^*)(1+\epsilon_-)}[\epsilon_-(a-f)+2b]\frac{r_0^2}{r^2}\sin 2\theta+\ldots.\end{aligned} \tag{4.19}$$

Now, we compare Eq. (4.19) with the general expression of the $2D$ scalar potential

$$\phi^{\rm out} = 2p_y\frac{\sin\theta}{r} + Q_{xy}\frac{\sin 2\theta}{r^2}+\ldots. \tag{4.20}$$

to obtain the DF dipole and quadrupole moment per unit length from the θ dependence of the potential. The quadratic dipole p_y contributes only for a non-zero deformation ξ while the quadrupolar response Q_{xy} is independent of ξ, i.e. it would exist for a circular cylinder. We must point out the difference with Eq. (3.30) which was written for the case when the external field was polarized only

along the $\hat{\boldsymbol{x}}$ direction. Using Eq. (4.20) and the definitions given by Eqs. (3.2) and (3.4) we write the DF moments, p_y and Q_{xy}, as

$$p_y = [\gamma^d_{-,yxy}(\omega_1,\overline{\omega}_2) + \gamma^d_{-,yyx}(\overline{\omega}_2,\omega_1)]E_{1,x}E^*_{2,y} = \gamma^d_-(\omega_1,\overline{\omega}_2)E_{1,x}E^*_{2,y}, \tag{4.21}$$

$$Q_{xy} = [\gamma^Q_{-,xyxy}(\omega_1,\overline{\omega}_2) + \gamma^Q_{-,xyyx}(\overline{\omega}_2,\omega_1)]E_{1,x}E^*_{2,y} = \gamma^Q_-(\omega_1,\overline{\omega}_2)E_{1,x}E^*_{2,y}. \tag{4.22}$$

We define for the dipolar hyperpolarizability

$$\gamma^d_-(\omega_1,\overline{\omega}_2) = \gamma^d_{-,yxy}(\omega_1,\overline{\omega}_2) + \gamma^d_{-,yyx}(\overline{\omega}_2,\omega_1) = 2\gamma^d_{-,yxy}(\omega_1,\overline{\omega}_2) = 2\gamma^d_{-,yyx}(\overline{\omega}_2,\omega_1) \tag{4.23}$$

where we used the relation $\gamma^d_{-,yxy}(\omega_1,\overline{\omega}_2) = \gamma^d_{-,yyx}(\overline{\omega}_2,\omega_1)$ between the components. Similarly, for the quadrupolar hyperpolarizability

$$\gamma^Q_-(\omega_1,\overline{\omega}_2) = \gamma^Q_{-,xyxy}(\omega_1,\overline{\omega}_2) + \gamma^Q_{-,xyyx}(\overline{\omega}_2,\omega_1) = 2\gamma^Q_{-,xyxy}(\omega_1,\overline{\omega}_2) = 2\gamma^Q_{-,xyyx}(\overline{\omega}_2,\omega_1) \tag{4.24}$$

with $\gamma^Q_{-,xyxy}(\omega_1,\overline{\omega}_2) = \gamma^Q_{-,xyyx}(\overline{\omega}_2,\omega_1)$ relating the different components. The equality among the components of the hyperpolarizabilities is due to their intrinsic permutation symmetry which states that an interchange of the last two Cartesian indices along with the input frequencies leaves the component unchanged. Comparing Eqs. (4.21) and (4.22) with Eqs. (4.19) and (4.20), we identify the DF response tensors. The dipolar hyperpolarizability is

$$\begin{aligned}\gamma^d_-(\omega_1,\overline{\omega}_2) = \frac{\xi r_0}{2\pi ne}\frac{(1-\epsilon_1)(1-\epsilon_2^*)}{(1+\epsilon_1)(1+\epsilon_2^*)(1+\epsilon_-)}\Bigg[\frac{1}{(1+\epsilon_1)(1+\epsilon_2^*)}\Bigg\{-(1-\epsilon_-)(2+\epsilon_1+\epsilon_2^*)+(1-\epsilon_1\epsilon_2^*)\\ +(\epsilon_2^*-\epsilon_1)\left(\frac{\omega_1+\omega_2}{\omega_-}\right)\Bigg\}-\frac{b}{2}\frac{1+3\epsilon_-}{1+\epsilon_-}+b\frac{\epsilon_2^*-\epsilon_1}{(1+\epsilon_1)(1+\epsilon_2^*)}\left(\frac{\omega_1+\omega_2}{\omega_-}\right)+\frac{\epsilon_-}{8}\frac{(3-\epsilon_-)(a-f)}{1+\epsilon_-}\\ +\frac{\epsilon_-}{8}\Bigg\{3(a-f)+\frac{4(a+f)(1-\epsilon_1\epsilon_2^*)}{(1+\epsilon_1)(1+\epsilon_2^*)}\Bigg\}\Bigg],\end{aligned} \tag{4.25}$$

and the quadrupolar hyperpolarizability is

$$\gamma^Q_-(\omega_1,\overline{\omega}_2) = \frac{r_0^2}{8\pi ne}\frac{(1-\epsilon_1)(1-\epsilon_2^*)}{(1+\epsilon_1)(1+\epsilon_2^*)(1+\epsilon_-)}[\epsilon_-(a-f)+2b]. \tag{4.26}$$

The SF, $\omega_+ = \omega_1+\omega_2$, hyperpolarizability of the infinite cylinder can be easily extracted from Eqs. (4.25) and (4.26) by substituting $\omega_2 \leftarrow -\omega_2$, ϵ_- by ϵ_+, and taking the complex conjugate of the permittivity $\epsilon_2 \leftarrow \epsilon_2^*$. The dipolar SF hyperpolarizability is,

$$\begin{aligned}\gamma^d_+(\omega_1,\omega_2) = \frac{\xi r_0}{2\pi ne}\frac{(1-\epsilon_1)(1-\epsilon_2)}{(1+\epsilon_1)(1+\epsilon_2)(1+\epsilon_+)}\Bigg[\frac{1}{(1+\epsilon_1)(1+\epsilon_2)}\Bigg\{-(1-\epsilon_+)(2+\epsilon_1+\epsilon_2)+(1-\epsilon_1\epsilon_2)\\ +(\epsilon_2-\epsilon_1)\left(\frac{\omega_1-\omega_2}{\omega_+}\right)\Bigg\}-\frac{b}{2}\frac{1+3\epsilon_+}{1+\epsilon_+}+b\frac{\epsilon_2-\epsilon_1}{(1+\epsilon_1)(1+\epsilon_2)}\left(\frac{\omega_1-\omega_2}{\omega_+}\right)+\frac{\epsilon_+}{8}\frac{(3-\epsilon_+)(a-f)}{1+\epsilon_+}\\ +\frac{\epsilon_+}{8}\Bigg\{3(a-f)+\frac{4(a+f)(1-\epsilon_1\epsilon_2)}{(1+\epsilon_1)(1+\epsilon_2)}\Bigg\}\Bigg],\end{aligned} \tag{4.27}$$

and the quadrupolar SF hyperpolarizability is

$$\gamma_{+}^{Q}(\omega_1,\omega_2)=\frac{r_0^2}{8\pi ne}\frac{(1-\epsilon_1)(1-\epsilon_2)}{(1+\epsilon_1)(1+\epsilon_2)(1+\epsilon_+)}[\epsilon_+(a-f)+2b]. \tag{4.28}$$

The degenerate SH case can be obtained from Eqs. (4.27) and (4.28) when the input frequencies are equal, i.e. $\omega_2=\omega_1$. We verified that using this condition in the expressions for the SF dipolar and quadrupolar hyperpolarizabilities we do obtain the SH response tensor given by Eqs. (3.31) and (3.32).

4.2 SF/DF efficiency

We now focus towards the calculation of the electromagnetic fields in the radiation zone and the efficiency of DFG/SFG from the nanowire. The DF/SF electric and magnetic fields in the radiation zone can be calculated from Eqs. (3.47) and (3.48) by substituting the nonlinear dipole and quadrupolar moments given by Eqs. (3.2) and (3.4) and using the DF/SF dipolar and quadrupolar hyperpolarizabilities given by Eq. (4.25) or Eq. (4.27) and Eq. (4.26) or Eq. (4.28) respectively. Substituting these DF/SF fields in Eq. (3.49), the angular distribution of the DF/SF power per unit length can be calculated. We obtain,

$$\frac{d\mathcal{P}_{\pm}}{d\theta}=ck_{\pm}^3(E_1E_2^*)^2\left[|\gamma_{\pm}^{d}|^2\cos^2\theta+\frac{k_{\pm}^2}{16}|\gamma_{\pm}^{Q}|^2\cos^2 2\theta-\frac{k_{\pm}}{2}\,\mathrm{Im}(\gamma_{\pm}^{d}\gamma_{\pm}^{Q*})\cos\theta\cos 2\theta\right], \tag{4.29}$$

where $k_{\pm}$ is the wave number at the SF $(+)$ or DF $(-)$ frequency. Integrating Eq. (4.29), the total DF/SF power radiated per unit length from the nanowire is,

$$\mathcal{P}_{\pm}=\pi ck_{\pm}^3(E_1E_2^*)^2\left[|\gamma_{\pm}^{d}|^2+\frac{k_{\pm}^2}{16}|\gamma_{\pm}^{Q}|^2\right]. \tag{4.30}$$

The efficiency of the SFG/DFG process from the nanowire is defined by

$$\mathcal{R}_{\pm}=\frac{\mathcal{P}_{\pm}}{I_1I_2}, \tag{4.31}$$

where I_g $(g=1,2)$ is the intensity of the incident radiation given by $I_g=(c/2\pi)|E_g|^2$.

Substituting the relation for the intensities of illumination and Eq. (4.29) in Eq. (4.31) we get

$$\mathcal{R}_{\pm}=\frac{\pi^3}{1024}\frac{k_{\pm}^3}{c}\left[|\gamma_{\pm}^{d}|^2+\frac{k_{\pm}^2}{16}|\gamma_{\pm}^{Q}|^2\right]. \tag{4.32}$$

4.3 Results and discussions

Fig. 4.1 illustrates the absolute value of the dipolar γ^d (top panels) and the quadrupolar γ^Q (bottom panels) hyperpolarizabilities, given by Eqs. (4.25) to (4.28) respectively, for a deformed cylinder made up of an insulator with its dielectric permittivity given by Eq. (2.26). We choose the relation between the frequencies of the longitudinal and transverse modes to be $\omega_{\rm L} = \sqrt{2}\,\omega_{\rm T}$ and the lifetime parameter $\tau = 20/\omega_{\rm T}$. These are the same material parameters that were employed to illustrate the normal component of the DF response of a planar dielectric surface through the dimensionless function $a(\omega_1, \overline{\omega}_2)$ in Fig. 2.3 given by Eq. (2.25). We allow both the input frequencies to vary between negative and positive values to demonstrate all of the three wave mixing processes, namely, SFG, DFG, SHG, OR and their complex conjugates, by identifying $\gamma^d(\omega_1, \omega_2) = \gamma^d_+(\omega_1, \omega_2)$ when both frequencies are positive, $\gamma^d(\omega_1, \omega_2) = \gamma^d_-(\omega_1, -\omega_2)$ when $\omega_1 > 0$ and $\omega_2 < 0$, $\gamma^d(\omega_1, \omega_2) = (\gamma^d(-\omega_1, -\omega_2))^*$ for the other cases, with similar relations for γ^Q. We show low resolution $3D$ surface plots (left panels) to illustrate the nature of peaks and also the more accurate $2D$ color maps (right panels) with higher resolution to display the normalized values. Both γ^d and γ^Q show strong resonant ridges when either input frequency, positive or negative, is equal to the frequency at which the surface plasmon polariton (SPP) is excited, $\omega_{\rm spp} = \sqrt{3/2}\,\omega_{\rm T}$. The intense diagonal ridges in the first and third quadrants of the figures occur when the sum of the two incident frequencies resonates with the SPP. There are further peaks when two ridges meet, for which both the resonant conditions are fulfilled jointly. The first quadrant is associated with the SFG process, the fourth with the DFG process; the third and the second quadrants, respectively, replicate these processes as the overall sign of the incident frequencies are inverted. The large peak observed in the fourth quadrant corresponds to the particular case of DFG where both the incident frequencies are simultaneously SPP resonant. The response along the diagonal $\omega_1 = \omega_2$ corresponds to the SH process. Notice that in this case we cross a diagonal ridge when the fundamental frequency is the subharmonic of the SPP resonance and meet a peak when the fundamental reaches the resonance condition. To enumerate, the main peaks of the response functions are located at the following positions: larger ones at ($\omega_1 = \omega_{spp}$, $\omega_2 = 0$) and ($\omega_1 = \omega_{spp}$, $\omega_2 = -\omega_{spp}$), and smaller peak at ($\omega_1 = \omega_2 = \omega_{spp}$), at the permutations of the input frequencies, and an overall change of sign. Both contributions, dipolar and quadrupolar, illustrate that the DF response is much stronger than the SF response and of similar order to the SH response. The horizontal, vertical, and diagonal ridges are much weaker than the main peaks for the quadrupolar response as compared to the dipolar case. We have also explored the absolute values of γ^d and γ^Q for two different lifetime parameters, namely, $\tau = 50/\omega_{\rm T}$ and $\tau = 100/\omega_{\rm T}$. As expected, we obtain a similar structure but the peaks and ridges become narrower and sharper with increasing lifetimes. In Fig. 4.2, we show a closeup of the map of γ^d in a region around the peak at $\omega_1 = -\omega_2 = \omega_{spp}$, corresponding to DFG process with a small difference frequency. Notice that when the two input frequencies are exactly equal and opposite, i.e. zero DF frequency, the second order response is about an order of magnitude lower than the neighboring points, when $\delta\omega \to 0$. Thus, the response of the system for OR is smaller than the DF

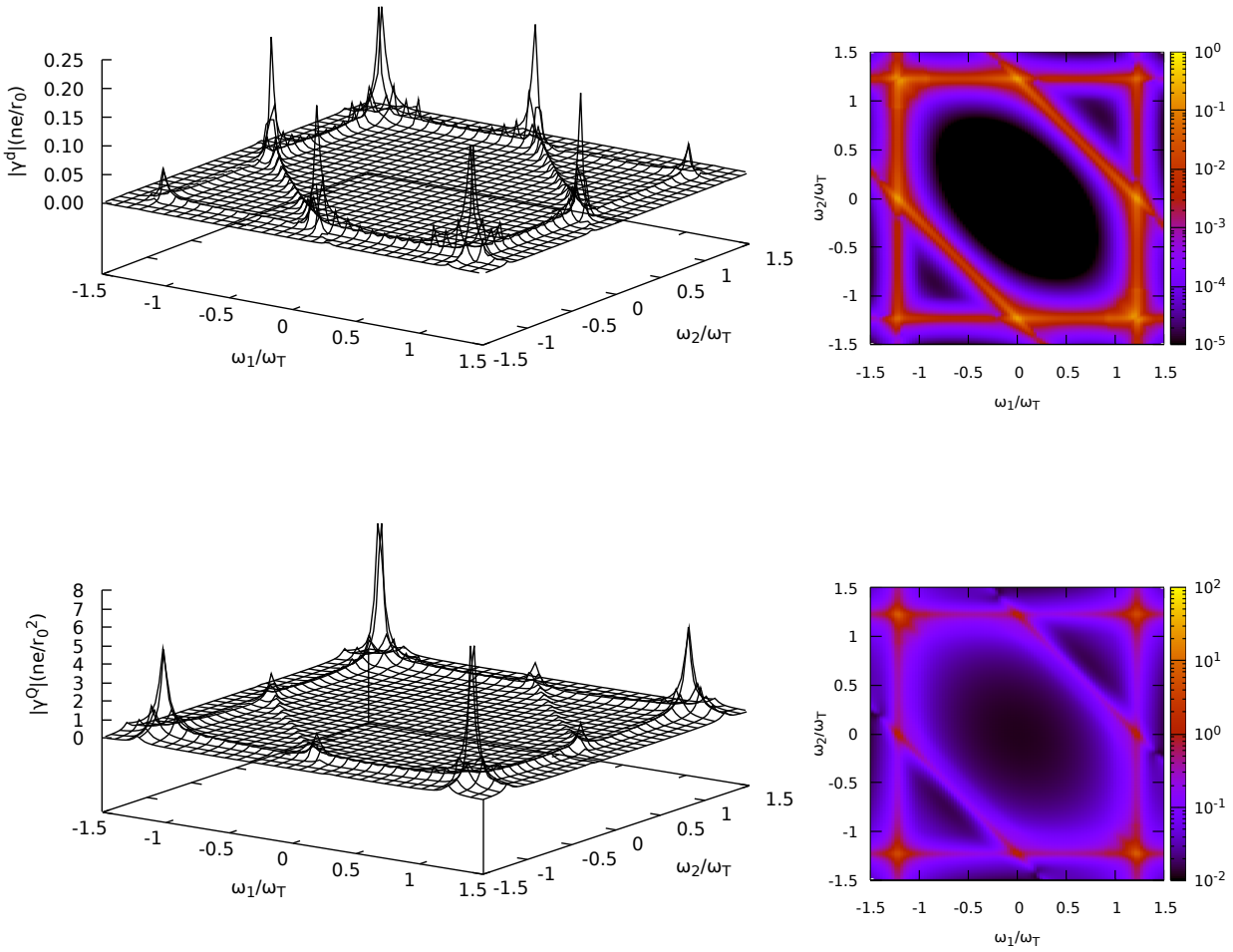

Figure 4.1: Normalized absolute value of the dipolar γ^d (top panels) and the quadrupolar (bottom panels) γ^Q hyperpolarizabilities for an infinitely long dielectric cylinder whose permittivity is given by Eq. (2.26) as a function of the normalized incident frequency $\omega_g/\omega_\mathrm{T}$ for $g = 1, 2$. The relation between the longitudinal and the transverse optical mode frequencies is $\omega_\mathrm{L} = \sqrt{2}\,\omega_\mathrm{T}$ and the lifetime parameter is $\tau = 20/\omega_\mathrm{T}$. The deformation is equal to $\xi = 0.01$. $3D$ surface plots (low resolution) of both are displayed in the left panels and the respective $2D$ color maps (high resolution) in the right panels. The regions where both frequencies have the same signs correspond to SFG and those with opposite signs to DFG.

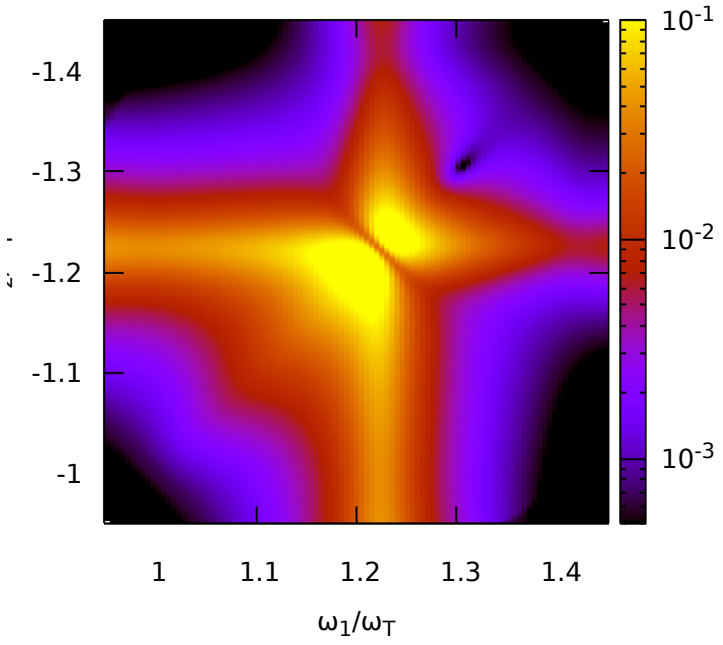

Figure 4.2: High resolution $2D$ color map of the normalized dipolar hyperpolarizability $|\gamma^d|$, shown in Fig. 4.1, close to the resonance around the region $\omega_1 \approx \omega_2 \approx \omega_{spp}$, with ω_2 negative.

response. No such structure was observed for the quadrupolar hyperpolarizability.

In Fig. 4.3, the absolute value of the dipolar γ^d (top panels) and the quadrupolar γ^Q (bottom panels) hyperpolarizabilities, given by Eqs. (4.25) to (4.28) respectively, for a deformed metallic cylinder with a Drude type permittivity given by Eq. (3.51) is plotted. Both low resolution $3D$ surface plots (left panels) and higher resolution $2D$ color maps (right panels) are shown. Similar to the dielectric case, both hyperpolarizabilities exhibit strong peaks when the surface plasmon (SP), $\omega_{\rm sp} = \sqrt{1/2}\,\omega_{\rm p}$, is excited at either or both the input frequencies or at the sum frequency. The dielectric permittivity of the metal has a pole at zero frequency resulting in a singularity demonstrated by a sharp peak when both input frequencies are zero. The diagonal ridges in the first and third quadrants represent the resonance in the SF response when the surface plasmon is excited at the sum frequency. When both input frequencies are equal to the SP resonance frequency, a peak corresponding to the SH response is observed. The fourth quadrant (ω_1 positive and ω_2 negative) corresponds to the DF response and exhibits a resonance, smaller than for the SH response, when both the frequencies are equal to $\omega_{\rm sp}$. As previously mentioned, the second and the third quadrants display the complex conjugates of the responses in the fourth and the first quadrants respectively. Similar to the dielectric case, horizontal and vertical ridges when either input frequency is SP resonant are also observed.

The efficiency of the DFG/SFG processes is given by Eq. (4.32), which we can write in the following

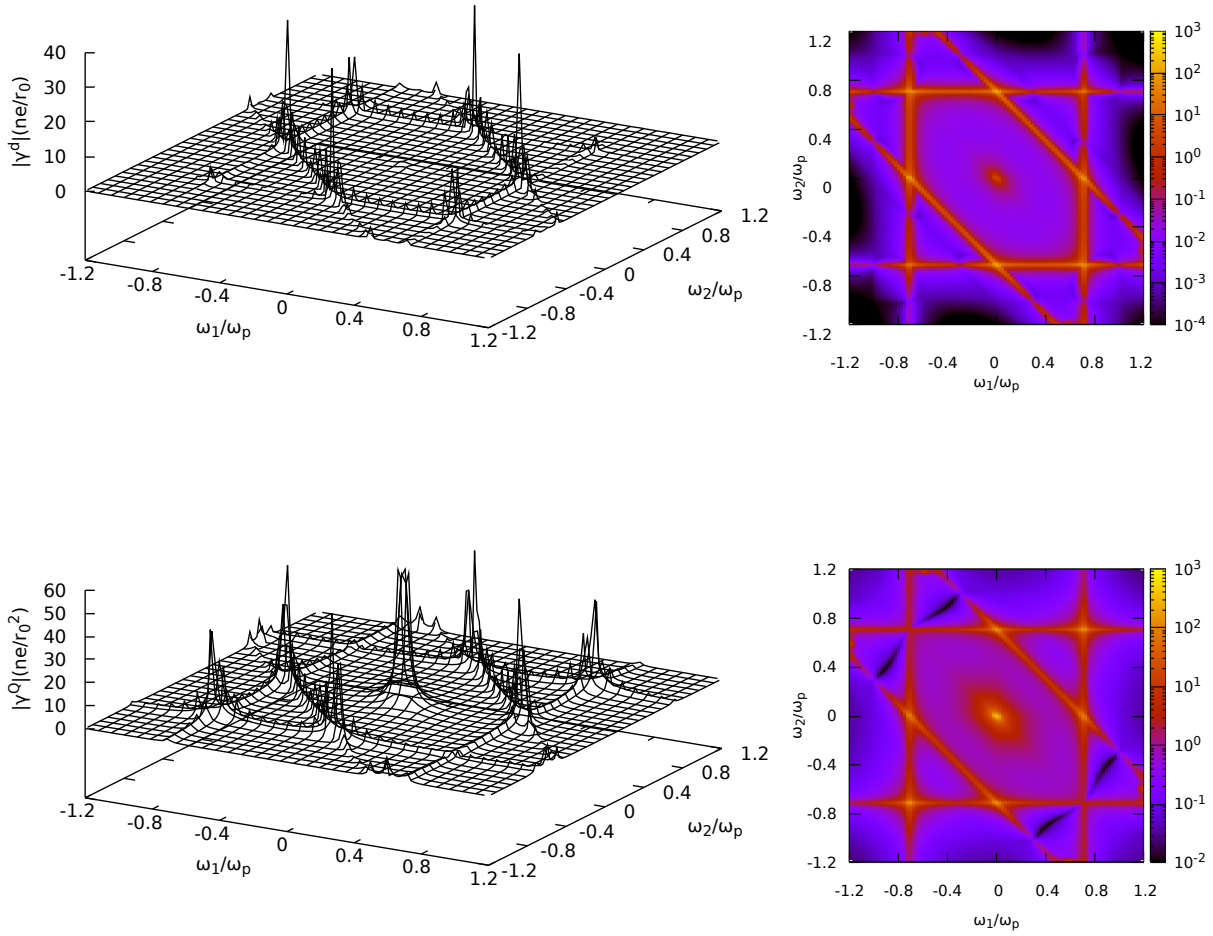

Figure 4.3: Normalized absolute value of the dipolar γ^d (top panels) and the quadrupolar (bottom panels) γ^Q hyperpolarizabilities for an infinitely long metallic cylinder whose permittivity is given by Eq. (3.51) as a function of the normalized incident frequency $\omega_g/\omega_\mathrm{p}$ for $g = 1, 2$ and the lifetime parameter is $\tau = 100/\omega_\mathrm{p}$. The deformation is equal to $\xi = 0.01$. $3D$ surface plots (low resolution) of both are displayed in the left panels and respective $2D$ color maps (high resolution) in the right panels.

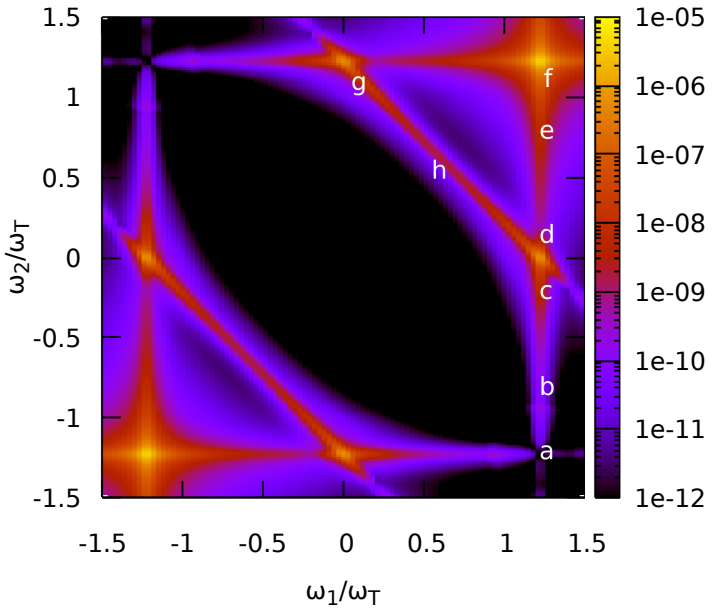

Figure 4.4: Normalized efficiency for the three wave mixing process for the same dielectric cylinder as in Fig. 4.1 as function of normalized input frequencies $\omega_g/\omega_{\mathrm{T}}$ for $g = 1, 2$ for deformation $\xi = 0.01$.

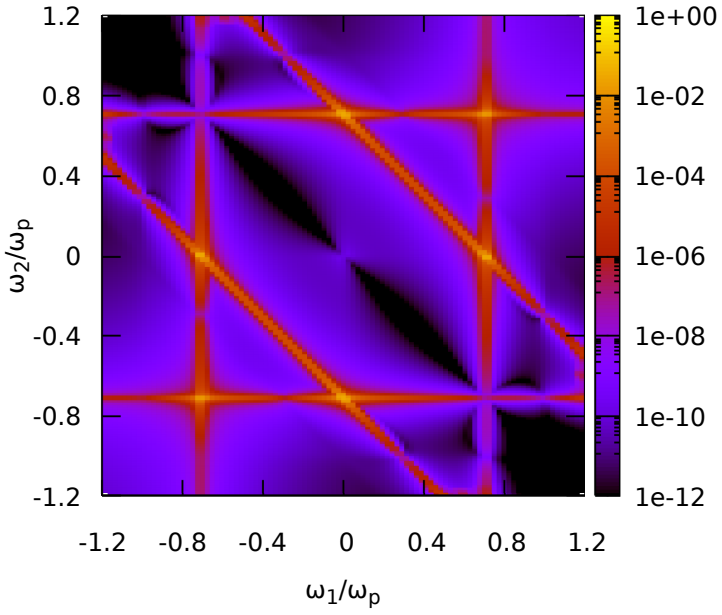

Figure 4.5: Normalized efficiency for the three wave mixing process for the same metallic cylinder as in Fig. 4.3 as function of normalized input frequencies $\omega_g/\omega_{\mathrm{p}}$ for $g = 1, 2$ for deformation $\xi = 0.01$.

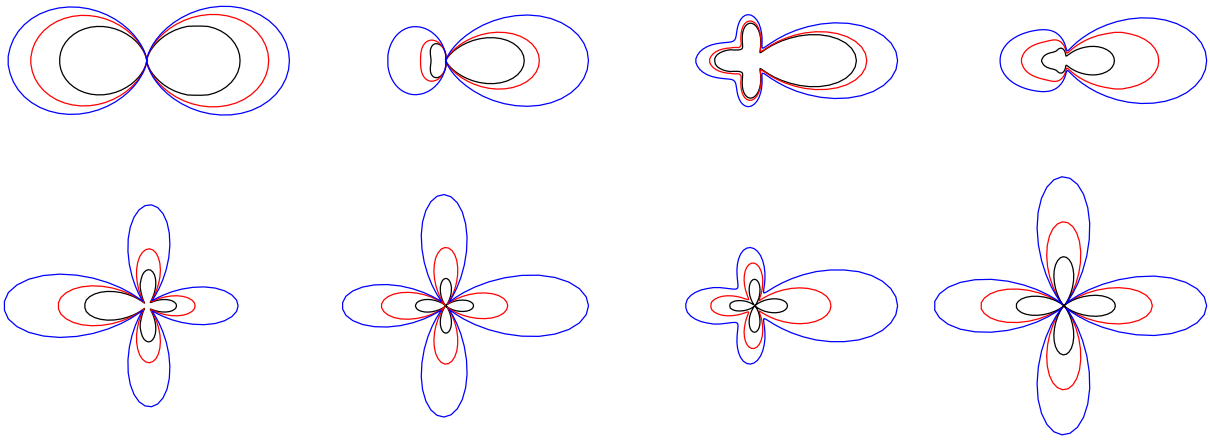

Figure 4.6: Normalized $2D$ angular radiation patterns for the same dielectric cylinder as in Fig. 4.4 for different input frequencies ω_1 and ω_2. Each set of pattern corresponds to the region around the points marked in Fig. 4.4; from left to right a-d (top row), and e-h (bottow row). For the patterns a-f we choose ω_1 at a constant value at the resonance with varying ω_2, i.e. we traverse along the vertical line at resonance. We choose both the input frequencies to vary along the diagonal resonance for regions g and h.

form,

$$\mathcal{R}_{\pm} = \frac{1}{cr_0}\frac{1}{(ne)^2}\mathcal{R}'_{\pm} \tag{4.33}$$

where $\mathcal{R}'_{\pm}$ is a dimensionless efficiency. We present the dimensionless efficiencies corresponding to the dielectric and metallic cylinders of Fig. 4.3 and Fig. 4.1 in Figs. 4.4 and 4.5 respectively. For the dielectric case, Fig. 4.4, the first quadrant illustrates the efficiency of the SFG process with a ridge along the diagonal where the sum of the two input frequencies is SPP resonant. The mid point of the diagonal corresponds to SH when the fundamental frequencies are the subharmonic of the SPP resonance. A peak is observed when both the fundamental frequencies are SPP resonant, associated with a SH process. The fourth quadrant, where ω_1 is positive and ω_2 negative, displays the efficiency of the DFG from the cylinder with a resonance in the region where both input frequencies are equal to ω_{spp}. The second and the third quadrants, as previously mentioned for the hyperpolarizabilities, denote complex conjugates of the processes in the fourth and the first quadrants respectively. Exactly similar horizontal, vertical, and diagonal ridges and peaks at the resonances of either or both input frequencies are observed for the metallic cylinder, shown in Fig. 4.5. Since, the dielectric permittivity of the metal has a singularity for $\omega = 0$, an additional resonance is observed when both the input frequencies are close to zero. Note, the SHG efficiency is much larger than the SFG or the DFG process for the dielectric cylinder, and of comparable magnitudes for the metallic case. Substantially large efficiency exhibited by both graphs corresponding to the DFG process with $\Delta\omega \to 0$ indicate a possible application towards the generation of THz radiation from the nanowire.

In Fig. 4.6, we plot the normalized $2D$ angular radiation pattern of the same dielectric cylinder as in Fig. 4.4 in the vicinity of resonances corresponding to the regions marked in Fig. 4.4. Even for a small deformation, $\xi = 0.01$, we observe strong competition between the dipolar and the quadrupolar contributions, with the dipolar response dominating over the quadrupolar response for certain frequencies. We also explored the radiation patterns, in the vicinity of resonances, for a metallic cylinder, identical to Fig. 4.5, and found the patterns to be completely dominated by the dipolar response; the effect of the quadrupolar contributions appearing only when farther from the resonance.

4.4 Conclusions

We extended our analytical perturbative formalism to study the SH response, introduced in Chapter 3, of an isolated infinitely long noncentrosymmetric cylinder to include all second order, particularly the SF and the DF, responses. We demonstrate our derivation by evaluating the approximate expressions for the DF response of the deformed isolated cylinder whose noncentrosymmetric cross-section displays three protuberances separated by an angle of 120° in the plane. Like the SH case, we performed our calculations in $2D$ given the translational symmetry along the axis of the cylinder, and we used the long wavelength limit by assuming the nominal radius of the cylinder to be much smaller than the wavelength of light. We employed our perturbative theory to obtain self consistent fields induced within and beyond the cylinder illuminated by two plane monochromatic waves polarized in the plane of the cross-section but perpendicular to each other up to linear order in the deformation parameter. We further employed the *dipolium* model, developed in Chapter 2, for the DF response to compute the bulk and surface contributions to the DF polarization. This DF polarization induces nonlinear charges in the bulk and on the surface of the cylinder. We again solve perturbatively for self-consistent DF fields from which we identify the DF dipolar and quadrupolar hyperpolarizability of the cylinder. As expected, we obtained the quadrupolar DF hyperpolarizability to be independent of the deformation and the dipolar hyperpolarizability to be linear dependent on it. Once the DF response is calculated, we reverted the sign of one of the input frequencies to obtain the SF response and fields, and then inserted the degeneracy condition for the two frequency to obtain the SH results of Chapter 3. The near SF/DF fields were then employed using the theory of electromagnetic radiation in $2D$, to obtain the SF/DF far-fields in the plane from which the angular power radiated, per unit length of the cylinder, in the plane is extracted. We finally computed the conversion efficiency of the SFG/DFG process.

We illustrated our results for the SF/DF hyperpolarizabilities and efficiencies of a metallic and a dielectric deformed cylinder. We plotted their spectral features, analyzed them, identified the frequency regions corresponding to the SF, DF, SH, and OR type response and their corresponding resonances. We observed resonances when either input frequency or both were close to the SPP or SP resonances of the dielectric or the metallic cylinder respectively. We noted efficient SFG and

SHG near the resonances for both systems. The resonant peaks in the region $\delta\omega \to 0$, corresponding to DF response, was found to be comparable to or of larger magnitude than the SH response. The nonlinear DF response for $\delta\omega \to 0$ with both input frequencies close to $\omega_{\rm spp}$ was found to be larger by an order of magnitude than the OR process ($\delta\omega = 0$). This predicts the possibility of the generation of radiation in the THz frequency gap form our system.

Thus, we have successfully developed an approximate analytical technique to explore any three-wave mixing process from our simple $2D$ noncentrosymmetric nanocylinders made up of centrosymmetric materials. As previously mentioned, the nonlinear responses estimated from our theory does not taking into account effects, similar to those ignored in the *dipolium* model, such as crystallinity, surface states and relaxation. Our calculation of the SF/DF response can be simply extended for incident waves polarized with any angles between them.

5

Numerical methods

Nonlinear optical properties of arrays of nanoparticles and metamaterials or metasurfaces designed by periodically arranging meta-atoms have been studied extensively by both experimental and numerical means [16, 24, 30, 33, 71, 158]. Diverse kinds of systems have been explored with various component materials or geometric configurations. Similar to bulk materials or single nanoparticles, metamaterials made up of centrosymmetric materials generate a dipole originated SH signal only at the interfaces between the inclusions and their host where the inversion symmetry is locally lost, though it can be globally restored if the geometry itself is centrosymmetric. Hence, for efficient nonlinear conversion to take place at metamaterials, it must have a noncentrosymmetric geometry. Otherwise, a multipolar originated signal may be produced, for example, when strongly focused beams with large field inhomogeneities are employed. Novel fabrication technique permit production of metamaterials with diverse geometrical configurations and hence SHG from metamaterials or metasurfaces constructed from centrosymmetric materials, with arbitrary geometry, have been explored. Different numerical techniques have been employed to study SHG from such nanostructures, such as the Surface Integral Equation (SIE) [33], Finite Differences in the Time Domain (FDTD) [16, 30, 159], Finite Element Method (FEM) [30], and others. The field enhancement at resonant plasmonic nanostructues and metamaterials offer some advantages for efficient SHG [24, 160], although it is somewhat hampered by dissipation. Recently, SHG from metasurfaces fabricated from high-refractive index dielectrics, supporting Mie resonances with low ohmic losses has been also explored [39, 161].

Here, we study the SH response of a binary metamaterial composed of an array of noncentrosymmetric nanowires made up of centrosymmetric materials. To that end, we take advantage of an efficient homogenization procedure [66] to calculate the macroscopic response of the nanostructured system. In this scheme, the macroscopic electromagnetic fields or the response of the artificial material is computed by averaging the microscopic fields, obtained through a solution of full-wave Maxwell's equations. Different theories have been reported over the years for homogenization methods to calculate the macroscopic fields and optical properties of nanostructures [162–164]. A program-

ming package, named *Photonic*, using the homogenization technique presented in ref. [66], has been developed by Mochán et. al [64]. The package is written in the programming language *Perl* and its extension *Perl-Data Language PDL* for scientific computing. The program implements the Haydock's recursive scheme [165] for efficient computation of the macroscopic response. Linear optical properties of $2D$ [166] and $3D$ [66] periodic arrays have been obtained using this package. In one work, Haydock's recursive scheme was employed to investigate from a macroscopic perspective the photonic bands of $2D$ photonic crystals made of a periodic arrays of holes in a dielectric medium [167]. It was later realized that the same Haydock scheme could also be employed to obtain the microscopic fields, and from them, the nonlinear response. Thus, the package has been complemented with modules to evaluate the microscopic linear fields, and the nonlinear polarization and SH response utilizing the *dipolium* [Sec. 2.2] model [124]. They have recently been used to calculate the second harmonic (SH) response of an array of cross shaped holes in a Ag matrix [71]. Recently, the package was also applied to study the linear optical response of multi-component nanostructures [70].

A detailed derivation of the homogenization scheme and the recursive Haydock's method employed to evaluate the macroscopic response of the system was presented in the doctoral thesis of Dr. Samuel Pérez [168]. We will not delve into the intricacies of the methodology here. However, for the sake of completeness, we briefly outline the technique in the subsequent sections. In the present work, we intend to compute the SH response of an array of bidimensional nanocylinders with noncentrosymmetric cross-section, as shown in Fig. 3.1, made up of a centrosymmetric material and to compare the results with those of the approximate analytical calculations of Chapter 3.

The chapter begins with an introduction to the homogenization scheme, Sec. 5.1, followed by a description of the Haydock's recursive methodology in Sec. 5.2 for the calculation of the macroscopic response and the microscopic linear fields. In Sec. 5.3 we compare the numerically computed fields to the analytical ones. We found some problems and limitations in the nonlinear modules of *Photonic*, which we describe in Sec. 5.4, together with a proposed solution and its implementation. Our primary results, the validation of our numerical results by a comparison between the numerical and the analytical SH susceptibility for dielectric systems are presented in Sec. 5.5. Finally, the conclusions of our work are presented Sec. 5.6.

5.1 Homogenization

We consider a binary periodic array formed of nanometer sized arbitrarily shaped inclusions embedded in a matrix. We divide the space into two regions; those occupied by the inclusions, denoted by b, and the rest of the space in the matrix, denoted by a. The space in the matrix can either be empty, i.e. vacuum, or a homogeneous material into which the inclusions are embedded. We assume that each inclusion is large enough to possess a well-defined macroscopic response, either

ϵ_a or ϵ_b, but much smaller than the free space wavelength of light so we can use a nonretarded approximation. The microscopic response of the system is given by

$$\begin{aligned}\epsilon(\boldsymbol{r}) &= \epsilon_a - \epsilon_{ab} B(\boldsymbol{r}) \\ &= \frac{\epsilon_a}{u}(u - B(\boldsymbol{r})),\end{aligned} \tag{5.1}$$

where $\epsilon_{ab} = \epsilon_a - \epsilon_b$ and we introduced the spectral variable $u = 1/(1 - \epsilon_b/\epsilon_a)$. $B(\boldsymbol{r})$ is the characteristic function for region b and takes the value 0 within a and 1 within b. The characteristic function is periodic, $B(\boldsymbol{r}) = B(\boldsymbol{r} + \boldsymbol{R})$, where $\{\boldsymbol{R}\}$ is the Bravais lattice of the periodic system. In the present work, we will designate such artificial periodic arrangement of two materials as a *metamaterial*.

The constitutive equation $\boldsymbol{D}(\boldsymbol{r}) = \epsilon(\boldsymbol{r})\boldsymbol{E}(\boldsymbol{r})$ is written in the reciprocal space for a Bloch's wave with Bloch's vector $\boldsymbol{q}$ as

$$\boldsymbol{D}_{\boldsymbol{G}}(\boldsymbol{q}) = \sum_{\boldsymbol{G}'} \epsilon_{\boldsymbol{G}\boldsymbol{G}'} \boldsymbol{E}_{\boldsymbol{G}'}(\boldsymbol{q}), \tag{5.2}$$

where $\{\boldsymbol{G}\}$ is the reciprocal lattice. $\boldsymbol{D}_{\boldsymbol{G}}$ and $\boldsymbol{E}_{\boldsymbol{G}}$ are the Fourier coefficients of the displacement $\boldsymbol{D}(\boldsymbol{r})$ and the electric $\boldsymbol{E}(\boldsymbol{r})$ fields respectively with wavevector $\boldsymbol{q} + \boldsymbol{G}$, and $\epsilon_{\boldsymbol{G}\boldsymbol{G}'}$ is the Fourier coefficient of $\epsilon(\boldsymbol{r})$ with wavevector $(\boldsymbol{G} - \boldsymbol{G}')$. We choose a longitudinal external field given by $\boldsymbol{E}^{\mathrm{ex}}(\boldsymbol{r}) = -\nabla\phi^{\mathrm{ex}}$ and neglect the effects of retardation within a unit cell. Thus, we take the electric field as longitudinal,

$$\boldsymbol{E} = \boldsymbol{E}^{\mathrm{L}}_{\boldsymbol{G}} = \hat{\boldsymbol{G}}\hat{\boldsymbol{G}} \cdot \boldsymbol{E}_{\boldsymbol{G}}, \tag{5.3}$$

where we have used the simplified notation $(\boldsymbol{q} + \boldsymbol{G})/|\boldsymbol{q} + \boldsymbol{G}| = \hat{\boldsymbol{G}}$. For all non-null $\boldsymbol{G}$'s, $q \ll G$ within the long-wavelength approximation, so that $\hat{\boldsymbol{G}} \approx \boldsymbol{G}/G$, while $\hat{\boldsymbol{0}} = \hat{\boldsymbol{q}}/q$. For longitudinal fields, $\nabla \times \boldsymbol{E}^{\mathrm{ex}} = \nabla \times \boldsymbol{D}^{\mathrm{L}} = 0$ and $\nabla \cdot \boldsymbol{E}^{\mathrm{ex}} = \nabla \cdot \boldsymbol{D}^{\mathrm{L}} = 4\pi\rho^{\mathrm{ex}}$; hence we identify $\boldsymbol{E}^{\mathrm{ex}}$ with $\boldsymbol{D}^{\mathrm{L}}$, which therefore has no spatial fluctuations originated in the texture of the metamaterial. From the constitutive equation we obtain $\boldsymbol{D}^{\mathrm{L}} = \epsilon^{\mathrm{LL}}\boldsymbol{E}^{\mathrm{L}}$ where ϵ^{LL} is the longitudinal projection of the dielectric response. After solving for the electric field in terms of the external field and averaging the result we obtain $\boldsymbol{E}^{\mathrm{L}}_{\mathrm{a}} = (\epsilon^{\mathrm{LL}})^{-1}_{\mathrm{aa}}\boldsymbol{D}^{\mathrm{L}}_{\mathrm{a}}$, where we denote with the subscript a the action of the *averaging projector* $\mathcal{P}_a$ which acts on a field by removing its short-lengthscale, large-wavevector spatial fluctuations. We identify the averaged fields with the macroscopic fields, $\boldsymbol{E}^{\mathrm{L}}_{\mathrm{a}} = \boldsymbol{E}^{\mathrm{L}}_{\mathrm{M}}$ and $\boldsymbol{D}^{\mathrm{L}}_{\mathrm{a}} = \boldsymbol{D}^{\mathrm{L}}_{\mathrm{M}}$; the superscript M denotes macroscopic. From the macroscopic constitutive equation $\boldsymbol{E}^{\mathrm{L}}_{\mathrm{M}} = (\boldsymbol{\epsilon}^{\mathrm{LL}}_{\mathrm{M}})^{-1}\boldsymbol{D}^{\mathrm{L}}_{\mathrm{M}}$ we identify the macroscopic linear response [169]

$$(\boldsymbol{\epsilon}^{\mathrm{LL}}_{\mathrm{M}})^{-1} = (\boldsymbol{\epsilon}^{\mathrm{LL}})^{-1}_{\mathrm{aa}}. \tag{5.4}$$

Hence, in the long-wavelength approximation, the inverse of the longitudinal projection of the macroscopic dielectric function is equal to the inverse of the longitudinal projection of the microscopic dielectric function averaged.

Going back to reciprocal space, we substitute Eq. (5.3) into Eq. (5.2) and take the longitudinal projection to find the electric field

$$\boldsymbol{E}^{\mathrm{L}}_{\boldsymbol{G}} = \hat{\boldsymbol{G}}\,[\hat{\boldsymbol{G}}\cdot(\epsilon_{\boldsymbol{G0}}\hat{\mathbf{0}})]^{-1}\hat{\mathbf{0}}\cdot\boldsymbol{D}^{\mathrm{L}}_{\mathbf{0}} = \hat{\boldsymbol{G}}\,\eta^{-1}_{\boldsymbol{G0}}\hat{\mathbf{0}}\cdot\boldsymbol{D}^{\mathrm{L}}_{\mathbf{0}}, \tag{5.5}$$

where we defined

$$\eta_{\boldsymbol{GG'}} = \hat{\boldsymbol{G}}\cdot(\epsilon_{\boldsymbol{GG'}}\hat{\boldsymbol{G}}'). \tag{5.6}$$

The macroscopic longitudinal field is obtained by spatially averaging the microscopic field, thus eliminating the small-scale spatial fluctuations from $\boldsymbol{E}^{\mathrm{L}}$; hence we identify the macroscopic fields with their $\boldsymbol{G}=0$ Fourier components, $\boldsymbol{E}^{\mathrm{L}}_{\mathrm{M}} = \boldsymbol{E}^{\mathrm{L}}_{0}$ and $\boldsymbol{D}^{\mathrm{L}}_{\mathrm{M}} = \boldsymbol{D}^{\mathrm{L}}_{0}$. Thus, Eq. (5.5) yields

$$\boldsymbol{E}^{\mathrm{L}}_{\mathrm{M}} = \hat{\boldsymbol{q}}\,\eta^{-1}_{\mathbf{00}}\hat{\boldsymbol{q}}\cdot\boldsymbol{D}^{\mathrm{L}}_{\mathrm{M}}, \tag{5.7}$$

from which we identify the macroscopic linear dielectric response given by

$$(\boldsymbol{\epsilon}^{\mathrm{LL}}_{\mathrm{M}})^{-1} = \hat{\boldsymbol{q}}\,\eta^{-1}_{\mathbf{00}}\hat{\boldsymbol{q}}. \tag{5.8}$$

The above result was first reported by Mochán et. al [169] where an elaborate derivation of the methodology can be found.

5.2 Haydock's Recursive Method

The macroscopic response [Eq. (5.8)] is computed efficiently by taking advantage of the Haydock's recursive scheme [165]. We begin by taking the Fourier transform of Eq. (5.1),

$$\epsilon_{\boldsymbol{GG'}} = \frac{\epsilon_a}{u}(u\delta_{\boldsymbol{GG'}} - B_{\boldsymbol{GG'}}), \tag{5.9}$$

where the characteristic function in reciprocal space is

$$B_{\boldsymbol{GG'}} \equiv B_{\boldsymbol{G-G'}} = \frac{1}{\Omega}\int_v d^3r e^{i(\boldsymbol{G-G'})\cdot\boldsymbol{r}}, \tag{5.10}$$

with v the region occupied by the inclusions inside the unit cell of volume Ω. Using Eq. (5.6) we may write

$$\eta^{-1}_{\boldsymbol{GG'}} = \frac{1}{\epsilon_{ab}}(u\delta_{\boldsymbol{GG'}} - B^{\mathrm{LL}}_{\boldsymbol{GG'}})^{-1} = \frac{1}{\epsilon_{ab}}\mathcal{G}_{\boldsymbol{GG'}} \tag{5.11}$$

where $\mathcal{G}_{\boldsymbol{GG'}}$ are the matrix elements of an operator $\mathcal{G} = (u - B^{LL})^{-1}$ which plays the role of a Green's operator, analogous to $(\mathcal{E}-\mathcal{H})^{-1}$ in ordinary quantum mechanics, with energy $\mathcal{E}$ and Hamiltonian $\mathcal{H}$. In the Haydock's scheme, the role of energy is played by the spectral variable $\mathcal{E}\to u$ and that of the Hamiltonian by the longitudinal projection of the characteristic function $\mathcal{H}\to B^{\mathrm{LL}}$. The

matrix elements of the Hamiltonian in the reciprocal space are

$$\mathcal{H}_{\boldsymbol{GG'}} = B^{\mathrm{LL}}_{\boldsymbol{GG'}} = \hat{\boldsymbol{G}} \cdot (B_{\boldsymbol{GG'}} \hat{\boldsymbol{G}'}). \tag{5.12}$$

The hamiltonian is a Hermitian operator which can be represented as a tridiagonal matrix with diagonal elements a_n, $n = 0, 1, 2\ldots$ and sub-diagonal and supra-diagonal elements b_n, $n = 1, 2\ldots$ in a basis of Haydock states $|n\rangle$, $n = 0, 1, 2\ldots$, where a_n and b_n are the Haydock's coefficients. To obtain these states and coefficients, we begin with an initial state $|0\rangle$ and apply the Hamiltonian $\mathcal{H}$ recursively to find all the other Haydock states through

$$|\tilde{n}\rangle \equiv \mathcal{H}|n-1\rangle = b_{n-1}|n-2\rangle + a_{n-1}|n-1\rangle + b_n|n\rangle. \tag{5.13}$$

The Haydock coefficients a_{n-1} and b_n are obtained by requiring the basis states $|n\rangle$ to be orthogonal and normalized, i.e. $\langle n|m\rangle = \delta_{nm}$; yielding $a_{n-1} = \langle n-1|\tilde{n}\rangle = \langle n-1|\hat{\mathcal{H}}|n-1\rangle$ and $b_n^2 = \langle \tilde{n}|\tilde{n}\rangle - a_{n-1}^2 - b_{n-1}^2$.

The macroscopic response function is given by only one element, $\mathcal{G}_{00}$, of the Green's operator, which can written as a continued fraction in terms of the Haydock coefficients and the spectral variable, from which we can write

$$\epsilon_{\mathrm{M}}^{\mathrm{LL}} = \frac{\epsilon_a}{u}\left(u - a_0 - \cfrac{b_1^2}{u - a_1 - \cfrac{b_2^2}{u - a_2 - \cfrac{b_3^2}{\ddots}}}\right). \tag{5.14}$$

Note that the Haydock's coefficients a_n and b_n are dependent only on the geometry of the system through the characteristic function B. Hence, for a given structure, different material compositions can be explored without recalculating the Haydock's coefficients. This is one of the reasons for the high efficiency of this method for the calculation of the response of binary metamaterials. A detailed account of the methodology to obtain Eq. (5.14) can be found in ref. [168].

5.3 Photonic: Microscopic Linear Fields

We now consider a metamaterial formed of an array of infinitely long cylinders made up of a centrosymmetric material in vacuum. We choose the transverse cross-section of the cylinders to have a slight deformation away from a perfect circle, identical to the isolated cylinder of Fig. 3.1. The geometry of the periodic structure is determined in *Photonic* [64] through the characteristic function in a unit cell, represented by a $2D$ matrix of binary pixels that can take values equal to either 0 or 1. For our $2D$ system, we create a unit cell with the cross-section of the noncentrosymmetric cylinder given by Eq. (3.1) by choosing the values of all pixels lying within the material to be equal to 1 and

in vacuum to 0. Fig. 5.1 displays a schematic diagram for the geometry of our metamaterial. We must point out that the curved boundary of the surface is not properly represented by the pixelated matrix as it has steps and thus is rough, instead of being smooth [Fig. 5.1]. These steps may play an important role in systems where the surface contribution is important, as they may modify its response due to the presence of sharp corners, particularly for metals. Inclusions with a rectangular form or those resembling shapes of the alphabets such as T, L, or E etc., with only horizontal and vertical borders, would have smooth boundaries and their properties would not be influenced by these steps.

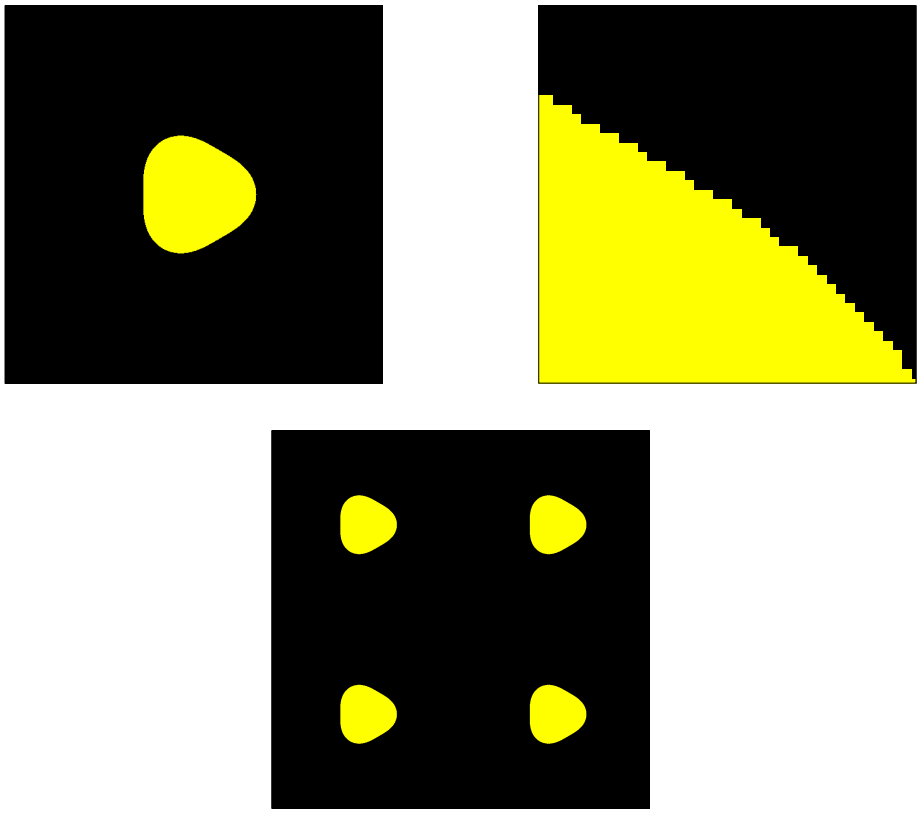

Figure 5.1: Cross-section of the cylindrical meta-atoms of the array in vacuum described by Eq. (3.1) with $\xi = 0.1$. Unit cell with one inclusion (top left panel), a zoomed in view of the surface (top right panel), a 2×2 region cut out of the infinite metamaterial (bottom center). Pixels with value 1 and 0 are indicated by the colors yellow and black respectively.

The programming package *Photonic* [64] includes modules to evaluate the microscopic fields induced in the metamaterial, in addition to those that calculate the macroscopic linear response using the efficient homogenization approach discussed in Secs. 5.1 and 5.2 and Eq. (5.5). We will now compare these numerically computed self consistent microscopic fields for the metamaterial to those calculated analytically for the isolated cylinder [Eq. (3.13)]. We choose a unit cell with $(2N+1) \times (2N+1) = 401 \times 401$ pixels and evaluate 150 Haydock's coefficients to obtain well converged results. We consider an array of dielectric or metallic cylinders periodically arranged in a $2D$ square lattice

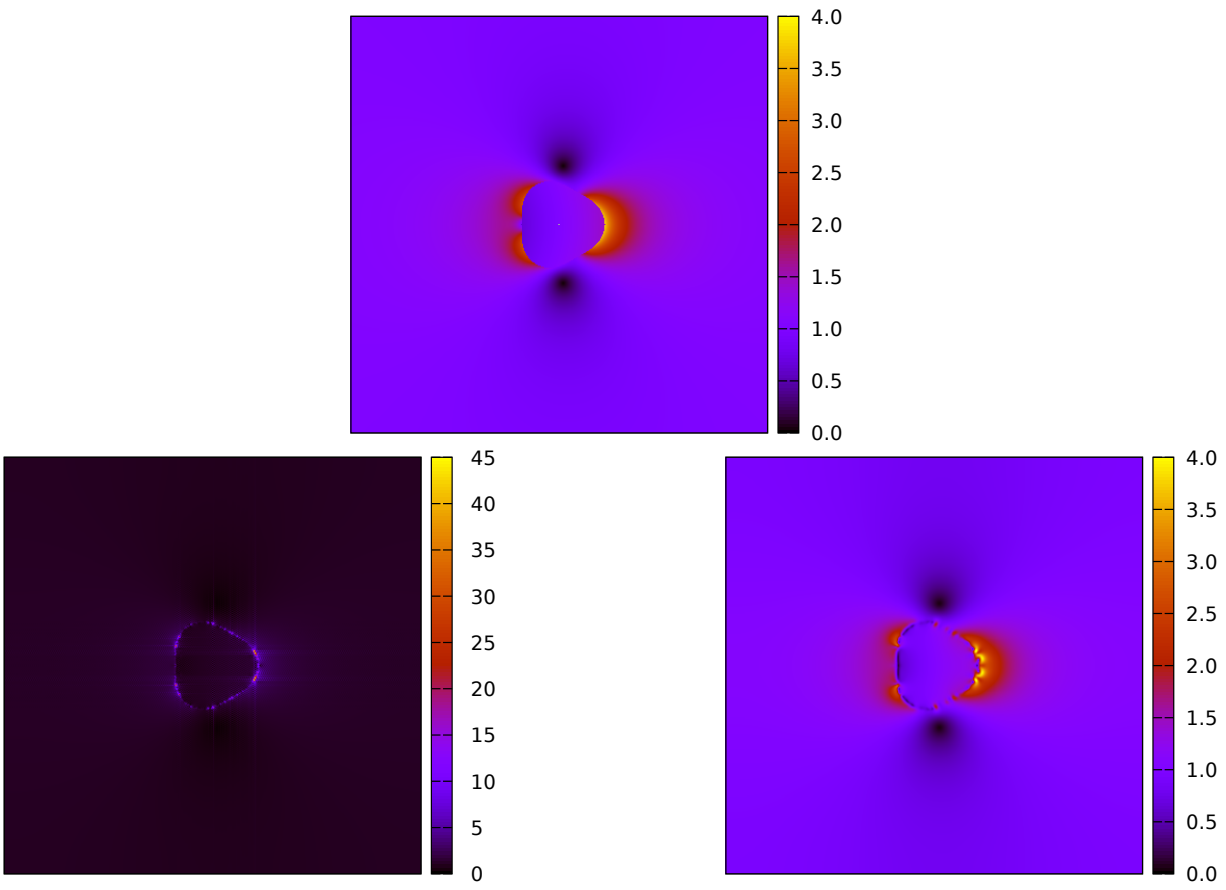

Figure 5.2: Absolute value of the self consistent linear electric field for deformed cylindrical metallic nanowires with dielectric function given by Eq. (3.51) with lifetime $\tau = 100/\omega_p$ evaluated at the frequency $\omega = 0.5\,\omega_p$. The ratio between the nominal radius r_0 and the lattice parameter L is $r_0/L \sim 1/10$ and the deformation parameter is $\xi = 0.1$. The analytical field for an isolated metallic cylinder is shown at the top and the numerical microscopic field within a metamaterial made of a square lattice of the such cylinders at the bottom. For the numerical calculation we employed a unit cell with $(2N+1) \times (2N+1) = 401 \times 401$ pixels. We show the field obtained numerically without further processing (bottom left panel) and after applying a Gaussian filter in reciprocal space (bottom right panel).

in vacuum with their transverse cross section described by Eq. (3.1) to demonstrate and discuss our observations.

Fig. 5.2 shows the self-consistent field obtained from our perturbative analytical method [Eq. (3.13)] for the isolated metallic cylinder (top) and the numerically computed microscopic field within a metamaterial formed of an array of such cylinders (bottom). The permittivity of the metal is assumed to be of the Drude type given by Eq. (3.51) with only one pole at $\omega = 0$ and its value being positive above the plasmon frequency ω_p and negative below it. The results are calculated for a deformation $\xi = 0.1$, a nominal radius r_0 corresponding to 40 pixels, a lattice parameter L corresponding to $2N + 1 = 401$ pixels, and at the frequency $\omega = 0.5\,\omega_\mathrm{p}$. Note that the dielectric

permittivity of the metal is negative at this frequency. The numerical microscopic field [bottom left panel of Fig. 5.2] is very large right at the surface; almost an order of magnitude larger than the analytical field. These large values originate in the field singularities expected at sharp corners of a metallic particle below its plasma frequency and they are absent for particles with positive dielectric functions. However, the sharp corners are not real, but an artifact due to the approximation of a curved boundary by a pixelated array [top left panel of Fig. 5.1]. To overcome this problem, we smooth out the estimated field by filtering it in reciprocal space using a low pass filter with a Gaussian kernel using a cutoff equal to $N/4$ in a unit cell of $(2N+1) \times (2N+1)$ pixels [bottom right panel of Fig. 5.2]. The smoothed out field has a structure qualitatively very similar to that of the analytical case and closely agrees quantitatively with it except in the immediate vicinity of the surface, where it still shows some small residual fluctuations. Notice that we choose a small ratio of the radius of the inclusion to the lattice parameter $r_0/L \sim 1/10$, so that the inter-inclusion separation is relatively large and we may expect the interaction between the inclusions in the metamaterial to be small. Hence, the agreement with the analytical calculation. For larger cylinders, their mutual interactions are expected to become important, thus invalidating the isolated single cylinder approximation made in our analytical calculation. To illustrate this, we plot the self consistent induced linear fields for two different radii. Fig. 5.3 shows a 2×2 region of the metamaterial formed of the same inclusions as in Fig. 5.2 for $r_0/L \sim 1/10$ (left panel) and $\sim 1/4$ (right panel). For smaller cylinders or larger inter-inclusion distances (left panel), the absolute values of the induced fields between two inclusions reaches zero. Hence, an interaction between the inclusions, in this case, may not occur. However, for larger radius (right panel), the inter-inclusion distance is reduced and the interaction between the cylinders becomes important. In this regimen, the absolute values of the induced fields in the interstitial region is never null. In this regime, the analytical results do not apply. Hence, to validate our numerical computation against the analytical results for the SH response of the metamaterial we choose the smaller radius.

Fig. 5.4 demonstrates the field determined analytically and numerically for the same system as in Fig. 5.2 but made up of a dielectric material with a Lorentzian dielectric permittivity given by Eq. (2.26), with a transverse and longitudinal optical mode frequencies related by $\omega_{\mathrm{L}} = \sqrt{2}\,\omega_{\mathrm{T}}$. The permittivity of the material has a pole at ω_{T}; is zero at ω_{L}, negative between the two frequencies and positive otherwise. The fields, both numerical and analytical, are calculated for the normalized frequency $\omega = 0.5\,\omega_{\mathrm{T}}$ where the dielectric permittivity is positive. Unlike the metallic case, there are no large fluctuations near the surface in the microscopic fields (left panel) for the dielectric cylinders. We remove the small fluctuations as in the metallic case, by applying the same Gaussian filter, as previously mentioned for the metallic case, in the reciprocal space. The filtered field (right panel) is found to be almost identical to the analytical field. As we did for the metallic case, in Fig. 5.5 we show the induced fields for different nominal radii of the cylinders. For larger radius, the inter-inclusion distance becomes small and the interaction between neighbor cylinders becomes evident.

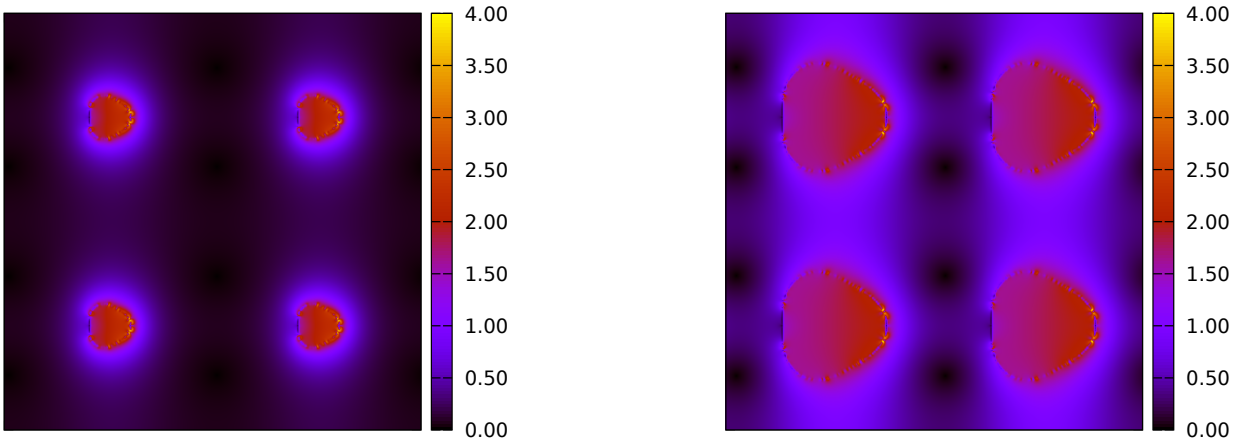

Figure 5.3: Microscopic induced field numerically calculated for a metamaterial made of a square lattice of deformed cylinders as in Fig. 5.2 but of different nominal radii r_0. We show a region with 2×2 unit cells. We choose the ratio $r_0/L \sim 1/10$ (left) and $r_0/L \sim 1/4$ (right). The unit cell has $(2N+1) \times (2N+1) = 401 \times 401$ pixels.

5.4 Photonic: SH response

The package *Photonic* also has modules to evaluate the nonlinear SH polarization and the susceptibility tensor of a binary metamaterial using the *dipolium* model [124]. The computation of the second order response begins with the calculation of the microscopic nonlinear dipole and quadrupole moments described by Eqs. (2.50) and (2.51) induced within the metamaterial. The modules are restricted to the long wavelength approximation and hence the term corresponding to the *curl* of the field in Eq. (2.50) is ignored. These moments are then used to calculate the total nonlinear polarization, given by Eq. (2.52). The depolarizing field at the SH is then utilized to obtain the screened self consistent nonlinear polarization; the process is illustrated in Fig. 2.2. Finally, this self consistent microscopic nonlinear polarization is averaged to obtain the macroscopic SH polarization from which the SH susceptibility tensor of the metamaterial is extracted.

We now explore the SH response from our deformed cylinders obtained using the SH modules of *Photonic*. Our analysis of the microscopic linear fields hints that the presence of steps with corners at the interface makes the fields near the surface to be poorly approximated exhibiting singularities and/or artificial oscillations. Hence, we anticipate that the nonlinear polarization computed by the package may give erroneous results in the vicinity of a surface with steps, but it may give appropriate results in the vicinity of a flat horizontal or vertical surfaces oriented with the pixelated sides. An investigation into the SH response from an array of cross shaped holes in Silver (Ag) using *Photonic* have been recently reported [71] where the use of horizontal and vertical surfaces of the inclusions helped avoid the problems that arise due to the presence of the steps.

The numerically computed SH susceptibility tensor of a square array of deformed cylinders with an abrupt interface and the analytical dipolar hyperpolarizability given by Eq. (3.31) normalized

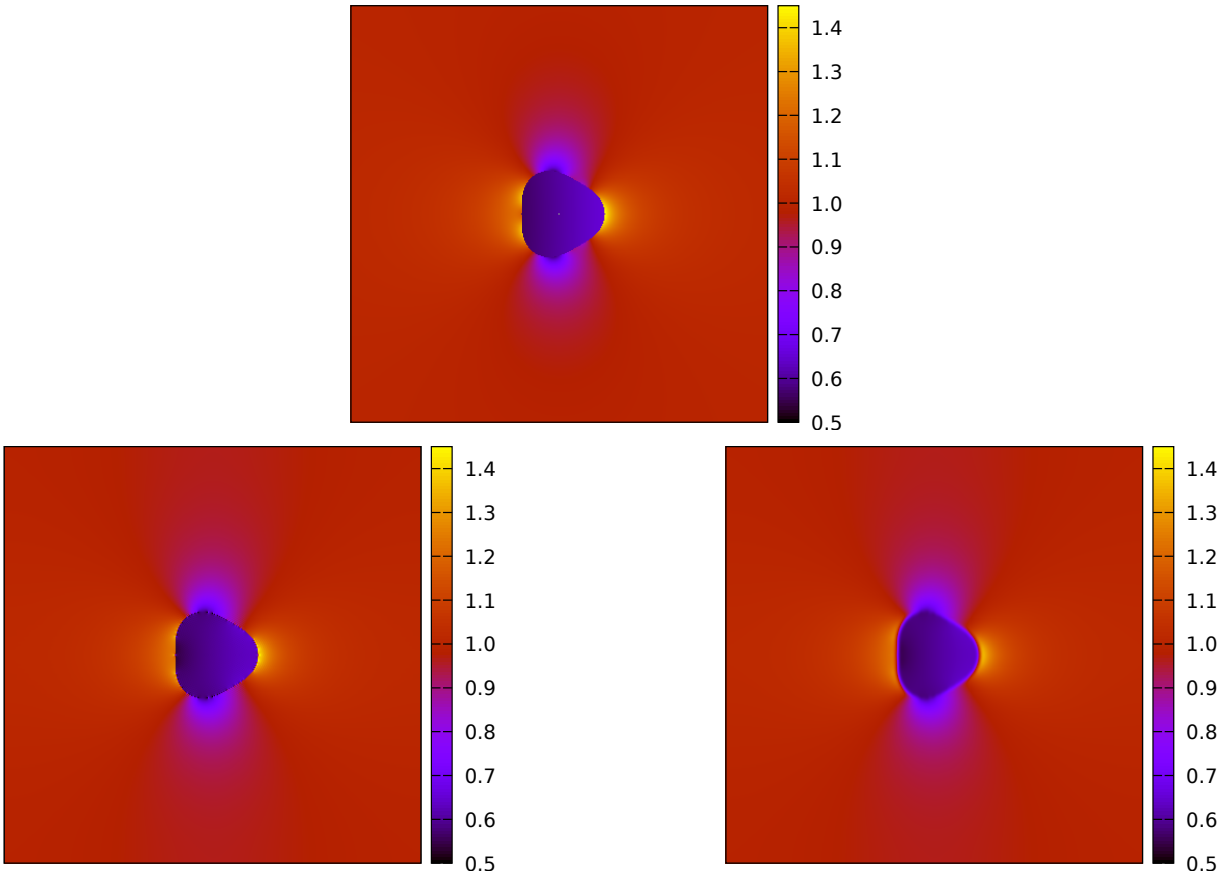

Figure 5.4: Absolute value of the self consistent field calculated analytically for an isolated dielectric cylinder with the same geometry as in Fig. 5.1 (top) calculated numerically within a metamaterial made of a square array of such cylinders (bottom). We show results obtained numerically without further processing (bottom left) and after applying a Gaussian filter in reciprocal space (bottom right). The dielectric function of the material is given by Eq. (2.26) with $\omega_{\mathrm{L}} = \sqrt{2}\,\omega_{\mathrm{T}}$, and $\tau = 100/\omega_{\mathrm{T}}$ and we chose $\omega = 0.5\,\omega_{\mathrm{T}}$.

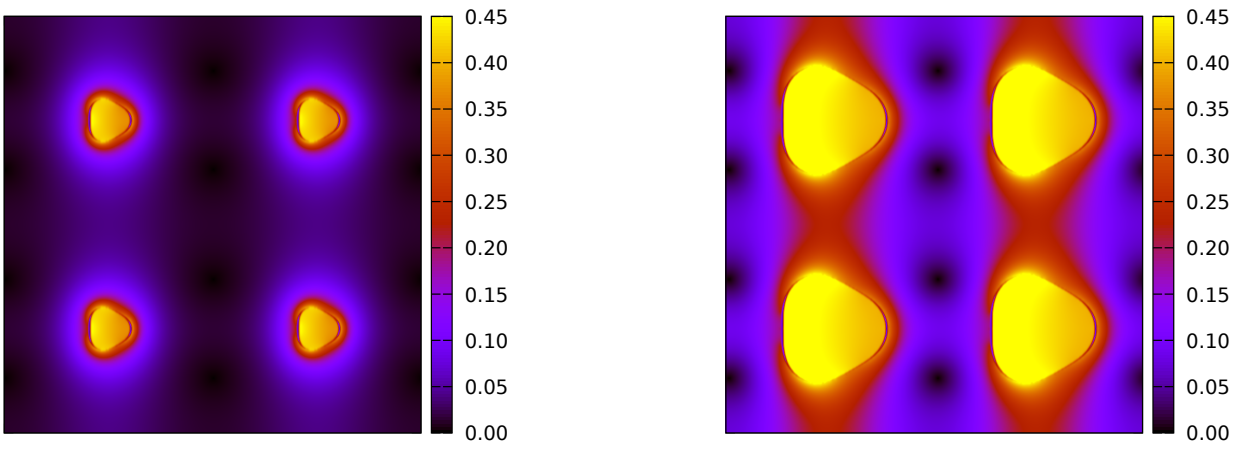

Figure 5.5: Absolute value of the induced fields for a metamaterial made of a square lattice of deformed dielectric cylinders as in Fig. 5.1 with parameters corresponding to those in Fig. 5.4 but of different nominal radii. We show a region with 2×2 unit cells. We choose $r_0/L \sim 1/10$ (left) and $r_0/L \sim 1/4$ (right).

to the area of the unit cell are shown in Fig. 5.6. Additionally, the susceptibility being defined in terms of the response to the macroscopic field, is divided by ϵ_M^2, to compare it to the polarizability defined in terms of the response to the external field. The dielectric permittivity of the material is chosen to be given by Eq. (2.26) with the relation between the longitudinal and transverse optical mode frequencies $\omega_{\mathrm{L}} = \sqrt{2}\,\omega_{\mathrm{T}}$ and lifetime parameter $\tau = 10/\omega_{\mathrm{T}}$. A rough resemblance in the overall spectral shape can be observed, with the numerical results closely following the analytical curves. The peaks at the surface plasmon polariton (SPP) resonance, $\omega_{\mathrm{spp}} = \sqrt{3/2}\,\omega_{\mathrm{T}}$, and its subharmonic in the numerical χ_{xxx} (left panel) have some discrepancies with the analytical one: a red shift of the SPP peak and a blue shift at the subharmonic of the SPP resonance, smaller peak values and somewhat differing lineshapes. In addition to this, our numerical results do not satisfy the relation between different components of the $\boldsymbol{\chi}$ tensor (right panel) arising due to the symmetry [Eq. (3.38)]. We must point out that as the metamaterial is designed in the form of a square array of the cylinders, the rotational symmetry of the isolated cylinder, Eq. (3.38), is lost indicating that the susceptibility tensor $\boldsymbol{\chi}$ must possess more independent components. However, as the inter-inclusion distance is large and the intercylinder interactions are expected to be negligible, we do expect the suceptibility components to comply approximately with the symmetries of the isolated cylinder. Thus, our calculation of the nonlinear polarization and the SH susceptibility of the deformed cylinders displays erroneous results which might arise from the presence of steps in the pixelated approximation to the curved boundary.

Planar Surface

We now turn our attention to the calculation of the nonlinear polarization calculated by the *Photonic* package for a planar surface which we might expect to be more precise. In order to validate

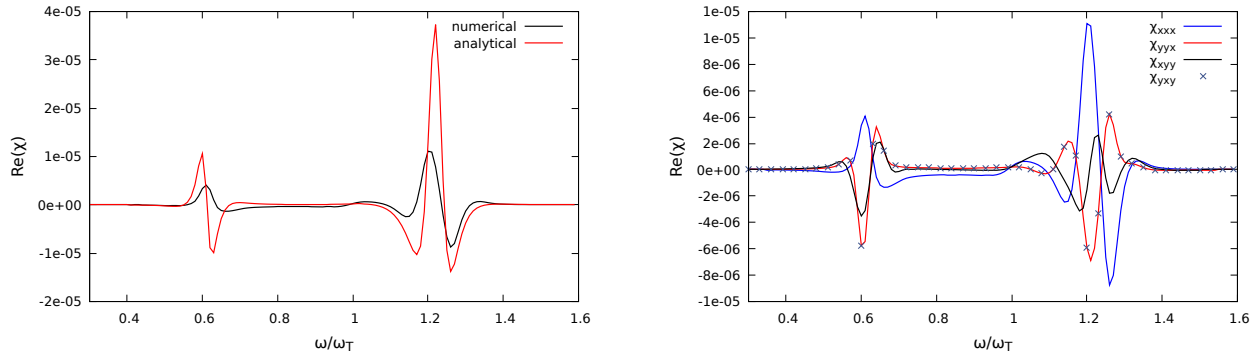

Figure 5.6: Numerically and analytically computed real part of the SH susceptibility tensor component χ_{xxx} (left panel), as a function of the normalized frequency $\omega/\omega_{\mathrm{T}}$, for a deformed cylinder with an abrupt interface, such as the one in Fig. 5.1, with $r_0/L \sim 1/10$ and deformation $\xi = 0.1$. The cylinder is made up of a dielectric material whose permittivity is given by Eq. (2.26) with the lifetime parameter $\tau = 10/\omega_{\mathrm{T}}$. Real part of the different components of the second order susceptibility $\boldsymbol{\chi}$ computed numerically.

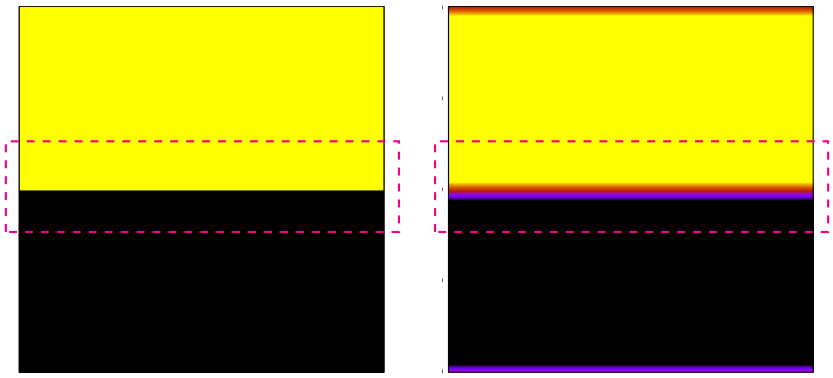

Figure 5.7: Unit cell of $1D$ layered structure used to study the properties of an infinite planar surface. Yellow regions indicate the material and black denotes vacuum. Abrupt surface (left panel) and a thick surface (right panel). The different colors between yellow and black in the figure on the right indicates a continuous variation in density of particles when going from the homogeneous medium to vacuum, whose value have been normalized to one for simplicity. The dashed rectangle qualitatively illustrates the mask used to isolate the surface response.

the nonlinear response in the close vicinity of a planar surface, we investigate a semi-infinite homogeneous system, identical to that used to calculate the surface response within the *dipolium* model. However, the package *Photonic* can only be applied to periodic systems. Thus, we consider the geometrical configuration shown in the left panel of Fig. 5.7 which essentially is a $1D$ layered structure with alternating centrosymmetric materials. The nonretarded, nonlinear polarization in this system would be zero everywhere except at the interfaces where the normal field has a large gradient. Nevertheless, the layered geometry of Fig. 5.7 is centrosymmetric and would yield a null total nonlinear polarization when the contributions of the two interfaces within a unit cell are added. Hence, to obtain the SH response of the planar interface, we select a thin region around one interface using a mask, illustrated by the dashed rectangle in Fig. 5.7, and add up only the contributions within the masked region. The normal component of this nonlinear surface polarization, related to the dimensionless parameter $a(\omega)$, is thus calculated numerically. We compare the spectra of the numerically computed $a(\omega)$ with the analytical expression Eq. (2.55). We choose the system to be made up of the same insulator of which the dielectric cylinder of Fig. 5.6 was composed. The top panels of Fig. 5.8 shows the real (left) and imaginary (right) parts of the function $a(\omega)$ for an abrupt surface as function of $\omega/\omega_{\mathrm{T}}$ for the dielectric planar surface. The numerically evaluated a does not compare well with the analytical one except at very low and high frequencies. Hence, our assumption that the nonlinear polarization evaluated for horizontal or vertical surface by the SH modules of the package are precise turns out not to be entirely true. The steps, arising when curved boundaries are modelled by an array of pixels, contributing to inaccuracies due to the sharp corners is only a part of the whole story.

A tentative explanation for the discrepancy between the analytical and numerical calculation even for a flat surface is the following. The normal component of the electric field is discontinuous exactly at the interface possessing an infinite gradient. The numerical calculation, being discrete approximates the surface with just one pixel exactly where the discontinuity in the field resides. The gradient of the field appears as a singularity at the surface and leads to inaccurate estimation of the nonlinear response by our program. To solve this, we can replace the sharp interfaces by continuous density profiles. Thus, we spread the interface over a few pixels instead of abruptly changing from vacuum to the medium in just one pixel. To verify this assumption, we consider the same $1D$ layered structure as above, but with a thick interface, 10 pixels wide with the density linearly interpolating between the medium and the vacuum, as illustrated by the right panel of Fig. 5.7. We show the real (left) and imaginary (right) parts of the dimensionless function $a(\omega)$, calculated by both numerical and analytical means, in the bottom panels of Fig. 5.8. An excellent agreement between the two is observed except between the frequencies ω_{T} and ω_{L} where the numerical curves exhibits oscillations. This is the regimen where the dielectric permittivity ϵ_{d} within the material is negative. We must point out that within this frequency region, the dielectric permittivity, for a continuously varying particle density that interpolates between vacuum and bulk across the thick surface, would go from a value 1 in vacuum to a negative value within the medium, necessarily crossing zero somewhere in between. As the normal component of the displacement field is nearly constant across the thick

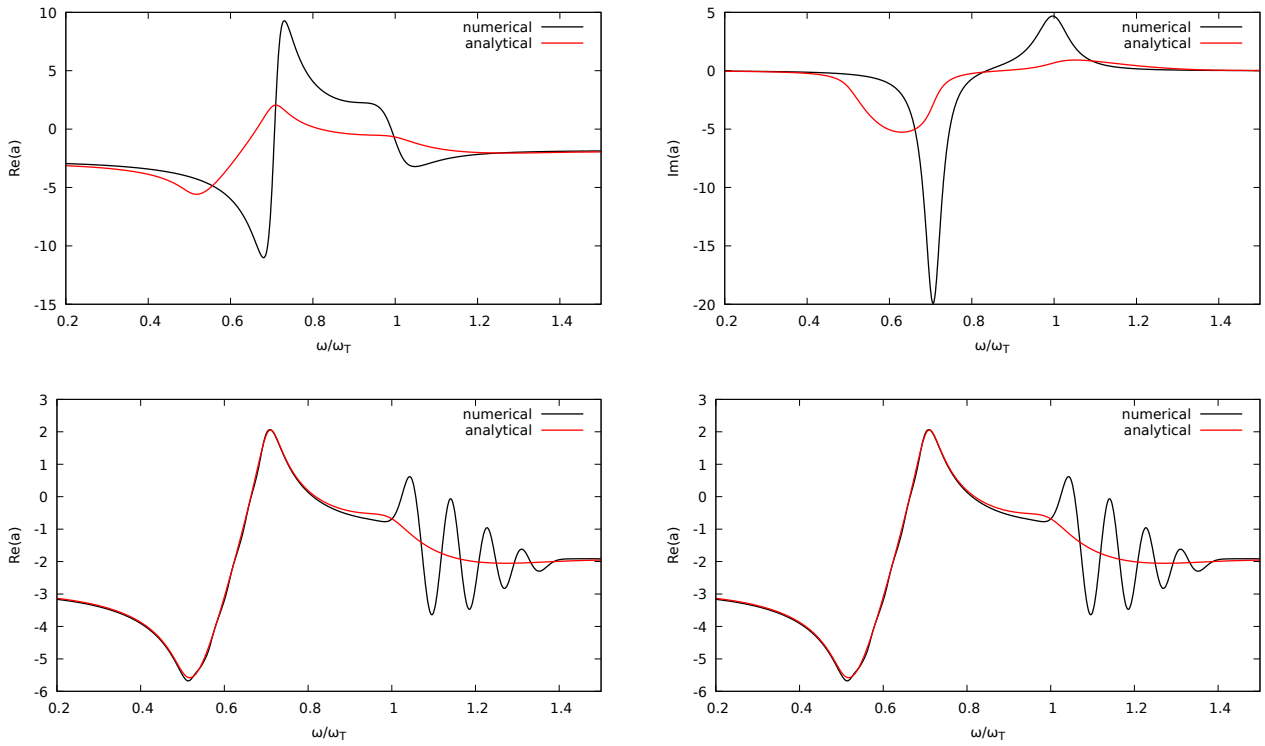

Figure 5.8: Real (left panels) and Imaginary (right panels) of the dimensionless function $a(\omega)$ of the SH type given by Eq. (2.55) for an infinite planar abrupt (top panels) and a thick (bottom panels) surface, similar to Fig. 5.7, with the dielectric permittivity of the material given by Eq. (2.26) with $\tau = 10/\omega_{\mathrm{T}}$.

interface, the electric field i.e. $E_\perp = D_\perp/\epsilon$, would have a pole at some position within across the widened surface. Since, ϵ is frequency dependent, the position of this singularity would dependend on frequency. We don't expect a pixelated representation of the system to permit an accurate description of this localized singularity. Furthermore, as the frequency varies, the position of the singularity may hit one or another of the pixels. This manifest itself as an oscillatory behavior in the nonlinear response when the permittivity of the material is negative, with the number of oscillations dependent on the number of pixels across the selvedge, as we have verified by repeating the calculation with different widths. This brings us to the conclusion that while a thick surface may help in avoiding the problems due to the discontinuity of the fields, the inaccuracies in our numerical calculations arising for negative permittivities demands a solution.

Periodic array of noncentrosymmetric cylinders with thick interfaces

Notwithstanding the last remarks of the previous subsection, we now choose a metamaterial formed of a periodic array of infinite noncentrosymmetric dielectric cylinders [Fig. 5.1] but instead of making their interfaces abrupt, we assume a thick selvedge where the density of polarizable entities inter-

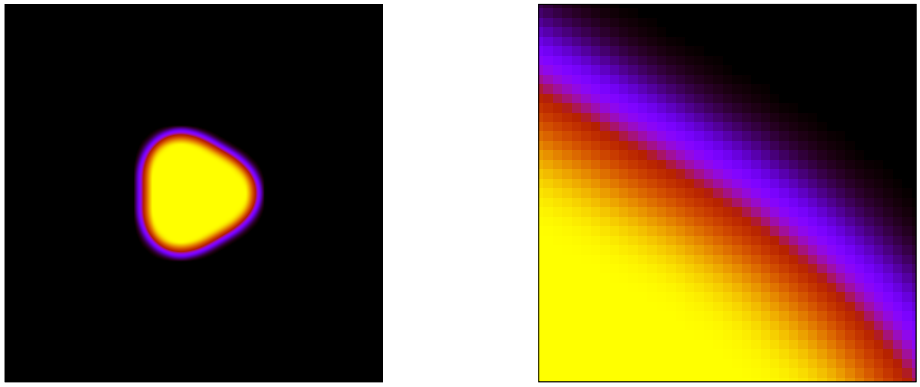

Figure 5.9: Unit cell (left panel) of a periodically array of the deformed cylinders with thick surface and a zoomed in view of the surface (right panel). The color yellow and black represents the two homogeneous materials of the inclusions and the host respectively, with the continuously varying density demonstrated by the different colors in between.

polates from vacuum to their bulk value within the material. Fig. 5.9 illustrates the unit cell and a zoomed in view of the surface for such a metamaterial. The dimension and the material parameters for these cylinders are chosen identical to those in Fig. 5.6 but with a thicker selvedge formulated using a $2D$ Gaussian function spread over 20×20 pixels. The left panel of the figure Fig. 5.10 shows the real part of the SH susceptibility tensor component χ_{xxx} obtained both numerically and analytically [from Eq. (3.31)]. As mentioned previously, the susceptibility is defined in terms of the response to the macroscopic field, and the polarizability is defined in terms of the response to the external field, hence we divided the numerically obtained susceptibility by ϵ_M^2. As in Fig. 5.6, the numerical and analytical curves show some resemblance in their overall spectra with differing values of peaks at the SPP and its sub-harmonic. Note, that for the thick cylinder, the numerical curve is more than an order of magnitude smaller than the analytical result. However, the peak positions for the numerical curve appear to have shifted back and have a better agreement with those of the analytical results, though the latter are much sharper and narrower than the former. To illustrate this in Fig. 5.11 we plot χ_{xxx} obtained analytically and numerically for both an abrupt and a thick selvedge. Notice the shift in the peaks between both the numerical curves (black and blue).

From Fig. 5.11, we can conclude that our pretension of resolving the inaccuracies in *Photonic* using a thick selvedge, i.e. a continuous interpolation of density between the two media, is not sufficient. The right panel of Fig. 5.10 displays the different components of the susceptibility tensor for the thick cylinder. In this case, the symmetry relation, Eq. (3.38), between the components is satisfied. Thus, tweaking the manner in which the geometry of the system is described in *Photonic*, we were able to capture the fundamental effects of the structure and symmetries of the system, although failing to estimate precise values.

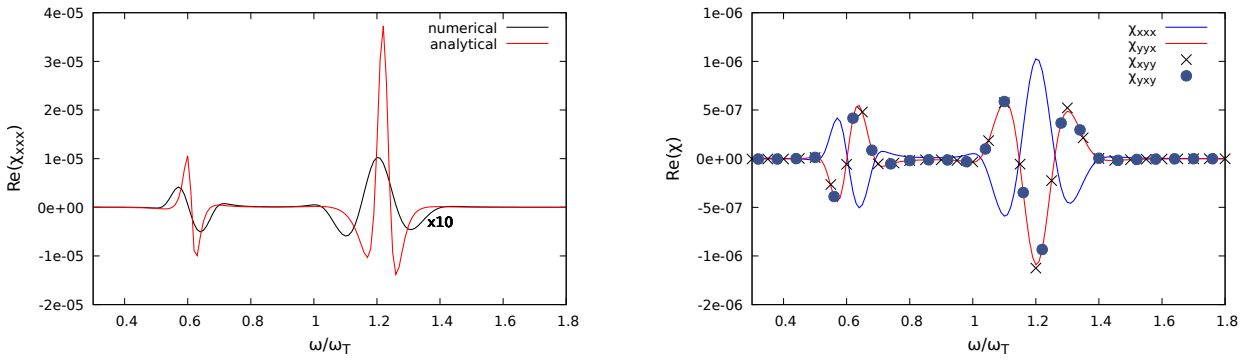

Figure 5.10: Real part of the SH susceptibility tensor component χ_{xxx} (left panel) calculated numerically for a deformed cylinder with a thick selvedge and analytically for the corresponding cylinder with abrupt interfaces, as function of the normalized frequency $\omega/\omega_{\mathrm{T}}$. The cylinder havethe same geometry as in Fig. 5.9 and identical material parameters as in Fig. 5.6. Real parts of the different components of χ tensor calculated numerically are shown in the right panel.

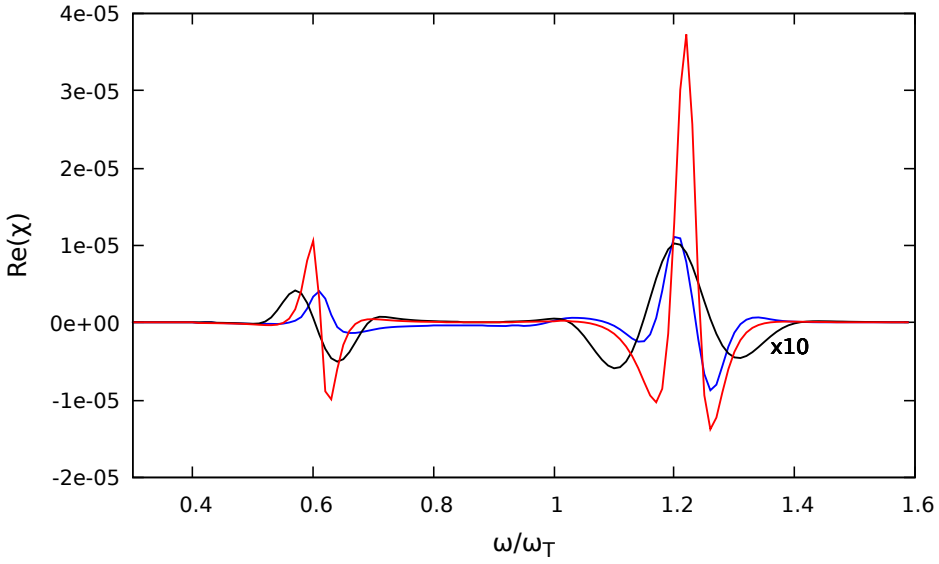

Figure 5.11: Real part of the χ_{xxx} component of the SH susceptibility tensor calculated analytically (red) and numerically for a dielectric cylinder as in Figs. 5.6 and 5.10 respectively but with thin (blue) and thick (black) selvedges, as a function of the normalized frequency $\omega/\omega_{\mathrm{T}}$. The numerical results for the case of a thick selvedge is multiplied by a factor of 10.

Nonlinear surface response of deformed cylinders

Observing the results presented in Fig. 5.10, as concluded in the previous paragraph, *Photonic* reproduces the nature of the spectra and the symmetry of the analytical SH response tensor but doesn't yield the correct values close to the resonances. We believe that this happens because of the inconsistencies that arise when the response and the induced fields are computed at the surface. Our analysis of the linear microscopic fields [Sec. 5.3] showed spurious large fluctuations of the microscopic fields at the surface originated in its steps. Furthermore, our results for the normal component of the nonlinear polarization at the planar surface, characterized through the parameter $a(\omega)$, exhibited how the discontinuity and singularity of the field at a surface where the permittivity changes sign are the reasons for this inaccurate evaluation. To test this diagnosis, we single out the contributions to the nonlinear polarization coming from the surface of the inclusions, integrate it across the surface and compare the numerical and the analytical calculations. The normal $P^s_{\mathrm{sh},\perp}$ and the tangential $P^s_{\mathrm{sh},\parallel}$ components of the nonlinear surface polarization at any point on the surface calculated analytically is given by Eqs. (3.20) and (3.21) respectively. The nonlinear surface dipole moment per unit area length is then computed by integrating these local contributions to the surface nonlinear polarization utilizing an equation similar to Eq. (3.22) which we may write as

$$\boldsymbol{p}^s_{\mathrm{def}} = \int_0^{2\pi} (P^s_{\mathrm{sh},\perp}\,\hat{\boldsymbol{n}} + P^s_{\mathrm{sh},\parallel}\,\hat{\boldsymbol{t}})\, r_0(1+\xi\cos 3\theta)\, d\theta, \tag{5.15}$$

where the unit vectors normal $\hat{\boldsymbol{n}}$ and tangential $\hat{\boldsymbol{t}}$ to the surface are given by Eqs. (3.10) and (3.24). To compute the surface nonlinear polarization numerically, we first evaluate the microscopic self consistent linear fields induced within the metamaterial, average them using a kernel to eliminate their singular behavior at the surface, and then substitute them in Eqs. (3.17) to (3.19). It is then summed over the entire boundary to obtain the quadratic surface dipole moment per unit length. For both the numerical and analytical calculations, we normalize our results to the factor ne appearing in Eqs. (3.19) to (3.21). The self-consistent fields obtained numerically have been normalized using the macroscopic permittivity of the metmaterial, so that they can interpreted as the response to the external, not the macroscopic field, as for the analytical response. The absolute value of the x component of this nonlinear surface dipole moment per unit length is shown in Fig. 5.12 for the same dielectric deformed cylinder as in Fig. 5.6, for the case of an abrupt interface, and for two different lifetime parameters $\tau = 10/\omega_{\mathrm{T}}$ (left panel) and $\tau = 100/\omega_{\mathrm{T}}$ (right panel). Notice that the numerical curve overlaps the analytical one completely when the absorption in the material is large, corresponding to a relatively small τ, differing slightly only at the SPP peak. For low absorption, corresponding to a relatively large τ, the numerical curve mimics the nature of the spectra of the analytically evaluated quadratic surface dipole moment except at the SPP resonance where it splits into two smaller peaks, one located below and the other above the nominal resonance. It is also two orders of magnitude smaller than the analytical case. We believe that this splitting might be due to the fact that for the undeformed cylinder, all the multipolar resonances are degenerate and

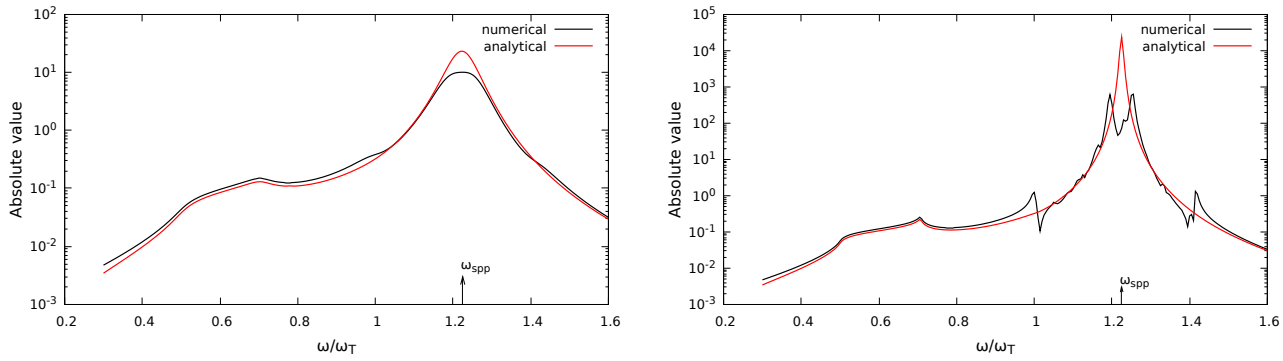

Figure 5.12: Normalized absolute value of the $x-$ component of the nonlinear surface dipole moment per unit length of the same deformed cylinder as in Fig. 5.6 with an abrupt interface as a function of the normalized frequency $\omega/\omega_{\mathrm{T}}$ for two different lifetimes $\tau = 10/\omega_{\mathrm{T}}$ (left panel) and $\tau = 100/\omega_{\mathrm{T}}$ (right panel).

have the same frequency. Thus, any interaction between different multipoles, such as those due to a deformed shape or due to the interaction among different particles may break the degeneracy, and this would be more noticeable when the absorption in the medium is low and the resonances are larger and narrower. As our perturbative analytical theory did not account for this degeneracy, it doesn't show this splitting. Additional small structures are visible for the numerical results at ω_T and ω_L for the case of low absorption.

5.5 Results: Analytical vs Numerical SH response

We now turn our attention towards the resolution of the problems we discussed in the previous sections by updating the SH code of *Photonic* with a new formulation for the calculation of the surface nonlinear polarization. To this end, we separate the bulk and surface regions, shown in Fig. 5.13, and use a hybrid technique to determine the total nonlinear polarization including well defined surface and bulk contributions. We describe our procedure using the metamaterial illustrated in Fig. 5.1.

1. We begin with the calculation of the self consistent microscopic fields within the metamaterial using the respective *Photonic* modules.

2. Next, we compute the external (unscreened) nonlinear polarization source induced at all the points of the matematerial using the existing modules of *Photonic*.

3. We construct a mask to identify the pixels corresponding to the interfaces. To that end, we use the numerically calculated gradient ∇B of the characteristic function (Fig. 5.1) which is zero everywhere in the metamaterial except at the interfaces where its value of the pixel changes

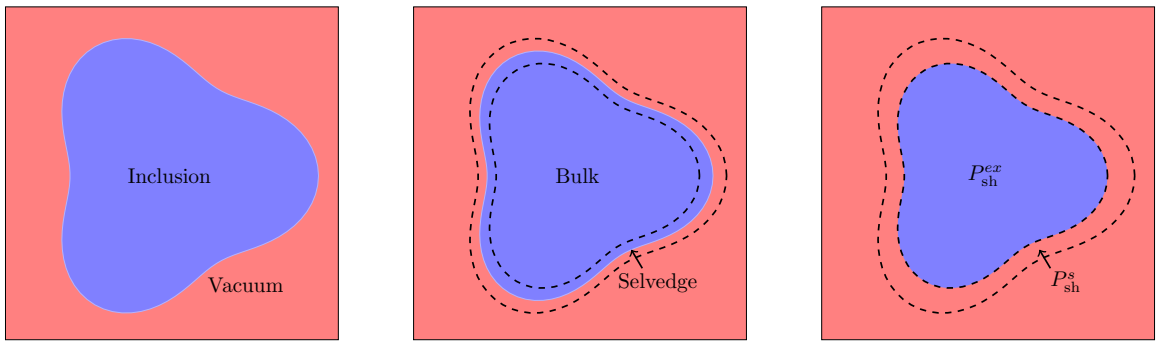

Figure 5.13: A schematic representation of the separation of the inclusion into bulk and selvedge regions for the hybrid calculation. Unit cell with a single inclusion (left panel). Inclusion divided into bulk and selvedge regions (center panel). Setting the selvedge in vacuum with self consistent polarization $P^{s}_{\rm sh}$ obtained from the semi-infinite *dipolium* model and the bulk with numerical external polarization $P^{ex}_{\rm sh}$ (right panel).

between 0 and 1. We evaluate this gradient using centered differences. The segregated bulk and surface regions are illustrated in the center panel of Fig. 5.13.

4. We select the surface region of the inclusions using this mask and we replace its nonlinear polarization by the self-consistent surface polarization $\boldsymbol{P}^{s}_{\rm sh}$ with parallel and perpendicular components given by Eqs. (2.53) and (2.56) using the numerically computed microscopic averaged linear fields. The averaging is performed by applying a convolution using a small $2D$ kernel in real space eliminate spurious surface fluctuations yielding smoother fields. That is, we replace, in the surface region, $\boldsymbol{P}^{ex}_{\rm sh}$ by $\boldsymbol{P}^{s}|\nabla B|$, as $|\nabla B|$ is a numerical approximation to a Dirac's delta function at the interface. Thus, the surface response is evaluated using the analytical results of the *dipolium* model but using the smoothed numerical linear fields.

5. We use the same surface mask to change the composition corresponding to those pixels at the surface, removing their material and replacing it by vacuum. This way, we avoid screening the already selfconsistent response at the surface region in the following steps. Thus, we shrink the inclusions by a small distance, corresponding to the *selvedge* region (right panel of Fig. 5.13).

6. We set the external polarization $P^{ex}_{\rm sh}$ of the shrinked inclusions to that calculated in step 2 (right panel of Fig. 5.13).

7. At this point we have at our disposal, the building blocks for our new hybrid SH calculation; the external bulk polarization within the bulk of the inclusions and the self consistent surface polarization at the *selvedge* region which we situate in vacuum. Finally, we combine them to obtain the total nonlinear polarization which is then screened appropriately to evaluate the self consistent quadratic polarization from which the SH susceptibility tensor components are identified.

We must point out that the *selvedge* region with the contribution of the nonlinear surface polarization, calculated analytically using the *dipolium* model, being already self-consistent is deliberately set in vacuum so as to not screen it again.

Fig. 5.14 demonstrates the normalized real values of the SH susceptibility tensor component χ_{xxx} of a metamaterial made of a square array of deformed cylindrical inclusions with an abrupt interface with the same material parameters as in Fig. 5.6. The numerical results have been compared against the analytical ones for different deformation parameters and for $r_0/L \sim 1/10$ in vacuum. We find that for deformation parameter $\xi = 0.1$ (top right panel), the numerical results agree reasonably well with the analytical ones with almost an identical structure (a maxima followed by a minima) at the subharmonic of the SPP resonance, $\omega_{\text{spp}} = \sqrt{3/2}\,\omega_{\text{T}}$, and with a similar lineshape of the resonant response (a minima followed by a maxima and another minima) at the fundamental SPP resonance, albeit slightly red shifted. In addition to these, the numerical curve also exhibits an additional structure in the form of a small maxima followed by minima, absent from the analytical result, at the frequency $\omega \approx 1.3\,\omega_{\text{T}}$. We suspect that this minima is related to the splitting of the SPP resonances that are degenerate for the unperturbed circular cylinder, as shown in theright panel of Fig. 5.12 . At very small deformations, the geometry of the curved boundary of the inclusions is not well described by a pixelated array, and thus the numerical calculation of the SH response might loose precision; we verified this by calculating the results for a smaller deformation $\xi = 0.05$ (top left panel). The structure at the SPP resonance displays a more pronounced red shift and the additional minima at $\omega = 1.3\,\omega_{\text{T}}$ is larger in size and comparable to the size of the primary minima at SPP. The structure at the subharmonic, however, compares well with the analytical results. On the other hand, for large deformations our approximate analytical theory is not valid and may not compare with the numerically obtained results where no such perturbative theory is applied. We demonstrate this by plotting the results for $\xi = 0.2$ (bottom left panel) and $\xi = 0.25$ (bottom right panel). Notice that, for $\xi = 0.2$ the red shift in the primary resonance structure at frequency ω_{spp}, computed numerically, with respect to the analytical curve is considerably large and the adjoining minima has grown to become comparable to the primary minima at the SPP resonance. The numerical curve also exhibits a small variation at the subharmonic resonance, with a broader and smaller structure. For even larger deformations, $\xi = 0.25$, the spectral dependence of the numerical result near the SPP resonance differs considerably from the analytical result, while the one at its subharmonic is still similar albeit broader and smaller, as in the case of $\xi = 0.2$. Note, that the second minima overshoots the primary becoming dominant over it.

In Fig. 5.15, we plot the normalized absolute values of the SH susceptibility tensor component χ_{xxx}, calculated numerically, for the same metamaterial as in Fig. 5.14 for different deformations. The curves display peaks at the excitation of the SPP and its sub-harmonic with an additional peak at $\omega = 1.3\,\omega_{\text{T}}$ near the main peak at the SPP frequency. For small deformations, the peaks grow linearly, as could be expected from our perturbative analytical theory. For larger deformations, however, the main and the additional peak to its right compete with each other, and for large

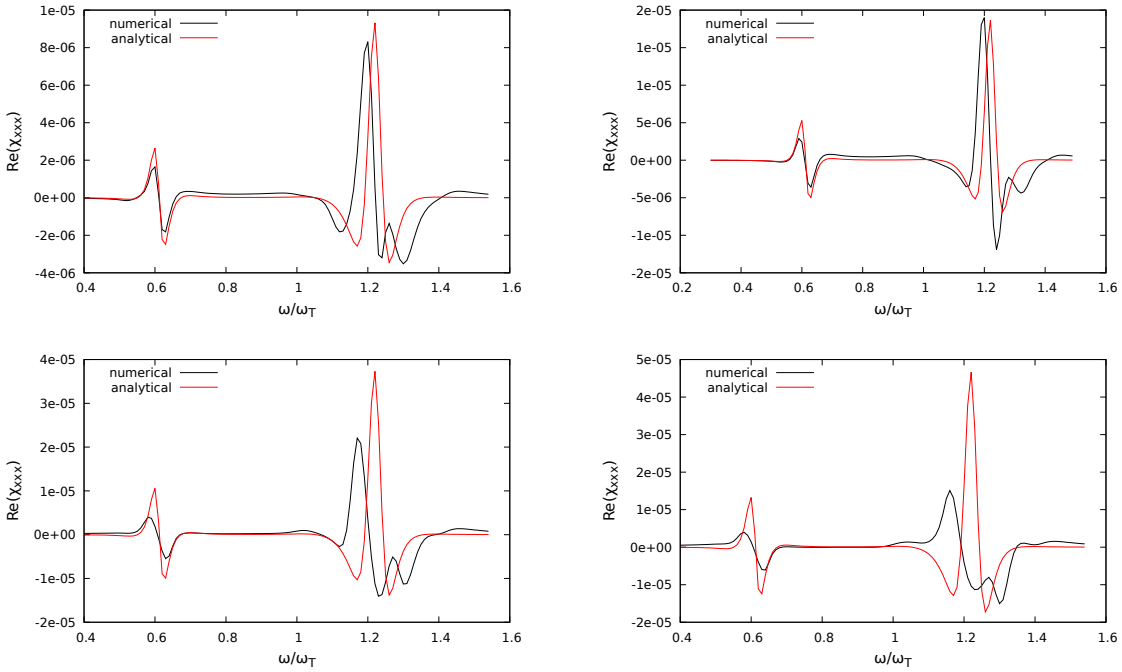

Figure 5.14: Real part of the χ_{xxx} component of the SH susceptibility tensor, as a function of the normalized frequency $\omega/\omega_{\mathrm{T}}$, for the same dielectric cylinder as in Fig. 5.6 with an abrupt interface, for different deformations. Both analytical results and the numerical one computed using our hybrid implementation are shown. The different deformation parameters are $\xi = 0.05$ (top left), $\xi = 0.1$ (top right), $\xi = 0.2$ (bottom left), and $\xi = 0.25$ (bottom right).

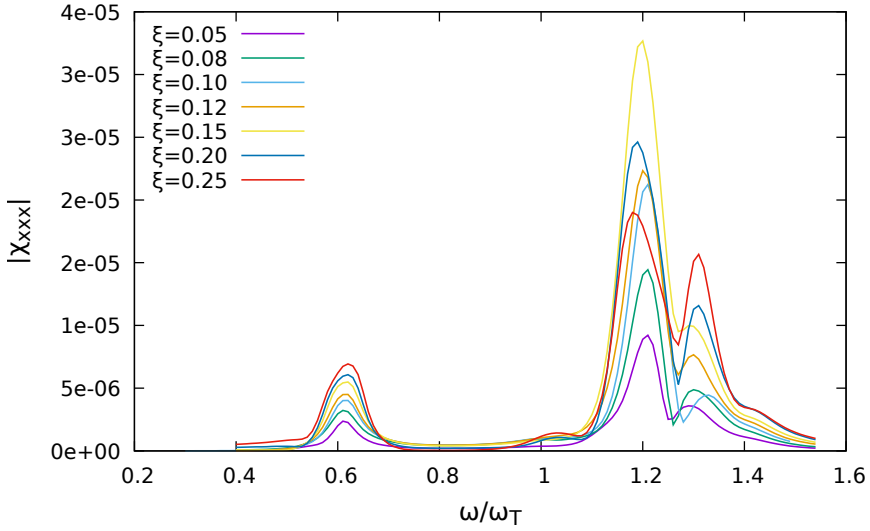

Figure 5.15: Normalized absolute value of the SH susceptibility tensor component χ_{xxx}, obtained numerically, for the same metamaterial as in Fig. 5.14 for different deformation parameters ξ.

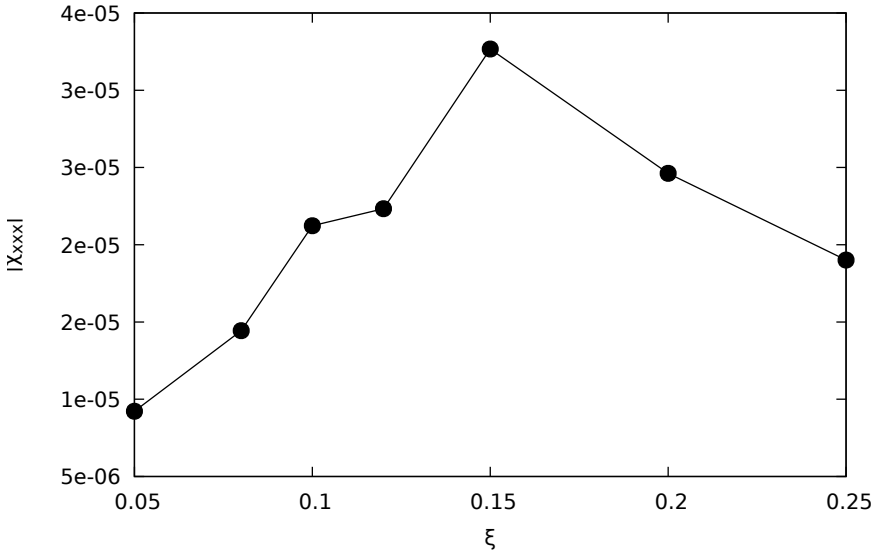

Figure 5.16: Normalized absolute value of the main peak near the SPP resonance of the SH susceptibility tensor component χ_{xxx}, shown in Fig. 5.15, as a function of the deformation parameter ξ.

enough deformations the main peak diminishes and the additional peak increases in height with increasing deformation. The variation of the peak value of the main peak at the SPP resonance as a function of the deformation is plotted in Fig. 5.16; the peak increases up to about 15% of deformation and decreases beyond this value.

5.6 Conclusions

A numerical calculation, based on an efficient homogenization technique, of the SH susceptibility tensor of a binary metamaterial formed of a periodic array of noncentrosymmetric infinitely long cylinders in vacuum was performed. The results of the computation were compared to those of the analytical approach described in Chapter 3. First, the existing modules of *Photonic* were analyzed and assessed by comparison with the analytical results for the linear microscopic fields and SH polarization and susceptibility. We identified discrepancies between the numerical and analytical calculations and we explored their origin. We found that the pixel array representation of the geometry causes deviations for curved boundaries due to the formation of steps with sharp corners at which the electric field is amplified for negative permittivities. The numerically computed linear fields could be corrected by a simple averaging procedure. Not so the SH susceptibility. Thus, we explored the SH nonlinear response of a plane surface with no steps and calculated the dimensionless parameter a which characterizes the normal component of the nonlinear surface polarization. We obtained an excellent agreement with the analytical results except in the frequency regime where the permittivity of the material is negative. Assuming that the discrepancies arose due to the

deficient representation of discontinuous fields within the numerical formalism we smoothed out the discontinuities by replacing the density of polarizable entities of the dipolium model by a slowly varying function. This attempt was succesful for frequencies for which the permittivity of the particles is positive, but failed, yielding large oscillations when it is negative, due to local singularities at the selvedge, as expected, for the electric field.

Having identified the various effects which produce discrepancies between the numerical and analytical nonlinear calculations, a novel solution was proposed, applied and validated. We used a hybrid formulation in which the spurious surface response is eliminated from the numeric calculation and replaced by its analytical counterpart, evaluated by substituting the numerically estimated linear fields in the analytical expression of the nonlinear surface polarization. We observed an outstanding improvement in the numerically estimated susceptibility, thus validating our approach. We studied the SH susceptibility tensor for a metamaterial composed of noncentrosymmetric infinitely long dielectric cylinders periodically arranged in a square lattice. We obtained, analyzed, and discussed the spectral response of the SH tensor of the metamaterial. We find remarkable agreement with the analytical results for small deformations. Deformations larger than 15% produced discrepancies, as they are beyond the validity range of our perturbative analytical calculation. On the other hand, deformations smaller than $\sim 5\%$ also yielded discrepancies, as they are too small for an accurate pixelated representation of the slightly noncentrosymmetric geometry. Thus, in the region where the geometry is well represented and the perturbation is not too large, we found agreement between the analytical and the new numerical calculation, thus validating it. Furthermore, the numerical method we developed is not restricted to $2D$ systems nor to slightly deformed cylinders in the nonretarded regime; it can be easily applied to $3D$ structures, and as the package *Photonic* also has modules for incorporating the effects of retardation, our technique can be simply extended to include systems with size comparable to the wavelength of light.

Through our study of a simple system, we accomplished our objective of validating and ensuring the reliability of a numerical technique to explore SHG from metamaterials, which can now be utilized for a vast class of systems and structures for which analytical calculations are unavailable. Other numerical techniques, such as FDTD, FEM, SIE etc., commonly employed to study the responses of nanostructures and metamaterials can now be contrasted against our method. Our analytical and numerical calculations incorporate some subtle effects, such as the screening of the the SH fields at the surface and within the particles, required to obtain a self-consistent response. Hence a comparison of our results to those of other computational techniques should prove useful to validate them or to exhibit their shortcomings. Since our numerical calculation was based in the *dipolium* model, it does suffers from its limitations at surface, such as its neglect of surface states, surface relaxation, and the change of crystal symmetry at crystalline surfaces. However, as the input to our hybrid numerical method is the nonlinear surface susceptibility, which may obtained from experiments with well characterized flat surfaces or from microscopic theories. Thus, our approach is more flexible than the previous implementation of SH calculations within the package *Photonic*,

as it allows going beyond the *dipolium* or the local jellium models for describing the interfacial response.

6 Conclusions

An investigation into the second order optical properties of nanowires and metamaterials made up of centrosymmetric materials with a simple noncentrosymmetric geometry was presented. First, an approximate analytical theory was developed to study the generation of second harmonic (SH), difference (DF) and sum (SF) frequency signals from an isolated infinitely long cylinder made of a centrosymmetric material with a noncentrosymmetric cross-section consisting of a small circle with three small protuberances separated by an angle of 120°. This is one of the most simple geometry that lacks centrosymmetry and thus can support ordinary three wave mixing processes. We assumed the nominal radius small enough so that the long wavelength approximation could be applied. Analytical expressions for the SH, SF and DF hyperpolarizabilities of dipolar and quadrupolar types were derived perturbatively using the deformation from the circle as a small perturbative parameter. We used the *dipolium* model, which assumes that the material is a continuum made up of harmonic polarizable entities that nevertheless become nonlinear when account is taken of the spatial variations of the driving field. The spectral features of the hyperpolarizabilities were identified and discussed for metallic and dielectric systems. The hyperpolarizabilities were written in terms of the geometry characterized the deformation parameter, and the linear response functions of the material at each of the frequencies involved, i.e., those of the incoming waves, their harmonics, and their sum and difference.

We also performed a derivation of the electromagnetic radiation in 2D and utilized the results to evaluate the SH, SF and DF radiated fields. The angular radiation patterns and the total power emitted were obtained and analyzed. We found that even for very small deformations the dipolar contribution, absent for circular cross sections, competes with the quadrupolar, and one or the other might dominate, depending on the frequency of the incoming light, yielding a rich variety of radiation patterns that depend on frequency and on the polarization of the incident light.

This was followed by a numerical computation of the SH response of a binary metamaterial formed of a square array of deformed cylinders as those discussed above within vacuum. We used an efficient homogenization scheme, developed by our group, to calculate the macroscopic linear response, the

microscopic fields, the nonlinear SH polarization source and the self consistent nonlinear fields and polarizations. The numerically evaluated SH susceptibility tensor was compared with the analytical one for small deformations and was found to agree well with each other for some frequency ranges but not for others. We identified the sources of the discrepancies and proposed and implemented a novel numerical scheme to overcome them. We verified the new procedures by comparing the results to those of the analytic theory in its region of validity. We were then able to perform and analyze the case of large deformations, beyond the reach of our analytical perturbative analysis. We have, thus, successfully validated our numerical technique which can now be applied to a wider category of systems. For example, $3D$ nanoparticle array with an arbitrary geometry for which analytical solutions are not available. Furthermore, the numerical calculations can be extended beyond the long wavelength approximation.

Our analytical and numerical results were based on the continuous isotropic *dipolium*, which is a convenient model that yields the local surface and bulk nonlinear susceptibilities of centrosymmetric materials in terms of their frequency dependent complex linear response. Thus, it allows readily the calculation and interpretation of the nonlinear spectral features. However, this model has some shortcomings, as it does not incorporate microscopic effects such as transitions to and from surface states, the bulk crystalline structure, the reduction of crystalline symmetry at the surfaces, surface relaxation and reconstruction. Nevertheless, our results may be simply generalized and applied to systems made of materials whose bulk and surface susceptibilities are known, having being obtained from microscopic calculations or from experiment.

In summary, we developed the theory of optical three wave mixing processes (SFG, DFG, and its limiting cases SHG and OR) from nanoparticles made of centrosymmetric materials but with a noncentrosymmetric geometry, we obtained analytical expressions for the corresponding response functions and radiated fields of particles with a particularly simple geometry, and we applied our results to calculate three wave mixing phenomena from particles made of metallic and dielectric materials. On the other hand, we tested a numerical procedure for the calculation of SHG from metamaterials through comparison with the analytical results, found its flaws and proposed, implemented and validated a novel computational scheme that overcomes them and that may be generalized to particles of arbitrary composition, size and shape. Thus, we believe that our research will prove useful for advancing the currently very active field of nonlinear nanophotonics.

A

Appendix

Electromagnetic radiation in $2D$

Most textbooks on electromagnetism discusses the theory of radiation from localized distribution of oscillating charges or current densities in $3D$, hardly mentioning the $2D$ case. Many systems such as ours possesses translational symmetry along one axis, thus reducing it to $2D$. These systems radiate electromagnetic fields confined to a plane with nature distinct from their $3D$ counterpart. This appendix is dedicated to the discussion of the theory behind the calculation of the electromagnetic fields radiated due to oscillating charges ρ and current densities $\boldsymbol{J}$ in $2D$ varying sinusoidally in time,

$$\boldsymbol{J}(\boldsymbol{r},t) = \boldsymbol{J}(\boldsymbol{r})e^{-i\omega t}, \tag{A.1}$$

$$\boldsymbol{\rho}(\boldsymbol{r},t) = \boldsymbol{\rho}(\boldsymbol{r})e^{-i\omega t}, \tag{A.2}$$

where $\boldsymbol{r}$ is the $2D$ position vector. We restrict ourselves to small radiating systems and demonstrate the contributions to the radiated fields only from the first multipoles, namely, the electric dipole, magnetic dipole, and electric quadrupole. The treatment is predominantly similar to that of $3D$; the essential difference between them being in the Green's function for the wave equation.

In the Lorentz gauge, the vector potential is also monochromatic and obeys the wave equation

$$\nabla^2\boldsymbol{A} - \frac{1}{c^2}\frac{\partial^2}{\partial t^2}\boldsymbol{A} = \nabla^2\boldsymbol{A} + k^2\boldsymbol{A} = -\frac{4\pi}{c}\boldsymbol{J}, \tag{A.3}$$

where $k = \omega/c$. Once the above equation is solved to obtain the vector potential for a certain

current distribution, the electromagnetic fields in the radiation zone are then given by

$$\boldsymbol{B} = \boldsymbol{\nabla} \times \boldsymbol{A}, \tag{A.4}$$

$$\boldsymbol{E} = \frac{i}{k} \boldsymbol{\nabla} \times \boldsymbol{B}. \tag{A.5}$$

To solve Equation (A.3) we first find its corresponding Green's function in $2D$ $G(\boldsymbol{r}, \boldsymbol{r}') = G(\boldsymbol{r} - \boldsymbol{r}')$, which obeys

$$(\nabla^2 + k^2) G(\boldsymbol{r}) = -4\pi\delta(\boldsymbol{r}), \tag{A.6}$$

where we assumed translational symmetry. As space is isotropic, we impose isotropic outgoing boundary conditions and assume that the Green's function depends only on distance and not on direction. Thus, we write $G(\boldsymbol{r}) = R(kr)$ and look for the radial function $R(kr)$. For $r \neq 0$, the above equation can be written in termos of the dimensionless variable $s \equiv kr$ as

$$s^2 \frac{d^2}{ds^2} R(s) + s \frac{d}{ds} R(s) + s^2 R(s) = 0, \tag{A.7}$$

whose outoing solution is proportional to the Hankel function $H_0^{(1)}(s) = J_0^{(1)}(s) + iY_0^{(1)}(s)$, which in the near zone, $(s \to 0)$, takes the form

$$\lim_{s \to 0} H_0^{(1)}(s) = 2i \ln(s)/\pi. \tag{A.8}$$

As the nonretarded Green's function in 2D is $G = -2\ln(r) + \text{constant}$, i.e., the scalar potential of a line with unit charge per unit length, a comparison with Eq. (A.8) yields

$$G(\boldsymbol{r}) = i\pi H_0^{(1)}(kr). \tag{A.9}$$

Thus, using the asymptotic expression for the Hankel's function for large arguments, we obtain

$$G(\boldsymbol{r}) = e^{i\pi/4} \sqrt{\frac{2\pi}{kr}} e^{ikr}, \tag{A.10}$$

in the radiation zone $(kr \to \infty)$, where the retarded vector potential becomes

$$\boldsymbol{A}(\boldsymbol{r}) = \frac{1}{c} \int d^2r'\, G(\boldsymbol{r} - \boldsymbol{r}') \boldsymbol{J}(\boldsymbol{r}') = \frac{1}{c} \int d^2r'\, e^{i\pi/4} \sqrt{\frac{2\pi}{k|\boldsymbol{r} - \boldsymbol{r}'|}} e^{ik|\boldsymbol{r} - \boldsymbol{r}'|} \boldsymbol{J}(\boldsymbol{r}'). \tag{A.11}$$

Note, that in the radiation zone $(kr >> 1)$ the exponential within the integral of Eq. (A.11) oscillates rapidly. For a localized source we may assume $r \gg r'$ and in the long-wavelength approximatino $kr' \ll 1$ we can further approximate Eq. (A.11) by

$$\lim_{kr \to \infty} \boldsymbol{A}(\boldsymbol{r}) = \frac{1}{c} \sqrt{\frac{2\pi}{kr}} e^{i\pi/4} e^{ikr} \int d^2r' \boldsymbol{J}(\boldsymbol{r'}) e^{-ik\,\hat{\boldsymbol{n}} \cdot \boldsymbol{r'}}, \tag{A.12}$$

where $\hat{\boldsymbol{n}}$ is the unit vector in the direction of $\boldsymbol{r}$. Here, we have used the approximation $|\boldsymbol{r}-\boldsymbol{r'}| \cong r - \hat{\boldsymbol{n}}\cdot\boldsymbol{r'}$ in the exponential, while we replaced $|\boldsymbol{r}-\boldsymbol{r'}|$ by r in the relatively slowly varying denominator.

We further Taylor expand the exponential within the integral, yielding a multipolar series, each of whose terms may be integrated separately to obtain different multipolar contributions to radiation, in analogy to the $3D$ case. Thus, Eq. (A.12) is written as

$$\lim_{kr\to\infty} \boldsymbol{A}(\boldsymbol{r}) = \frac{1}{c}\sqrt{\frac{2\pi}{kr}} e^{i\pi/4} e^{ikr} \int d^2r' \boldsymbol{J}(\boldsymbol{r'}) \sum_{m=0} \frac{(-ik)^m}{m!} (\hat{\boldsymbol{n}}\cdot\boldsymbol{r'})^m. \tag{A.13}$$

Electric Dipole Radiation

Considering the first term ($m = 0$) in the series (Eq. (A.13)),

$$\boldsymbol{A}^{(0)}(\boldsymbol{r}) = \frac{1}{c}\sqrt{\frac{2\pi}{kr}} e^{i\pi/4} e^{ikr} \int d^2r' \boldsymbol{J}(\boldsymbol{r'}), \tag{A.14}$$

one can obtain the dipolar contribution to the vector potential. The integration in Eq. (A.14) can be performed by using the following tricks as illustrated for its $x-$th component,

$$\int d^2r' J_x(\boldsymbol{r'}) = \int d^2r' \boldsymbol{J}(\boldsymbol{r'})\cdot\hat{\boldsymbol{x}}', \tag{A.15a}$$

$$= \int d^2r' \boldsymbol{J}(\boldsymbol{r'})\cdot\nabla' x', \tag{A.15b}$$

$$= \int d^2r' \{[\nabla'\cdot\boldsymbol{J}(\boldsymbol{r'})\, x'] - [\nabla'\cdot\boldsymbol{J}(\boldsymbol{r'})]\, x'\}, \tag{A.15c}$$

$$= \oint ds' \boldsymbol{J}(\boldsymbol{r'})\cdot\hat{\boldsymbol{n}}'\, x' - \int d^2r' [\nabla'\cdot\boldsymbol{J}(\boldsymbol{r'})]\, x', \tag{A.15d}$$

where we used the divergence theorem in Eq. (A.15d). Since no current passes through the surface bounding the entire source, its first term integrates to zero. Using the continuity equation $\nabla\cdot\boldsymbol{J}(\boldsymbol{r},t) = -\partial\rho(\boldsymbol{r},t)/\partial t$ and Eq. (A.2) for its second term, we get

$$\int d^2r' J_x(\boldsymbol{r'}) = \int d^2r' \frac{\partial\rho(\boldsymbol{r'},t)}{\partial t}\, x' = -i\omega \int d^2r' \rho(\boldsymbol{r'})\, x'. \tag{A.16}$$

Hence,

$$\int d^2r' \boldsymbol{J}(\boldsymbol{r'}) = -i\omega \int d^2r' \rho(\boldsymbol{r'})\, \boldsymbol{r'}. \tag{A.17}$$

Identifying the amplitude of the dipole moment per unit length $\boldsymbol{p} = \int d^2r\rho(\boldsymbol{r})\boldsymbol{r}$, we get

$$\int d^2r \boldsymbol{J}(\boldsymbol{r}) = -i\omega\boldsymbol{p}. \tag{A.18}$$

Finally, substituting Eq. (A.18) in Eq. (A.14) we obtain the vector potential radiated by an oscillating dipole,

$$\boldsymbol{A}^{(0)}(\boldsymbol{r}) = (-ie^{i\pi/4})\sqrt{2\pi}\sqrt{\frac{k}{r}}e^{ikr}\boldsymbol{p}. \tag{A.19}$$

Using Eqs. (A.4), (A.5) and (A.19), the expressions for the electromagnetic fields radiated by a dipole are,

$$\boldsymbol{B}(\boldsymbol{r}) = (\sqrt{2\pi}e^{i\pi/4})\frac{k^{3/2}}{\sqrt{r}}e^{ikr}(\hat{\boldsymbol{n}}\times\boldsymbol{p}), \tag{A.20}$$

$$\boldsymbol{E}(\boldsymbol{r}) = (\sqrt{2\pi}e^{i\pi/4})\frac{k^{3/2}}{\sqrt{r}}e^{ikr}[(\hat{\boldsymbol{n}}\times\boldsymbol{p})\times\hat{\boldsymbol{n}}]. \tag{A.21}$$

We must point out that we used the relation, $\nabla \to ik\hat{\boldsymbol{n}}$, to calculate the fields. This relation holds true in the radiation zone.

Electric Quadrupole Radiation

The next order of approximation corresponds to the second term in the expansion in Eq. (A.13)

$$\boldsymbol{A}^{(1)}(\boldsymbol{r}) = \frac{1}{c}\sqrt{\frac{2\pi}{kr}}e^{i\pi/4}e^{ikr}(-ik)\int d^2r'\boldsymbol{J}(\boldsymbol{r'})(\hat{\boldsymbol{n}}\cdot\boldsymbol{r'}). \tag{A.22}$$

The integrand in the above equation can be written as the sum of a symmetric and an antisymmetric part

$$\begin{aligned}\boldsymbol{A}^{(1)}(\boldsymbol{r}) =& \frac{1}{c}\sqrt{\frac{2\pi}{kr}}e^{i\pi/4}e^{ikr}\times \\ & (-ik)\int d^2r'\frac{1}{2}[\underbrace{\boldsymbol{J}(\boldsymbol{r'})(\hat{\boldsymbol{n}}\cdot\boldsymbol{r'})+\boldsymbol{r'}(\hat{\boldsymbol{n}}\cdot\boldsymbol{J}(\boldsymbol{r'}))}_{\text{Symmetric}}+\underbrace{\boldsymbol{J}(\boldsymbol{r'})(\hat{\boldsymbol{n}}\cdot\boldsymbol{r'})-\boldsymbol{r'}(\hat{\boldsymbol{n}}\cdot\boldsymbol{J}(\boldsymbol{r'}))}_{\text{Anti-symmetric}}].\end{aligned} \tag{A.23}$$

We begin by choosing the x component of the first term of the symmetric part,

$$\int d^2r'J_x(\boldsymbol{r'})(\hat{\boldsymbol{n}}\cdot\hat{\boldsymbol{r}'}) = \int d^2r'(\hat{\boldsymbol{n}}\cdot\hat{\boldsymbol{r}'})\,\boldsymbol{J}(\boldsymbol{r'})\cdot\hat{\boldsymbol{x}'}, \tag{A.24}$$

$$= \int d^2r'(\hat{\boldsymbol{n}}\cdot\hat{\boldsymbol{r}'})\,\boldsymbol{J}(\boldsymbol{r'})\cdot\nabla' x', \tag{A.25}$$

$$= \int d^2r'\nabla'\cdot\{(\hat{\boldsymbol{n}}\cdot\hat{\boldsymbol{r}'})\,\boldsymbol{J}(\boldsymbol{r'})\,x'\} - \int d^2r'x'\,\nabla'\cdot\{(\hat{\boldsymbol{n}}\cdot\hat{\boldsymbol{r}'})\,\boldsymbol{J}(\boldsymbol{r'})\}, \tag{A.26}$$

$$= -\int d^2r'x'\,\nabla'\cdot\{(\hat{\boldsymbol{n}}\cdot\hat{\boldsymbol{r}'})\,\boldsymbol{J}(\boldsymbol{r'})\}, \tag{A.27}$$

where the first term in Eq. (A.26) integrates to zero using the divergence theorem, as discussed

above. We continue from Eq. (A.27),

$$\int d^2r' J_x(\boldsymbol{r}')(\hat{\boldsymbol{n}}\cdot\hat{\boldsymbol{r}}') = -\int d^2r' x' \,(\nabla'\cdot\boldsymbol{J}(\boldsymbol{r}'))(\hat{\boldsymbol{n}}\cdot\hat{\boldsymbol{r}}') - \int d^2r' x'\, \boldsymbol{J}(\boldsymbol{r}')\cdot\nabla'(\hat{\boldsymbol{n}}\cdot\hat{\boldsymbol{r}}'), \tag{A.28}$$

$$= -\int d^2r' x' \,(\nabla'\cdot\boldsymbol{J}(\boldsymbol{r}'))(\hat{\boldsymbol{n}}\cdot\hat{\boldsymbol{r}}') - \int d^2r' x'\, \boldsymbol{J}(\boldsymbol{r}')\cdot\hat{\boldsymbol{n}}. \tag{A.29}$$

Thus,

$$\int d^2r' J_x(\boldsymbol{r}')(\hat{\boldsymbol{n}}\cdot\hat{\boldsymbol{r}}') + \int d^2r' x'\, \boldsymbol{J}(\boldsymbol{r}')\cdot\hat{\boldsymbol{n}} = -\int d^2r' x' \,(\nabla'\cdot\boldsymbol{J}(\boldsymbol{r}'))(\hat{\boldsymbol{n}}\cdot\hat{\boldsymbol{r}}'), \tag{A.30}$$

Eq. (A.30) represents the x component of the symmetric part of the integral of Eq. (A.23). Hence the full vector form can be written as

$$\int d^2r' \boldsymbol{J}(\boldsymbol{r}')(\hat{\boldsymbol{n}}\cdot\hat{\boldsymbol{r}}') + \int d^2r' \boldsymbol{r}' \,(\boldsymbol{J}(\boldsymbol{r}')\cdot\hat{\boldsymbol{n}}) = -\int d^2r' \boldsymbol{r}' \,(\nabla'\cdot\boldsymbol{J}(\boldsymbol{r}'))(\hat{\boldsymbol{n}}\cdot\hat{\boldsymbol{r}}'). \tag{A.31}$$

Substituting the equation of continuity in Eq. (A.31) and using Eq. (A.2), we get

$$\int d^2r' \boldsymbol{J}(\boldsymbol{r}')(\hat{\boldsymbol{n}}\cdot\hat{\boldsymbol{r}}') + \int d^2r' \boldsymbol{r}' \,(\boldsymbol{J}(\boldsymbol{r}')\cdot\hat{\boldsymbol{n}}) = +\int d^2r' \boldsymbol{r}' \,\frac{\partial\rho(\boldsymbol{r}',t)}{\partial t}(\hat{\boldsymbol{n}}\cdot\hat{\boldsymbol{r}}'), \tag{A.32}$$

$$\int d^2r' \boldsymbol{J}(\boldsymbol{r}')(\hat{\boldsymbol{n}}\cdot\hat{\boldsymbol{r}}') + \int d^2r' \boldsymbol{r}' \,(\boldsymbol{J}(\boldsymbol{r}')\cdot\hat{\boldsymbol{n}}) = -i\omega \int d^2r' \boldsymbol{r}' \,\rho(\boldsymbol{r}')(\hat{\boldsymbol{n}}\cdot\hat{\boldsymbol{r}}'), \tag{A.33}$$

Subsituting Eq. (A.33) in Eq. (A.23) and writting only the symmetric part, we obtain

$$\boldsymbol{A}_{\mathrm{s}}^{(1)}(\boldsymbol{r}) = -(\sqrt{2\pi}e^{i\pi/4})\frac{e^{ikr}}{2\sqrt{r}}k^{3/2}\int d^2r' \boldsymbol{r}'(\hat{\boldsymbol{n}}\cdot\boldsymbol{r}')\rho(\boldsymbol{r}'). \tag{A.34}$$

Since we defined the quadrupole moment in $2D$ by

$$\boldsymbol{Q} = \int d^2r' \rho(\boldsymbol{r}')(2\boldsymbol{r}'\boldsymbol{r}' - r'^2), \tag{A.35}$$

we rewrite the integral in Eq. (A.34) as

$$\int d^2r' \boldsymbol{r}'(\hat{\boldsymbol{n}}\cdot\boldsymbol{r}')\rho(\boldsymbol{r}') = \frac{1}{2}\int d^2r' \rho(\boldsymbol{r}')(2\boldsymbol{r}'(\hat{\boldsymbol{n}}\cdot\boldsymbol{r}') - \hat{\boldsymbol{n}}r'^2 + \hat{\boldsymbol{n}}r'^2), \tag{A.36}$$

where we identify the quadrupolar tensor to write

$$\boldsymbol{A}_{\mathrm{s}}^{(1)}(\boldsymbol{r}) = -(\sqrt{2\pi}e^{i\pi/4})\frac{e^{ikr}}{2\sqrt{r}}k^{3/2}\left\{\boldsymbol{Q}(\hat{\boldsymbol{n}}) + \frac{1}{2}\int d^2r' \rho(\boldsymbol{r}')\,\hat{\boldsymbol{n}}\,r'^2\right\}, \tag{A.37}$$

where $\boldsymbol{Q}(\hat{\boldsymbol{n}}) = \boldsymbol{Q}\cdot\hat{\boldsymbol{n}}$ is a vector related to the quadrupole moment $\boldsymbol{Q}$ of the charge distribution. The additional term in Eq. (A.37) is radial and thus doesn't contribute to the transverse radiated

fields and may be safely ignored. The $\boldsymbol{B}$ field due to the vector potential in Eq. (A.37) is given by

$$\boldsymbol{B}(\boldsymbol{r}) = (-i\sqrt{2\pi}e^{i\pi/4})\frac{e^{ikr}}{4\sqrt{r}}k^{5/2}\{\hat{\boldsymbol{n}} \times \boldsymbol{Q}(\hat{\boldsymbol{n}})\} \tag{A.38}$$

and the $\boldsymbol{E}$ by

$$\boldsymbol{E}(\boldsymbol{r}) = (-i\sqrt{2\pi}e^{i\pi/4})\frac{e^{ikr}}{4\sqrt{r}}k^{5/2}[\{\hat{\boldsymbol{n}} \times \boldsymbol{Q}(\hat{\boldsymbol{n}})\} \times \hat{\boldsymbol{n}}]. \tag{A.39}$$

We reiterate that we used the relation $\nabla \rightarrow ik\hat{\boldsymbol{n}}$ to calculate the fields in the radiation zone as discussed in the dipolar case.

Magnetic Dipole Radiation

Choosing the anti-symmetric part of Eq. (A.23), we have

$$\boldsymbol{A}^{(1)}_{\text{as}}(\boldsymbol{r}) = \frac{1}{c}\sqrt{\frac{2\pi}{kr}}e^{i\pi/4}e^{ikr}(-ik)\frac{1}{2}\int d^2r'\{\boldsymbol{J}(\boldsymbol{r'})(\hat{\boldsymbol{n}} \cdot \boldsymbol{r'}) - \boldsymbol{r'}(\hat{\boldsymbol{n}} \cdot \boldsymbol{J}(\boldsymbol{r'})\}), \tag{A.40}$$

which can be written as

$$\boldsymbol{A}^{(1)}_{\text{as}}(\boldsymbol{r}) = \frac{1}{c}\sqrt{\frac{2\pi}{kr}}e^{i\pi/4}e^{ikr}(-ik)\hat{\boldsymbol{n}} \times \int d^2r'\frac{1}{2}[\boldsymbol{J}(\boldsymbol{r'}) \times \boldsymbol{r'}]. \tag{A.41}$$

The magnetic dipole moment $\boldsymbol{m}$ is defined as,

$$\boldsymbol{m} = \frac{1}{2c}\int d^2r'\{\boldsymbol{r'} \times \boldsymbol{J}(\boldsymbol{r'})\}. \tag{A.42}$$

Substituting Eq. (A.42) in Eq. (A.41), we get

$$\boldsymbol{A}^{(1)}_{\text{as}}(\boldsymbol{r}) = \sqrt{\frac{2\pi}{kr}}e^{i\pi/4}e^{ikr}(ik)[\hat{\boldsymbol{n}} \times \boldsymbol{m}]. \tag{A.43}$$

The electromagnetic fields radiated by a magnetic dipole are then evaluated following the same procedure as of the electric dipole or electric quadrupole. We obtain

$$\boldsymbol{B}(\boldsymbol{r}) = -(\sqrt{2\pi}e^{i\pi/4})\frac{k^{3/2}}{\sqrt{r}}e^{ikr}[\hat{\boldsymbol{n}} \times (\hat{\boldsymbol{n}} \times \boldsymbol{m})], \tag{A.44}$$

$$\boldsymbol{E}(\boldsymbol{r}) = -(\sqrt{2\pi}e^{i\pi/4})\frac{k^{3/2}}{\sqrt{r}}e^{ikr}[\hat{\boldsymbol{n}} \times \boldsymbol{m}]. \tag{A.45}$$

Bibliography

[1] Daria Smirnova and Yuri S. Kivshar. Multipolar nonlinear nanophotonics. *Optica*, 3(11):1241–1255, Nov 2016.

[2] Martti Kauranen and Anatoly V. Zayats. Nonlinear plasmonics. *Nature Photonics*, 6:737–748, 2012.

[3] Yu-xi Zhang and Yu-hua Wang. Nonlinear optical properties of metal nanoparticles: A review. *RSC Adv.*, 7:45129–45144, 2017.

[4] Kevin O'Brien, Haim Suchowski, Junsuk Rho, Alessandro Salandrino, Boubacar Kante, Xiaobo Yin, and Xiang Zhang. Predicting nonlinear properties of metamaterials from the linear response. *Nature Materials*, 14(4):379–383, Apr 2015.

[5] Matthias W. Klein, Martin Wegener, Nils Feth, and Stefan Linden. Experiments on second- and third-harmonic generation from magnetic metamaterials. *Opt. Express*, 15(8):5238–5247, Apr 2007.

[6] Guixin Li, Shuang Zhang, and Thomas Zentgraf. Nonlinear photonic metasurfaces. *Nature Reviews Materials*, 2(5):17010, Mar 2017.

[7] Thomas Pertsch and Yuri Kivshar. Nonlinear optics with resonant metasurfaces. *MRS Bulletin*, 45(3):210–220, 2020.

[8] Pete Vukusic and J. Roy Sambles. Photonic structures in biology. *Nature*, 424(6950):852–855, 2003.

[9] M. A. Giraldo and D. G. Stavenga. Brilliant iridescence of morpho butterfly wing scales is due to both a thin film lower lamina and a multilayered upper lamina. *Journal of comparative physiology. A, Neuroethology, sensory, neural, and behavioral physiology*, 202(5):381–388, May 2016.

[10] Joanna Aizenberg, Alexei Tkachenko, Steve Weiner, Lia Addadi, and Gordon Hendler. Calcitic microlenses as part of the photoreceptor system in brittlestars. *Nature*, 412(6849):819–822, Aug 2001.

[11] Ian Freestone, Nigel Meeks, Margaret Sax, and Catherine Higgitt. The lycurgus cup – a roman nanotechnology. *Gold Bulletin*, 40(4):270–277, 2007.

[12] N. Brun, L. Mazerolles, and M. Pernot. Microstructure of opaque red glass containing copper. *Journal of Materials Science Letters*, 10(23):1418–1420, 1991.

[13] Sofía Pérez-Villar, Juan Rubio, and Jose Luis Oteo. Study of color and structural changes in silver painted medieval glasses. *Journal of Non-Crystalline Solids*, 354(17):1833 – 1844, 2008.

[14] Philippe Sciau. Nanoparticles in ancient materials: The metallic lustre decorations of medieval ceramics. In Abbass A. Hashim, editor, *The Delivery of Nanoparticles*, chapter 25. IntechOpen, Rijeka, 2012.

[15] Philip Ball. Renaissance potters were nanotechnologists. *Nature*, 2003.

[16] Sinjeung Park, Jae W. Hahn, and Jae Yong Lee. Doubly resonant metallic nanostructure for high conversion efficiency of second harmonic generation. *Opt. Express*, 20(5):4856–4870, Feb 2012.

[17] Alexandre Baron, Stéphane Larouche, Daniel J. Gauthier, and David R. Smith. Scaling of the nonlinear response of the surface plasmon polariton at a metal/dielectric interface. *J. Opt. Soc. Am. B*, 32(1):9–14, Jan 2015.

[18] P Zijlstra and M Orrit. Single metal nanoparticles: optical detection, spectroscopy and applications. *Reports on Progress in Physics*, 74(10):106401, sep 2011.

[19] Jérémy Butet, Pierre-François Brevet, and Olivier J. F. Martin. Optical second harmonic generation in plasmonic nanostructures: From fundamental principles to advanced applications. *ACS Nano*, 9(11):10545–10562, Nov 2015.

[20] Robert Czaplicki, Jouni Mäkitalo, Roope Siikanen, Hannu Husu, Joonas Lehtolahti, Markku Kuittinen, and Martti Kauranen. Second-harmonic generation from metal nanoparticles: Resonance enhancement versus particle geometry. *Nano Letters*, 15(1):530–534, 2015. PMID: 25521745.

[21] Guillaume Bachelier, Isabelle Russier-Antoine, Emmanuel Benichou, Christian Jonin, and Pierre-François Brevet. Multipolar second-harmonic generation in noble metal nanoparticles. *J. Opt. Soc. Am. B*, 25(6):955–960, Jun 2008.

[22] Raksha Singla and W. Luis Mochán. Analytical theory of second harmonic generation from a nanowire with noncentrosymmetric geometry. *Phys. Rev. B*, 99:125418, Mar 2019.

[23] Yun-Hang Qiu, Si-Jing Ding, Yong-Jie Lin, Kai Chen, Da-Jie Yang, Song Ma, Xiaoguang Li, Hai-qing Lin, Jianfang Wang, and Qu-Quan Wang. Growth of au hollow stars and harmonic excitation energy transfer. *ACS Nano*, 14(1):736–745, Jan 2020.

[24] Robert Czaplicki, Antti Kiviniemi, Mikko J. Huttunen, Xiaorun Zang, Timo Stolt, Ismo Vartiainen, Jérémy Butet, Markku Kuittinen, Olivier J. F. Martin, and Martti Kauranen. Less is more: Enhancement of second-harmonic generation from metasurfaces by reduced nanoparticle density. *Nano Letters*, 18(12):7709–7714, 2018. PMID: 30423245.

[25] Isabelle Russier-Antoine, Hye Jin Lee, Alastair W. Wark, Jérémy Butet, Emmanuel Benichou, Christian Jonin, Olivier J. F. Martin, and Pierre-François Brevet. Second harmonic scattering from silver nanocubes. *The Journal of Physical Chemistry C*, 122(30):17447–17455, Aug 2018.

[26] Bruno Majérus, Jérémy Butet, Gabriel D. Bernasconi, Raziman Thottungal Valapu, Michaël Lobet, Luc Henrard, and Oliver J. F. Martin. Optical second harmonic generation from nanostructured graphene: a full wave approach. *Opt. Express*, 25(22):27015–27027, Oct 2017.

[27] Brian K. Canfield, Hannu Husu, Janne Laukkanen, Benfeng Bai, Markku Kuittinen, Jari Turunen, and Martti Kauranen. Local field asymmetry drives second-harmonic generation in noncentrosymmetric nanodimers. *Nano Letters*, 7(5):1251–1255, 2007.

[28] J. Butet, G. Bachelier, I. Russier-Antoine, F. Bertorelle, A. Mosset, N. Lascoux, C. Jonin, E. Benichou, and P.-F. Brevet. Nonlinear fano profiles in the optical second-harmonic generation from silver nanoparticles. *Phys. Rev. B*, 86:075430, Aug 2012.

[29] W. L. Schaich. Second harmonic generation by periodically-structured metal surfaces. *Phys. Rev. B*, 78:195416, Nov 2008.

[30] Renlong Zhou, Hua Lu, Xueming Liu, Yongkang Gong, and Dong Mao. Second-harmonic generation from a periodic array of noncentrosymmetric nanoholes. *J. Opt. Soc. Am. B*, 27(11):2405–2409, Nov 2010.

[31] Carlo Forestiere, Antonio Capretti, and Giovanni Miano. Surface integral method for second harmonic generation in metal nanoparticles including both local-surface and nonlocal-bulk sources. *J. Opt. Soc. Am. B*, 30(9):2355–2364, Sep 2013.

[32] Lei Zhang, Shifei Tao, Zhenhong Fan, and Rushan Chen. Efficient method for evaluation of second-harmonic generation by surface integral equation. *Opt. Express*, 25(23):28010–28021, Nov 2017.

[33] Jérémy Butet, Benjamin Gallinet, Krishnan Thyagarajan, and Olivier J. F. Martin. Second-harmonic generation from periodic arrays of arbitrary shape plasmonic nanostructures: A surface integral approach. *J. Opt. Soc. Am. B*, 30(11):2970–2979, Nov 2013.

[34] Naveen K. Balla, Peter T. C. So, and Colin J. R. Sheppard. Second harmonic scattering from small particles using discrete dipole approximation. *Opt. Express*, 18(21):21603–21611, Oct 2010.

[35] Denis G. Baranov, Dmitry A. Zuev, Sergey I. Lepeshov, Oleg V. Kotov, Alexander E. Krasnok, Andrey B. Evlyukhin, and Boris N. Chichkov. All-dielectric nanophotonics: the quest for better materials and fabrication techniques. *Optica*, 4(7):814–825, Jul 2017.

[36] Yuri Kivshar. All-dielectric meta-optics and non-linear nanophotonics. *National Science Review*, 5(2):144–158, 01 2018.

[37] Isabelle Staude and Jörg Schilling. Metamaterial-inspired silicon nanophotonics. *Nature Photonics*, 11(5):274–284, May 2017.

[38] Sheng Liu, Michael B. Sinclair, Sina Saravi, Gordon A. Keeler, Yuanmu Yang, John Reno, Gregory M. Peake, Frank Setzpfandt, Isabelle Staude, Thomas Pertsch, and Igal Brener. Resonantly enhanced second-harmonic generation using iii–v semiconductor all-dielectric metasurfaces. *Nano Letters*, 16(9):5426–5432, Sep 2016.

[39] Kun-Ching Shen, Yi-Teng Huang, Tsung Lin Chung, Ming Lun Tseng, Wei-Yi Tsai, Greg Sun, and Din Ping Tsai. Giant efficiency of visible second-harmonic light by an all-dielectric multiple-quantum-well metasurface. *Phys. Rev. Applied*, 12:064056, Dec 2019.

[40] Tao Zeng, Ling Guo, Long Xu, and Tiancheng Han. Enhanced second-harmonic generation from l-shaped algaas nanoantennas. *J. Opt. Soc. Am. B*, 37(3):868–875, Mar 2020.

[41] Luca Carletti, Andrea Locatelli, Dragomir Neshev, and Costantino De Angelis. Shaping the radiation pattern of second-harmonic generation from algaas dielectric nanoantennas. *ACS Photonics*, 3(8):1500–1507, Aug 2016.

[42] Churong Ma, Jiahao Yan, Yuming Wei, Pu Liu, and Guowei Yang. Enhanced second harmonic generation in individual barium titanate nanoparticles driven by mie resonances. *J. Mater. Chem. C*, 5:4810–4819, 2017.

[43] Elizaveta V. Melik-Gaykazyan, Kirill Koshelev, Jae-Hyuck Choi, Sergey Kruk, Hong-Gyu Park, and Yuri Kivshar. Second-harmonic spectroscopy with structured beams and the observation of quasi-BIC modes in all-dielectric nanoresonators. In Arnan Mitchell and Halina Rubinsztein-Dunlop, editors, *AOS Australian Conference on Optical Fibre Technology (ACOFT) and Australian Conference on Optics, Lasers, and Spectroscopy (ACOLS) 2019*, volume 11200, pages 1 – 2. International Society for Optics and Photonics, SPIE, 2019.

[44] Miguel A. G. Mandujano, Eugenio R. Méndez, Claudio I. Valencia, and Bernardo S. Mendoza. Multipolar analysis of the second harmonic generated by dielectric particles. *Opt. Express*, 27(3):3337–3353, Feb 2019.

[45] A. V. Ovchinnikov, O. V. Chefonov, E. D. Mishina, and M. B. Agranat. Second harmonic generation in the bulk of silicon induced by an electric field of a high power terahertz pulse. *Scientific Reports*, 9(1):9753, Jul 2019.

[46] Claudio Castellan, Alessandro Trenti, Chiara Vecchi, Alessandro Marchesini, Mattia Mancinelli, Mher Ghulinyan, Georg Pucker, and Lorenzo Pavesi. On the origin of second harmonic generation in silicon waveguides with silicon nitride cladding. *Scientific Reports*, 9(1):1088, Jan 2019.

[47] Xiyuan Lu, Gregory Moille, Ashutosh Rao, Daron Westly, and Kartik Srinivasan. Efficient photo-induced second harmonic generation in silicon photonics. *arXiv e-prints*, page arXiv:2003.12176, March 2020.

[48] Yu Zhang, Di Huang, Yuwei Shan, Tao Jiang, Zhihong Zhang, Kaihui Liu, Lei Shi, Jinluo Cheng, John E. Sipe, Wei-Tao Liu, and Shiwei Wu. Doping-induced second-harmonic generation in centrosymmetric graphene from quadrupole response. *Phys. Rev. Lett.*, 122:047401, Jan 2019.

[49] Jerry I. Dadap, Jie Shan, and Tony F. Heinz. Theory of optical second-harmonic generation from a sphere of centrosymmetric material: Small-particle limit. *J. Opt. Soc. Am. B*, 21(7):1328–1347, Jul 2004.

[50] Alex G. F. de Beer and Sylvie Roke. Nonlinear mie theory for second-harmonic and sum-frequency scattering. *Phys. Rev. B*, 79:155420, Apr 2009.

[51] Vera L. Brudny, Bernardo S. Mendoza, and W. Luis Mochán. Second-harmonic generation from spherical particles. *Phys. Rev. B*, 62:11152–11162, Oct 2000.

[52] W. Luis Mochán, Jesús A. Maytorena, Bernardo S. Mendoza, and Vera L. Brudny. Second-harmonic generation in arrays of spherical particles. *Phys. Rev. B*, 68:085318, Aug 2003.

[53] Claudio I. Valencia, Eugenio R. Méndez, and Bernardo S. Mendoza. Second-harmonic generation in the scattering of light by an infinite cylinder. *J. Opt. Soc. Am. B*, 21(1):36–44, Jan 2004.

[54] Jerry Icban Dadap. Optical second-harmonic scattering from cylindrical particles. *Phys. Rev. B*, 78:205322, Nov 2008.

[55] C. G. Biris and N. C. Panoiu. Second harmonic generation in metamaterials based on homogeneous centrosymmetric nanowires. *Phys. Rev. B*, 81:195102, May 2010.

[56] Olivier Pluchery, Christophe Humbert, Mehrnoush Valamanesh, Emmanuelle Lacaze, and Bertrand Busson. Enhanced detection of thiophenol adsorbed on gold nanoparticles by sfg and dfg nonlinear optical spectroscopy. *Phys. Chem. Chem. Phys.*, 11:7729–7737, 2009.

[57] Jie-Yun Yan, Wei Zhang, Suqing Duan, and Xian-Geng Zhao. Plasmon-enhanced midinfrared generation from difference frequency in semiconductor quantum dots. *Journal of Applied Physics*, 103(10):104314, 2008.

[58] Uday K. Chettiar and Nader Engheta. Optical frequency mixing through nanoantenna enhanced difference frequency generation: Metatronic mixer. *Phys. Rev. B*, 86:075405, Aug 2012.

[59] Mikko J. Huttunen, Payman Rasekh, Robert W. Boyd, and Ksenia Dolgaleva. Using surface lattice resonances to engineer nonlinear optical processes in metal nanoparticle arrays. *Phys. Rev. A*, 97:053817, May 2018.

[60] Federico De Luca and Cristian Cirací. Difference-frequency generation in plasmonic nanostructures: a parameter-free hydrodynamic description. *J. Opt. Soc. Am. B*, 36(8):1979–1986, Aug 2019.

[61] Sofia Evangelou. Nonlinear optical rectification of a coupled semiconductor quantum dot – metallic nanosphere system under a strong electromagnetic field. *Physica B: Condensed Matter*, 556:170 – 174, 2019.

[62] Alex G. F. de Beer, Sylvie Roke, and Jerry I. Dadap. Theory of optical second-harmonic and sum-frequency scattering from arbitrarily shaped particles. *J. Opt. Soc. Am. B*, 28(6):1374–1384, Jun 2011.

[63] Kristina Frizyuk. Second-harmonic generation in dielectric nanoparticles with different symmetries. *J. Opt. Soc. Am. B*, 36(8):F32–F37, Aug 2019.

[64] W. Luis Mochán, Guillermo Ortiz, Bernardo S. Mendoza, and José Samuel Pérez-Huerta. Photonic. Comprehensive Perl Archive Network (CPAN), 2016. Perl package for calculations on metamaterials and photonic structures.

[65] Guillermo P. Ortiz, Brenda E. Martínez-Zérega, Bernardo S. Mendoza, and W. Luis Mochán. Effective optical response of metamaterials. *Phys. Rev. B*, 79:245132, Jun 2009.

[66] W. Luis Mochán, Guillermo P. Ortiz, and Bernardo S. Mendoza. Efficient homogenization procedure for the calculation of optical properties of 3d nanostructured composites. *Opt. Express*, 18(21):22119–22127, Oct 2010.

[67] J S Pérez-Huerta, Guillermo P Ortiz, Bernardo S Mendoza, and W Luis Mochán. Macroscopic optical response and photonic bands. *New Journal of Physics*, 15(4):043037, apr 2013.

[68] Lucila Juárez-Reyes and W. Luis Mochán. Magnetic response of metamaterials. *physica status solidi (b)*, 255(4):1700495, 2018.

[69] Bernardo S. Mendoza and W. Luis Mochán. Tailored optical polarization in nanostructured metamaterials. *Phys. Rev. B*, 94:195137, Nov 2016.

[70] W. Luis Mochán, Raksha Singla, Lucila Juárez, and Guillermo P. Ortiz. Recursive calculation of the optical response of multicomponent metamaterials. *physica status solidi (b)*, 257(5):1900560, 2020.

[71] Ulises R. Meza, Bernardo S. Mendoza, and W. Luis Mochán. Second-harmonic generation in nanostructured metamaterials. *Phys. Rev. B*, 99:125408, Mar 2019.

[72] Robert Boyd. *Nonlinear Optics, Third Edition*. Academic Press, Inc., USA, 3rd edition, 2008.

[73] T.H. Maiman. Stimulated optical radiation in ruby. *Nature*, 187:493–494, 1960.

[74] P. A. Franken, A. E. Hill, C. W. Peters, and G. Weinreich. Generation of optical harmonics. *Phys. Rev. Lett.*, 7:118–119, Aug 1961.

[75] Norman M. Kroll. Parametric amplification in spatially extended media and application to the design of tuneable oscillators at optical frequencies. *Phys. Rev.*, 127:1207–1211, Aug 1962.

[76] R. Baumgartner and R. Byer. Optical parametric amplification. *IEEE Journal of Quantum Electronics*, 15(6):432–444, June 1979.

[77] A. Dubietis, R. Butkus, and A. P. Piskarskas. Trends in chirped pulse optical parametric amplification. *IEEE Journal of Selected Topics in Quantum Electronics*, 12(2):163–172, March 2006.

[78] Bruno E. Schmidt, Nicolas Thiré, Maxime Boivin, Antoine Laramée, François Poitras, Guy Lebrun, Tsuneyuki Ozaki, Heide Ibrahim, and François Légaré. Frequency domain optical parametric amplification. *Nature Communications*, 5(1):3643, 2014.

[79] A. K. Popov and V. M. Shalaev. Negative-index metamaterials: second-harmonic generation, manley-rowe relations and parametric amplification. *Applied Physics B*, 84(1):131–137, 2006.

[80] R. H. Stolen and Chinlon Lin. Self-phase-modulation in silica optical fibers. *Phys. Rev. A*, 17:1448–1453, Apr 1978.

[81] M. Hofer, M. E. Fermann, F. Haberl, M. H. Ober, and A. J. Schmidt. Mode locking with cross-phase and self-phase modulation. *Opt. Lett.*, 16(7):502–504, Apr 1991.

[82] M. D. Perry, T. Ditmire, and B. C. Stuart. Self-phase modulation in chirped-pulse amplification. *Opt. Lett.*, 19(24):2149–2151, Dec 1994.

[83] N. Zhavoronkov and G. Korn. Generation of single intense short optical pulses by ultrafast molecular phase modulation. *Phys. Rev. Lett.*, 88:203901, May 2002.

[84] Jeffrey H Shapiro and Mohsen Razavi. Continuous-time cross-phase modulation and quantum computation. *New Journal of Physics*, 9(1):16–16, jan 2007.

[85] J. E. Sipe, D. J. Moss, and H. M. van Driel. Phenomenological theory of optical second- and third-harmonic generation from cubic centrosymmetric crystals. *Phys. Rev. B*, 35:1129–1141, Jan 1987.

[86] M. Lewenstein, Ph. Balcou, M. Yu. Ivanov, Anne L'Huillier, and P. B. Corkum. Theory of high-harmonic generation by low-frequency laser fields. *Phys. Rev. A*, 49:2117–2132, Mar 1994.

[87] Amnon Yariv and David M. Pepper. Amplified reflection, phase conjugation, and oscillation in degenerate four-wave mixing. *Opt. Lett.*, 1(1):16–18, Jul 1977.

[88] Vincent Boyer, Alberto M. Marino, Raphael C. Pooser, and Paul D. Lett. Entangled images from four-wave mixing. *Science*, 321(5888):544–547, 2008.

[89] Stefano Palomba, Shuang Zhang, Yongshik Park, Guy Bartal, Xiaobo Yin, and Xiang Zhang. Optical negative refraction by four-wave mixing in thin metallic nanostructures. *Nature Materials*, 11:34–38, 2012.

[90] Yong Wang, Chia-Yu Lin, Alexei Nikolaenko, Varun Raghunathan, and Eric O. Potma. Four-wave mixing microscopy of nanostructures. *Adv. Opt. Photon.*, 3(1):1–52, Mar 2011.

[91] D. Yelin, D. Meshulach, and Y. Silberberg. Adaptive femtosecond pulse compression. *Opt. Lett.*, 22(23):1793–1795, Dec 1997.

[92] E. Treacy. Optical pulse compression with diffraction gratings. *IEEE Journal of Quantum Electronics*, 5(9):454–458, Sep. 1969.

[93] P. Colman, C. Husko, S. Combrié, I. Sagnes, C. W. Wong, and A. De Rossi. Temporal solitons and pulse compression in photonic crystal waveguides. *Nature Photonics*, 4(12):862–868, 2010.

[94] P. B. Corkum, Claude Rolland, and T. Srinivasan-Rao. Supercontinuum generation in gases. *Phys. Rev. Lett.*, 57:2268–2271, Nov 1986.

[95] T. A. Birks, W. J. Wadsworth, and P. St. J. Russell. Supercontinuum generation in tapered fibers. *Opt. Lett.*, 25(19):1415–1417, Oct 2000.

[96] John M. Dudley, Goëry Genty, and Stéphane Coen. Supercontinuum generation in photonic crystal fiber. *Rev. Mod. Phys.*, 78:1135–1184, Oct 2006.

[97] Francesco Monticone and Andrea Alù. Metamaterial, plasmonic and nanophotonic devices. *Reports on Progress in Physics*, 80(3):036401, feb 2017.

[98] Pieter Dumon, Gino Priem, Luis Romeu Nunes, Wim Bogaerts, Dries Van Thourhout, Peter Bienstman, Tak Keung Liang, Masahiro Tsuchiya, Patrick Jaenen, Stephan Beckx, Johan Wouters, and Roel Baets. Linear and nonlinear nanophotonic devices based on silicon-on-insulator wire waveguides. *Japanese Journal of Applied Physics*, 45(8B):6589–6602, aug 2006.

[99] Tyler W. Hughes, Momchil Minkov, Ian A. D. Williamson, and Shanhui Fan. Adjoint method and inverse design for nonlinear nanophotonic devices. *ACS Photonics*, 5(12):4781–4787, Dec 2018.

[100] Aleksandr A. Pikalov, Dien Ngo, Han Ju Lee, T. Randall Lee, and Steven Baldelli. Sum frequency generation imaging microscopy of self-assembled monolayers on metal surfaces: Factor analysis of mixed monolayers. *Analytical Chemistry*, 91(2):1269–1276, 2019.

[101] L. Moreaux, O. Sandre, and J. Mertz. Membrane imaging by second-harmonic generation microscopy. *J. Opt. Soc. Am. B*, 17(10):1685–1694, Oct 2000.

[102] Y. R. Shen. Nonlinear optical studies of surfaces. *Applied Physics A Solids and Surfaces*, 59(5):541–543, 1994.

[103] W. J. Kozlovsky, C. D. Nabors, and R. L. Byer. Efficient second harmonic generation of a diode-laser-pumped cw nd:yag laser using monolithic mgo:linbo/sub 3/ external resonant cavities. *IEEE Journal of Quantum Electronics*, 24(6):913–919, June 1988.

[104] Na Ji, Kai Zhang, Haw Yang, and Yuen-Ron Shen. Three-dimensional chiral imaging by sum-frequency generation. *Journal of the American Chemical Society*, 128(11):3482–3483, 2006. PMID: 16536497.

[105] R. Scheps and J. F. Myers. Dual-wavelength coupled-cavity ti:sapphire laser with active mirror for enhanced red operation and efficient intracavity sum frequency generation at 459 nm. *IEEE Journal of Quantum Electronics*, 30(4):1050–1057, April 1994.

[106] S. Blit, E. G. Weaver, T. A. Rabson, and F. K. Tittel. Continuous wave uv radiation tunable from 285 nm to 400 nm by harmonic and sum frequency generation. *Appl. Opt.*, 17(5):721–723, Mar 1978.

[107] Y.F. Lü, X.H. Zhang, X.H. Fu, J. Xia, T.J. Zheng, and J.F. Chen. Diode-pumped nd:LuVO4 and nd:YAG crystals yellow laser at 594 nm based on intracavity sum-frequency generation. *Laser Physics Letters*, 7(9):634–636, jun 2010.

[108] K. Fradkin, A. Arie, A. Skliar, and G. Rosenman. Tunable midinfrared source by difference frequency generation in bulk periodically poled ktiopo4. *Applied Physics Letters*, 74(7):914–916, 1999.

[109] Yuki Yamaguchi, Ryohei Hida, Takakazu Suzuki, Fumihiro Isa, Kenta Yoshikiyo, Leo Fujii, Hirofumi Nemoto, and Fumihiko Kannari. Shaping and amplification of wavelength-tunable mid-infrared femtosecond pulses generated by intra-pulse difference-frequency mixing with spectral focusing. *J. Opt. Soc. Am. B*, 35(12):C1–C7, Dec 2018.

[110] P. Canarelli, Z. Benko, R. Curl, and F. K. Tittel. Continuous-wave infrared laser spectrometer based on difference frequency generation in aggas2 for high-resolution spectroscopy. *J. Opt. Soc. Am. B*, 9(2):197–202, Feb 1992.

[111] Mikhail A. Belkin, Federico Capasso, Feng Xie, Alexey Belyanin, Milan Fischer, Andreas Wittmann, and Jérôme Faist. Room temperature terahertz quantum cascade laser source based on intracavity difference-frequency generation. *Applied Physics Letters*, 92(20):201101, 2008.

[112] Karun Vijayraghavan, Robert W. Adams, Augustinas Vizbaras, Min Jang, Christian Grasse, Gerhard Boehm, Markus C. Amann, and Mikhail A. Belkin. Terahertz sources based on Čerenkov difference-frequency generation in quantum cascade lasers. *Applied Physics Letters*, 100(25):251104, 2012.

[113] M.B. Raschke, M. Hayashi, S.H. Lin, and Y.R. Shen. Doubly-resonant sum-frequency generation spectroscopy for surface studies. *Chemical Physics Letters*, 359(5):367 – 372, 2002.

[114] Yujin Tong, Yanbao Zhao, Na Li, Yunsheng Ma, Masatoshi Osawa, Paul B. Davies, and Shen Ye. Interference effects in the sum frequency generation spectra of thin organic films. ii: Applications to different thin-film systems. *The Journal of Chemical Physics*, 133(3):034705, 2010.

[115] A. Tadjeddine, A. Le Rille, O. Pluchery, F. Vidal, W. Q. Zheng, and A. Peremans. Sum and difference frequency generation at the electrochemical interface. *physica status solidi (a)*, 175(1):89–107, 1999.

[116] J F McGilp. A review of optical second-harmonic and sum-frequency generation at surfaces and interfaces. *Journal of Physics D: Applied Physics*, 29(7):1812–1821, jul 1996.

[117] Y. R. Shen. Surface properties probed by second-harmonic and sum-frequency generation. *Nature*, 337(6207):519–525, 1989.

[118] Marcus Zimmermann, Christoph Gohle, Ronald Holzwarth, Thomas Udem, and Theodor W. Hänsch. Optical clockwork with an offset-free difference frequency comb: accuracy of sum- and difference-frequency generation. *Opt. Lett.*, 29(3):310–312, Feb 2004.

[119] William P. Dempsey, Scott E. Fraser, and Periklis Pantazis. Shg nanoprobes: Advancing harmonic imaging in biology. *BioEssays*, 34(5):351–360, 2012.

[120] József András Fülöp, László Pálfalvi, Matthias C. Hoffmann, and János Hebling. Towards generation of mj-level ultrashort thz pulses by optical rectification. *Opt. Express*, 19(16):15090–15097, Aug 2011.

[121] J. A. Fülöp, L. Pálfalvi, S. Klingebiel, G. Almási, F. Krausz, S. Karsch, and J. Hebling. Generation of sub-mj terahertz pulses by optical rectification. *Opt. Lett.*, 37(4):557–559, Feb 2012.

[122] K.-L. Yeh, M. C. Hoffmann, J. Hebling, and Keith A. Nelson. Generation of 10μj ultrashort terahertz pulses by optical rectification. *Applied Physics Letters*, 90(17):171121, 2007.

[123] R. W. Terhune, P. D. Maker, and C. M. Savage. Optical harmonic generation in calcite. *Phys. Rev. Lett.*, 8:404–406, May 1962.

[124] Bernardo S. Mendoza and W. Luis Mochán. Exactly solvable model of surface second-harmonic generation. *Phys. Rev. B*, 53:4999–5006, Feb 1996.

[125] Jesús A. Maytorena, Bernardo S. Mendoza, and W. Luis Mochán. Theory of surface sum frequency generation spectroscopy. *Phys. Rev. B*, 57:2569–2579, Jan 1998.

[126] P. S. Pershan. Nonlinear optical properties of solids: Energy considerations. *Phys. Rev.*, 130:919–929, May 1963.

[127] N. Bloembergen, R. K. Chang, S. S. Jha, and C. H. Lee. Optical second-harmonic generation in reflection from media with inversion symmetry. *Phys. Rev.*, 174:813–822, Oct 1968.

[128] Joseph Rudnick and E. A. Stern. Second-harmonic radiation from metal surfaces. *Phys. Rev. B*, 4:4274–4290, Dec 1971.

[129] J. E. Sipe, V. C. Y. So, M. Fukui, and G. I. Stegeman. Analysis of second-harmonic generation at metal surfaces. *Phys. Rev. B*, 21:4389–4402, May 1980.

[130] M. Corvi and W. L. Schaich. Hydrodynamic-model calculation of second-harmonic generation at a metal surface. *Phys. Rev. B*, 33:3688–3695, Mar 1986.

[131] Victor Mizrahi and J. E. Sipe. Phenomenological treatment of surface second-harmonic generation. *J. Opt. Soc. Am. B*, 5(3):660–667, Mar 1988.

[132] W. L. Schaich and Bernardo S. Mendoza. Simple model of second-harmonic generation. *Phys. Rev. B*, 45:14279–14292, Jun 1992.

[133] X. D. Zhu, Hajo Suhr, and Y. R. Shen. Surface vibrational spectroscopy by infrared-visible sum frequency generation. *Phys. Rev. B*, 35:3047–3050, Feb 1987.

[134] B. Dick, A. Gierulski, G. Marowsky, and G. A. Reider. Determination of the nonlinear optical susceptibility $\chi(2)$ of surface layers by sum and difference frequency generation in reflection and transmission. *Applied Physics B*, 38(2):107–116, Oct 1985.

[135] A. V. Petukhov. Sum-frequency generation on isotropic surfaces: General phenomenology and microscopic theory for jellium surfaces. *Phys. Rev. B*, 52:16901–16911, Dec 1995.

[136] A.V. Petukhov and Th. Rasing. Crystallinity effect on the infrared-visible sum frequency generation in noble metals. *Surface Science*, 377-379:414 – 417, 1997. European Conference on Surface Science.

[137] A.V. Petukhov, B.S. Mendoza, V.L. Brudny, W.L. Mochán, J.A. Maytorena, and Th. Rasing. Energy exchange in second-order nonlinear optics in centrosymmetric media. *physica status solidi (a)*, 170(2):417–422, 1998.

[138] Jesús A. Maytorena, W. Luis Mochán, and Bernardo S. Mendoza. Hydrodynamic model for sum and difference frequency generation at metal surfaces. *Phys. Rev. B*, 57:2580–2585, Jan 1998.

[139] Y. R. Shen. Basic theory of surface sum-frequency generation. *The Journal of Physical Chemistry C*, 116(29):15505–15509, Jul 2012.

[140] Luyu Wang, Franklin Che, Sergey A. Ponomarenko, and Zhizhang (David) Chen. Plasmon-enhanced spectral changes in surface sum-frequency generation with polychromatic light. *Opt. Express*, 21(12):14159–14168, Jun 2013.

[141] N.W. Ashcroft and N.D. Mermin. *Solid State Physics*. Saunders College, Philadelphia, 1976.

[142] J.E. Sipe and G.I. Stegeman. Chapter 15 - nonlinear optical response of metal surfaces. In V.M. Agranovich and D.L. Mills, editors, *Surface Polaritons*, volume 1 of *Modern Problems in Condensed Matter Sciences*, pages 661 – 701. Elsevier, 1982.

[143] Toshiki Yamada, Hajime Hoshi, Takaaki Manaka, Ken Ishikawa, Hideo Takezoe, and Atsuo Fukuda. Resonant enhancement of second-harmonic generation of electric quadrupole origin in phthalocyanine films. *Phys. Rev. B*, 53:R13314–R13317, May 1996.

[144] Yu Zhang, Di Huang, Yuwei Shan, Tao Jiang, Zhihong Zhang, Kaihui Liu, Lei Shi, Jinluo Cheng, John E. Sipe, Wei-Tao Liu, and Shiwei Wu. Doping-induced second-harmonic generation in centrosymmetric graphene from quadrupole response. *Phys. Rev. Lett.*, 122:047401, Jan 2019.

[145] Antonio Capretti, Carlo Forestiere, Luca Dal Negro, and Giovanni Miano. Full-wave analytical solution of second-harmonic generation in metal nanospheres. *Plasmonics*, 9(1):151–166, Feb 2014.

[146] Jing-Wei Sun, Xiang-Hui Wang, Sheng-Jiang Chang, Ming Zeng, and Na Zhang. Second harmonic generation of metal nanoparticles under tightly focused illumination. *Chinese Physics B*, 25(3):37803, 2016.

[147] Bingzhong Huo, Xianghui Wang, Shengjiang Chang, and Ming Zeng. Second harmonic generation of a single centrosymmetric nanosphere illuminated by tightly focused cylindrical vector beams. *J. Opt. Soc. Am. B*, 29(7):1631–1640, Jul 2012.

[148] Radoslaw Kolkowski, Justyna Szeszko, Benjamin Dwir, Eli Kapon, and Joseph Zyss. Effects of surface plasmon polariton-mediated interactions on second harmonic generation from assemblies of pyramidal metallic nano-cavities. *Opt. Express*, 22(25):30592–30606, Dec 2014.

[149] Claudio I. Valencia, Eugenio R. Méndez, and Bernardo S. Mendoza. Second-harmonic generation in the scattering of light by two-dimensional particles. *J. Opt. Soc. Am. B*, 20(10):2150–2161, Oct 2003.

[150] John David Jackson. *Classical electrodynamics; 2nd ed.* Wiley, New York, NY, 1975.

[151] Cristian Ciracì, Ekaterina Poutrina, Michael Scalora, and David R. Smith. Origin of second-harmonic generation enhancement in optical split-ring resonators. *Phys. Rev. B*, 85:201403, May 2012.

[152] J. A. Maytorena, W. Luis Mochán, and Bernardo S. Mendoza. Hydrodynamic model for SHG at conductor surfaces with continuous profiles. *prb*, 51:2556, 1995.

[153] Yadong Wang, Masood Ghotbi, Susobhan Das, Yunyun Dai, Shisheng Li, Xuerong Hu, Xuetao Gan, Jianlin Zhao, and Zhipei Sun. Difference frequency generation in monolayer mos2. *Nanoscale*, pages –, 2020.

[154] Qingchen Yuan, Liang Fang, Hanlin Fang, Juntao Li, Tao Wang, Wanqi Jie, Jianlin Zhao, and Xuetao Gan. Second harmonic and sum-frequency generations from a silicon metasurface integrated with a two-dimensional material. *ACS Photonics*, 6(9):2252–2259, Sep 2019.

[155] M. Fang, Z. Huang, W. E. I. Sha, and X. Wu. Maxwell–hydrodynamic model for simulating nonlinear terahertz generation from plasmonic metasurfaces. *IEEE Journal on Multiscale and Multiphysics Computational Techniques*, 2:194–201, 2017.

[156] Ming Fang, Kaikun Niu, Zhiaxiang Huang, Wei E. I. Sha, Xianliang Wu, Thomas Koschny, and Costas M. Soukoulis. Investigation of broadband terahertz generation from metasurface. *Opt. Express*, 26(11):14241–14250, May 2018.

[157] L. Sun, P. Figliozzi, Y. Q. An, M. C. Downer, W. L. Mochán, and B. S. Mendoza. Nonresonant quadrupolar second-harmonic generation in isotropic solids by use of two orthogonally polarized laser beams. *Opt. Lett.*, 30(17):2287–2289, Sep 2005.

[158] Robert Czaplicki, Mariusz Zdanowicz, Kalle Koskinen, Janne Laukkanen, Markku Kuittinen, and Martti Kauranen. Dipole limit in second-harmonic generation from arrays of gold nanoparticles. *Opt. Express*, 19(27):26866–26871, Dec 2011.

[159] Hua Lu, Xueming Liu, Renlong Zhou, Yongkang Gong, and Dong Mao. Second-harmonic generation from metal-film nanohole arrays. *Appl. Opt.*, 49(12):2347–2351, Apr 2010.

[160] Racheli Ron, Omer Shavit, Hannah Aharon, Marcin Zielinski, Matan Galanty, and Adi Salomon. Nanoporous metallic network as a large-scale 3d source of second harmonic light. *The Journal of Physical Chemistry C*, 123(41):25331–25340, Oct 2019.

[161] Sheng Liu, Michael B. Sinclair, Sina Saravi, Gordon A. Keeler, Yuanmu Yang, John Reno, Gregory M. Peake, Frank Setzpfandt, Isabelle Staude, Thomas Pertsch, and Igal Brener. Resonantly enhanced second-harmonic generation using iii–v semiconductor all-dielectric metasurfaces. *Nano Letters*, 16(9):5426–5432, 2016. PMID: 27501472.

[162] David R. Smith and John B. Pendry. Homogenization of metamaterials by field averaging (invited paper). *J. Opt. Soc. Am. B*, 23(3):391–403, Mar 2006.

[163] A. I. Căbuz, A. Nicolet, F. Zolla, D. Felbacq, and G. Bouchitté. Homogenization of nonlocal wire metamaterial via a renormalization approach. *J. Opt. Soc. Am. B*, 28(5):1275–1282, May 2011.

[164] Andrea Alù. First-principles homogenization theory for periodic metamaterials. *Phys. Rev. B*, 84:075153, Aug 2011.

[165] Roger Haydock. The recursive solution of the schrodinger equation. volume 35 of *Solid State Physics*, pages 215 – 294. Academic Press, 1980.

[166] Bernardo S. Mendoza and W. Luis Mochán. Birefringent nanostructured composite materials. *Phys. Rev. B*, 85:125418, Mar 2012.

[167] J S Pérez-Huerta, Guillermo P Ortiz, Bernardo S Mendoza, and W Luis Mochán. Macroscopic optical response and photonic bands. *New Journal of Physics*, 15(4):043037, apr 2013.

[168] José Samuel Pérez Huerta. *La función dieléctrica macroscópica de sistemas estructurados.* PhD thesis, Universidad Nacional Autónoma de México, 2014.

[169] W. Luis Mochán and Rubén G. Barrera. Electromagnetic response of systems with spatial fluctuations. i. general formalism. *Phys. Rev. B*, 32:4984–4988, Oct 1985.